University of Alberta

Diamond sources beneath the Hall Peninsula, Baffin Island, Nunavut: A preliminary assessment based on Chidliak diamonds

by

Katie Marie Alwyn Nichols

A thesis submitted to the Faculty of Graduate Studies and Research
in partial fulfillment of the requirements for the degree of

Master of Science

Earth and Atmospheric Sciences

©Katie Marie Alwyn Nichols
Spring 2014
Edmonton, Alberta

Dedication

This thesis is dedicated to my husband, my mum, and my brother; words cannot express how grateful I am for all of you.

Abstract

Diamonds from the Chidliak kimberlite field, located on the Hall
Peninsula of Baffin Island, are the focus of this study. Morphology, carbon and
nitrogen isotopic compositions, and nitrogen characteristics of Chidliak diamonds
are used to constrain diamond sources, and conditions of diamond formation and
preservation.

Strong variations in $\delta^{13}C$ and nitrogen content across growth layers
indicate that at least two diamond growth events occurred, interrupted by
resorption. Diamond mantle residence temperatures range from ~980 to 1350°C,
equivalent to a depth range of ~150-200 km.

Stable isotopic analyses indicate that diamond formation occurred
principally from fluids or melts with a dominant mantle signature (modes in $\delta^{13}C$
of -6‰ and $\delta^{15}N$ of -3‰), but contribution of a subducted crustal component is
also apparent (^{13}C depleted and ^{15}N enriched samples). Combined with
observations of overall high nitrogen contents (≤3830 atomic ppm), Chidliak
diamond characteristics suggest derivation (partially or completely) from eclogitic
mantle sources.

Acknowledgements

To my Supervisor, Thomas Stachel, thank you for teaching me about diamonds and the mantle, for your ongoing guidance, and the endless support you've given me throughout my Masters, no matter how busy you were. Most of all, thank you for introducing me to the world of mantle research, for that I will always be grateful.

This project was made possible by Peregrine Diamonds Ltd. by donating the diamonds used for this study, and by the Canada-Nunavut Geoscience office through provision of funding for this project. Funding through Thomas Stachel, provided by an NSERC Discovery Grant, is also gratefully acknowledged.

Jennifer Pell and David Mate are thanked for the support and valuable feedback they have provided throughout this project. A special thank you to Jeff Harris for teaching me the art of describing diamonds, explaining the internal growth structures of diamonds, and for the enlightening conversations and discussions. I would also like to thank Tom McCandless for teaching me about describing especially small diamonds. Thanks is also extended to Long Li for the enlightening discussions about nitrogen isotopes in the mantle.

Thank you everyone who helped me with analytical work, especially, Richard Stern, Aleisha Crowell and the staff at the Canadian Centre for Isotopic Microanalyses for teaching me how to do sample preparation, for assisting with cathodoluminescence imaging, the use of ion microprobe and for feedback. Thank you to the staff at the scanning electron microscope lab for assisting with sample preparation and SEM imaging.

Thank you to the friends I've met along the way, Brenna Fossum, Léanne Labossiere, David Dockman, and Laura Brin, who were always there for me when I needed them. Special thanks to Pedro Waterton, for being an excellent sounding board, and for your willingness to always discuss various aspects of the mantle with me.

Thank you to the past and present members of the DRG, especially Lucy Hunt, for your encouragement, advice, lab assistance and for the many discussions we have had; you have taught me so much through my time at the U

Table of Contents

List of Tables

List of Figures

List of Symbols and Abbreviations

Shape:

agg	Aggregate
c	Cuboid
c-agg	Cuboid aggregate
cf	Cuboid fragment
do	>50% octahedral, <50% dodecahedral
do-agg	>50% octahedral aggregate
dodec	Dodecahedra
dodec-frag	Dodecahedra fragment
dodec macle	Dodecahedral macle
f	Fragment
f-agg	Aggregate fragment
I	Irregular
m	Macle
o	Octahedron
o-agg	Octahedral aggregate
od	>50% dodecahedral, <50% octahedral
od-agg	>50% dodecahedral aggregate
of	Octahedral fragment
of-agg	Octahedral fragment aggregate
thh	Tetrahexahedroid

Color:

lbrown	Light brown
vl brown	Very light brown
lbrown/pink	Light brown/pink
lyellow	Light yellow
vl yellow	Very light yellow
dyellow	Dark yellow
lgreen-yellow	Light green yellow
lgreen-grey	Light green grey
dgrey	Dark grey

lgrey	Light grey

Other:

at. ppm	Atomic parts per million
CCIM	Canadian Centre for Isotopic Microanalyses
f_{O_2}	Oxygen fugacity
FTIR	Fourier transform infrared spectrometry
G9	Lherzolitic garnet
G10	Harzburgitic garnet
G3	Eclogitic garnet
G4	Pyroxenitic-eclogitic garnet
G?D	The "D" suffix indicates a strong association with diamond
Ga	Giga-annum; billions of years before present
Ha	Hectare
KIMs	Kimberlite indicator minerals
Km	Kilometer
K_N	Partition coefficient of nitrogen
kV	Kilovolts
Ma	Mega-annum; millions of years before present
m.y.	Millions of years
nA	Nanoamps
ng	Weight in nanograms
nm	Nanometers
NQ	Drill core with a diameter of 4.3 cm
NWT	Northwest Territories
ppm	Concentration expressed in parts per million
μm	Micrometer
SCLM	Subcontintental lithospheric mantle
SEM	Scanning electron microscope
SIMS	Secondary ion mass spectrometer
%B	The proportion of nitrogen in the B centre in diamond
°C	Degree Celcius
$\delta^{13}C$	Carbon isotope composition expressed relative to a known standard

$\delta^{15}N$	Nitrogen isotope composition expressed relative to a known standard
Δ_C	The per mil difference in carbon isotopic composition between two phases
Δ_N	The per mil difference in nitrogen isotopic composition between two phases
~	Approximately
‰	Parts per thousand/per mil
σ	Error expressed as 1 standard deviation from the mean
2σ	Error expressed as 2 standard deviations from the mean

Chapter 1: Introduction

1.0 Introduction:

Diamond is one of the most highly valued minerals in the world, with a range of appealing properties making it ideal for jewelry, industrial purposes and research. Gem diamonds are sought after for their beauty and durability, owing to the diamonds optical properties, and hardness. Gem diamonds are susceptible to break along cleavage planes if impacted; non-gem diamonds such as polycrystalline aggregates have a different texture lacking cleavage planes and are therefore much less likely to break, making these diamonds ideal for industrial purposes. In addition, industrial grade diamond is valued for its high thermal conductivity and heat capacity; it is used widely in polishing and cutting tools, diamond knives and embedded in drill bits. Modern high-tech applications include diamond electrodes that can be deployed as probes in extreme environments (e.g., high corrosiveness). From an academic view point, diamond is a highly interesting study object as it allows us to gain insights in the conditions of diamond formation in Earth's mantle; diamond is chemically inert and contains information about processes we cannot directly observe in nature, such as those occurring at great depths within Earth.

Diamond forms in four domains: there are lithospheric diamonds, sublithospheric diamonds, rare impactite and meteoritic diamonds, and ultra-high pressure diamonds. Lithospheric diamonds form in the subcontinental lithospheric mantle (SCLM) (e.g., Gurney, 2010); sublithospheric diamonds may be sourced from as deep as the 670 km discontinuity, where ferropericlase bearing

parageneses indicates sampling of the lower mantle (Stachel et al., 2005). Ultrahigh-pressure diamonds form in crustal rocks which were subducted along cratonic margins into the diamond stability field, and then were subsequently rapidly exhumed by tectonic forces back to the Earth's surface (Zhang et al., 1997). The focus of this study is on lithospheric diamonds from Chidliak, located on the Hall Peninsula, Southern Baffin Island, Nunavut, Canada.

Diamond is a trace mineral in kimberlite, ranging from zero (non-diamondiferous kimberlites) up to about 2 ppm (i.e. 10 carats/ton for the most diamondiferous kimberlite) (eg., Richardson et al, 1984; Haggerty, 1999). Diamond reaches the Earth's surface as xenocrysts in kimberlite or less commonly, lamproite magmas; kimberlites are ultrabasic and ultramafic rocks with varying percentages of alkalis and other incompatible constituents such as rare earth elements and large ion lithophile elements. They are rapidly ascending volatile rich magmas that may be sufficiently oxidizing to react with diamond surfaces. Diamondiferous kimberlites and lamproites are rare in comparison to non-diamondiferous kimberlites and lamproites.

Primary diamond deposits are restricted to cratons; rare exceptions are formed by diamond deposits found on mobile belts adjacent to cratons. However, the diamondiferous lithospheric mantle beneath such "off-craton" deposits has generally been shown to be Archean, i.e. the mobile belts have been thrusted onto subcratonic mantle (e.g., Luguet et al., 2009). This relationship between primary diamond deposits and stable continental shields is known as "Clifford's Rule" and guides diamond exploration (Clifford, 1966). Janse (1994) modified Clifford's

Rule, stating that diamondiferous kimberlites are found only on Archean cratons (Archons) which are older than 2.5 billion years. The Chidliak diamondiferous kimberlite field also follows this rule, being emplaced into 2.92-2.80 Ga basement orthogneisses (Pell et al., 2012).

Cratons are areas of ancient continental crust which have been stable for at least 2.5 billion years (even through periods of younger tectonism), and have lithospheric keels that extend deep into the mantle up to depths of 200 km (eg., Pearson et al., 2002; Stachel and Harris, 2009). Formation of the lithospheric mantle in the Archean was caused by extreme mantle melting and extraction of continental crust (Haggerty, 1999), thus creating a buoyant and rigid residue that is depleted in radiogenic heat producing elements, where the method of heat transfer is conductive rather than convective (as in the asthenosphere) (Stachel and Harris, 2009). The lithospheric keels have cooler temperatures in comparison to the surrounding asthenospheric mantle at equivalent depths and pressures, and have a lower f_{O_2} (eg., Pollack and Chapman, 1977; Foley, 2011). The graphite-diamond transition is raised to lower pressures in the lithospheric keels relative to the surrounding asthenosphere (Figure 1.1). Temperatures and pressures of formation for most diamonds are within the range of 900-1500°C and 50-60 kbar, respectively (Haggerty, 1986). Diamonds typically form along "cool" cratonic steady state geotherms; in general, the "cooler" the geotherm (i.e., the lower the heat flow) the larger the diamond window (defined as the depth range between the graphite-diamond transition and the base of the lithosphere). The steady state heat conduction model means that the surface heat flow is in equilibrium with the heat

flowing into the lithosphere plus the heat generated by radioactive decay of heat

producing elements within the lithosphere (Pollack and Chapman, 1977).
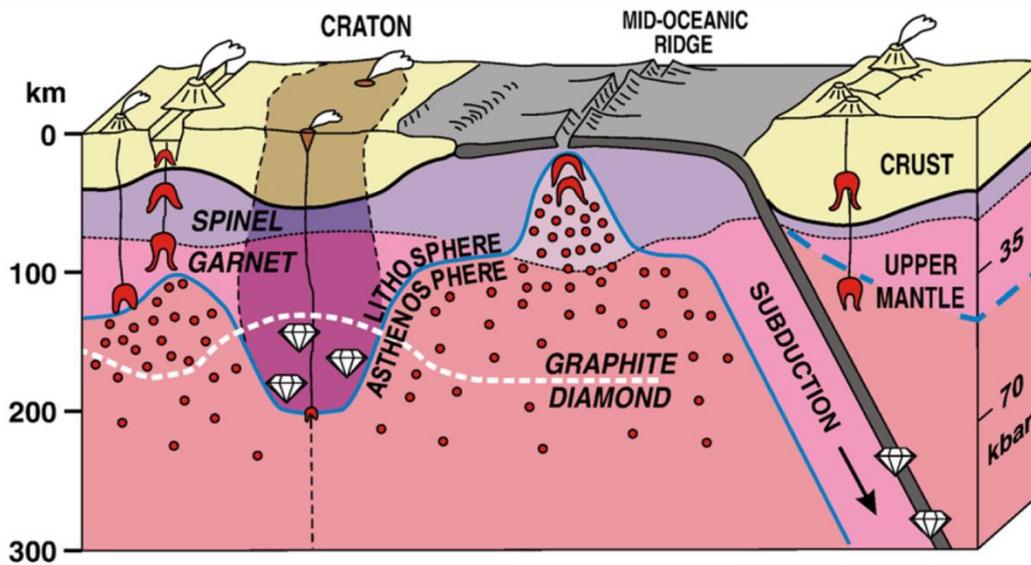
Figure 1.1. Cross sectional veiw through the Earth's crust and portion of the upper mantle (Fig 1. of Stachel and Harris, 2008), showing kimberlite emplacement on the craton, the graphite/diamond transition and related diamond stability field (below the white dashed line and the boundary between the lithosphere and asthenosphere) and the deep reaching lithospheric keels surrounded by asthenosphere.

1.1 Diamond Source Rocks:

Lithospheric diamonds are associated with mantle peridotites, eclogites,

and pyroxenites (Gurney et al., 2010). Peridotite is the primary rock in the upper

mantle and includes lherzolite, harzburgite and extremely depleted dunite;

Primitive mantle peridotite (lherzolite) is composed of olivine, orthopyroxene,

clinopyroxene, and either spinel (at pressures significantly below the graphite-

diamond transition) or garnet as the aluminum bearing phase. Harzburgite is

formed by intense melt extraction, causing clinopyroxene to disapear from the

assemblage. When >50% of melt is extracted from primitive mantle both

pyroxenes are removed from the residue and this rock type is a dunite, which is composed of >90% olivine.

Eclogite is the high pressure equivalent of oceanic basalt, and is composed of ≥90% omphacitic clinopyroxene and Cr-poor grossular garnet in roughly equal proportions; eclogite can contain minor phases such as sanidine, rutile, coesite kyanite and diamond.

Websterites are a class of pyroxenite composed of clinopyroxene, orthopyroxene, ± olivine and garnet. This rock type was first introduced by Gurney (1984) as the third principle diamond paragenesis and is chemically transitional between peridotite and eclogite. Prevalent models for the formation of websterites include: reactions between melts and fluids with mantle peridotite, crystal segregation of cumulates from magmas emplaced in the crust or upper mantle, or fragments from old subducted oceanic crust (eg., Litasov et al., 2000; Aulbach et al., 2002; Dantas et al., 2009).

Studies on silicate and oxide diamond inclusions show that peridotitic sources account for 65% of diamonds, eclogitic sources comprise 33% and websteritic sources are minor at 2% (Stachel and Harris, 2008).

1.2 Diamonds in Canada:

Diamond prospecting began in Canada in the 1960's, with the first major kimberlite discoveries in the 1980's, finally leading to the first diamond discovery in 1991 on the Slave Craton in the North West Territories (NWT). In 1998, Ekati (in the NWT) was the first diamond mine to go into production in Canada. The first diamond mine to open in Nunavut was Jericho, which remained open from

2006 to 2008. Canada is the third largest diamond producing country in the world; the top five diamond producing countries in 2009 (in order: Botswana, Russia, Canada, South Africa and Angola) account for 83% of worldwide diamond production by value (Read and Janse, 2009).

1.3 Thesis Intent:

The focus of this thesis is to provide the first direct constraints on the sources and mantle residence history for diamonds from a previously unstudied area of the world, the Chidliak project on the Hall Peninsula of Baffin Island. Diamond physical characterization (including diamond shape, color, and surface features), and internal growth structures imaged by cathodoluminescence are used to formulate a sequence of events from diamond genesis to kimberlite emplacement. Carbon and nitrogen isotopic compositions and nitrogen contents (measured via SIMS) are used to fingerprint the upper mantle source of Chidliak diamonds, placing them into a worldwide context. Nitrogen contents and aggregation states are measured using FTIR to constrain the diamond mantle residence and thermal history.

References:

Aulbach, S., Stachel, T., Viljoen, K.S., Brey, G.P. and Harris, J.W., 2002. Eclogitic and websteritic diamond sources beneath the Limpopo Belt - Is slab-melting the link? Contributions to Mineralogy and Petrology, 143(1): 56-70.

Clifford, T.N., 1966. Tectono-metallogenic units and metallogenic provinces of Africa. Earth and Planetary Science Letters, 1(6): 421-434.

Dantas, C., Grégoire, M., Koester, E., Conceição, R.V. and Rieck Jr, N., 2009. The lherzolite-websterite xenolith suite from Northern Patagonia (Argentina): Evidence of mantle-melt reaction processes. Lithos, 107(1-2): 107-120.

Foley, S.F., 2011. A Reappraisal of Redox Melting in the Earth's Mantle as a Function of Tectonic Setting and Time. Journal of Petrology, 52(7-8), 1363-1391.

Gurney, J.J., Harris, J.W. and Rickard, R.S., 1984. Silicate and oxide inclusions in diamonds from the Orapa mine, Botswana. In: J. Kornprobst (Editor), Kimberlites II: The Mantle and Crust-Mantle Relationships. Elsevier, Amsterdam, pp. 3-9.

Gurney, J.J., Helmstaedt, H.H., Richardson, S.H. and Shirey, S.B., 2010. Diamonds through time. Economic Geology, 105(3): 689-712.

Haggerty, S.E., 1986. Diamond genesis in a multiply-constrained model. Nature, 320(6057): 34-38.

Haggerty, S.E., 1999. A diamond trilogy: Superplumes, supercontinents, and supernovae. Science, 285(5429): 851-860.

Janse, A.J.A., 1994. Is Clifford's Rule still valid? Affirmative examples from around the World. Diamonds: Characterization, Genesis and Exploration, 2. CPRM, Araxa, Brazil, 215-235 pp.

Litasov, K.D., Foley, S.F. and Litasov, Y.D., 2000. Magmatic modification and metasomatism of the subcontinental mantle beneath the Vitim volcanic field (East Siberia): Evidence from trace element data on pyroxenite and peridotite xenoliths from Miocene picrobasalt. Lithos, 54(1-2): 83-114.

Luguet, A., Jaques, A.L., Pearson, D.G., Smith, C.B., Bulanova, G.P., Roffey, S.L., Rayner, M.J., Lorand, J.P., 2009. An integrated petrological, geochemical and Re-Os isotope study of peridotite xenoliths from the Argyle lamproite, Western Australia and implications for cratonic

diamond occurrences. Lithos, 112, 1096-1108.

Pearson, D.G., Irvine, G.J., Carlson, R.W., Kopylova, M.G. and Ionov, D.A., 2002. The development of lithospheric keels beneath the earliest continents; time constraints using PGE and Re-Os isotope systematics. Geological Society Special Publications, 199: 65-90.

Pell, J., Grütter, H., Dempsey, S. and Neilson, S., 2012. Exploration and discovery of the Chidliak kimberlite province, Baffin Island, Nunavut: Canada's newest diamond district. 10th International Kimberlite Conference, Bangalore, India. 2012, conference CD (abstract 40).

Pollack, H.N. and Chapman, D.S., 1977. On the regional variation of heat flow, geotherms, and lithospheric thickness. Tectonophysics, 38(3-4): 279-296.

Read, G.H. and Janse, A.J.A., 2009. Diamonds: Exploration, mines and marketing. Lithos, 112, Supplement 1(0): 1-9.

Richardson, S.H., Gurney, J.J., Erlank, A.J. and Harris, J.W., 1984. Origin of diamonds in old enriched mantle. Nature, 310(5974): 198-202.

Stachel, T., Brey, G.P. and Harris, J.W., 2005. Inclusions in sublithospheric diamonds: Glimpses of deep Earth. Elements, 1(2): 73-78.

Stachel, T. and Harris, J.W., 2008. The origin of cratonic diamonds - Constraints from mineral inclusions. Ore Geology Reviews, 34(1-2): 5-32.

Stachel, T. and Harris, J.W., 2009. Formation of diamond in the Earth's mantle. Journal of Physics Condensed Matter, 21(36).

Zhang, R.Y., Liou, J.G., Ernst, W.G., Coleman, R.G., Sobolev, N.V., Shatsky, V.S., 1997. Metamorphic evolution of diamond-bearing and associated rocks from the Kokchetav Massif, northern Kazakhstan. Journal of Metamorphic Geology, 15(4), 479-496.

Chapter 2: Geological Background

2.0 Introduction:

The diamonds used for this study come from kimberlites on the Chidliak
Project area, 120 km northeast of Iqaluit, located on the Hall Peninsula, southern
Baffin Island, Nunavut (Figure 2.1) (Pell, 2008; Pell and Farrow, 2012).
Specifically, this study will focus on diamonds from two kimberlites, CH-7
(kimberlite sample P5500) and CH-6 (kimberlite sample P6807). The Hall
Peninsula is separated into three domains (Scott, 1996), one of which is the Hall
Peninsula block (previously called the eastern plutonic domain) that hosts the
Chidliak kimberlites (Pell et al., 2013). The first kimberlite at Chidliak was
identified in 2008, with many kimberlite discoveries occurring since then. Pell et
al. (2013) studied the Chidliak kimberlites in detail, while kimberlite age dating
was completed by Heaman et al. (2012).

2.1 The Hall Peninsula:

The geology of the Hall Peninsula is poorly understood; reconnaissance
scale mapping was done in 1965, followed by a more detailed study along an
East-West transect by Scott (1996). Scott (1996) separated the Hall Peninsula into
three domains based on the reconnaissance mapping: (1) a western plutonic
domain (2) a central metasedimentary domain, and (3) an eastern plutonic
domain. The western plutonic domain contains the eastern edge of the 1.865-
1.845 Ga Cumberland Batholith (Whalen et al., 2010), which is in contact with
Paleoproterozoic supracrustal rocks to the East (St. Onge, 2001; Pell and Farrow,
2012), and consists mainly of monzogranites and granodiorite and is interpreted to

have intruded the central domain (Scott, 1996; Whalen et al., 2010). The central

metasedimentary domain is mainly comprised of rusty-weathered quartz-feldspar-

biotite psammite with lilac garnets; the eastern plutonic domain is dominated by

fine- to medium-grained tonalitic gneisses, but monzogranite and minor

metasedimentary rocks are also present (Scott, 1996). The eastern plutonic

domain is now called the Hall Peninsula Block (Whalen et al., 2010) which

includes the tonalitic gneissic rocks of ca. 2.92–2.80 Ga age and younger clastic

units (Scott, 1999). The Hall Peninsula block is separated from northern Baffin

Island by the 1.88-1.865 Ga Baffin Suture (Snyder, 2010).

2.1.1 The Hall Peninsula Block:

The Chidliak kimberlites are hosted solely within the Hall Peninsula block

basement made up of ortho- and para-gneisses (Pell et al., 2013). The origin of the

Hall Peninsula block is unresolved, but to date there are three theories outlined in

Pell et al. (2013): (1.) that it may be a microcontinent that was accreted during a

two-phase, three-way collision between the Superior, Rae and North Atlantic

cratons at about 1.865-1.850 Ga and 1.82-1.79 Ga (Snyder, 2010; Whalen et al.,

2010). The initial collision pre-dates the emplacement of the Cumberland

Batholith which connects the Rae craton, North Atlantic craton and the Hall

Peninsula block (Whalen et al., 2010). (2.) That it is part of the Nain/North

Atlantic craton (Scott, 1996; Scott, 1999, Theriault et al., 2001). Or (3.) that it is a

reworked fragment of Archean gneisses correlative with those of the Trans

Hudson Orogen in Canada and the Nagssugtoqidian Orogen of west Greenland

(St. Onge et al. 2007, Pell et al., 2013).

A teleseismic study done at the seismological observatory station FRB

(near the Iqaluit airport) identified northeastward-dipping layers (at 15°) within

the upper mantle, 50-150 km below the FRB station (Snyder, 2010). Snyder

(2010), interpreted these layers as underthrust parts of the Sugluk Block, the

Narsajuag Arc and Cape Smith Fold belt, and at greater depths, the Superior

craton; if the modeled 15° dip was constant between the FRB station and the Hall

Peninsula Block, these layers would project to depths of 100-160 km at Chidliak;

the underthrust oceanic and microcontinental layers may provide a suitable

protolith for kimberlite indicator minerals and diamond.
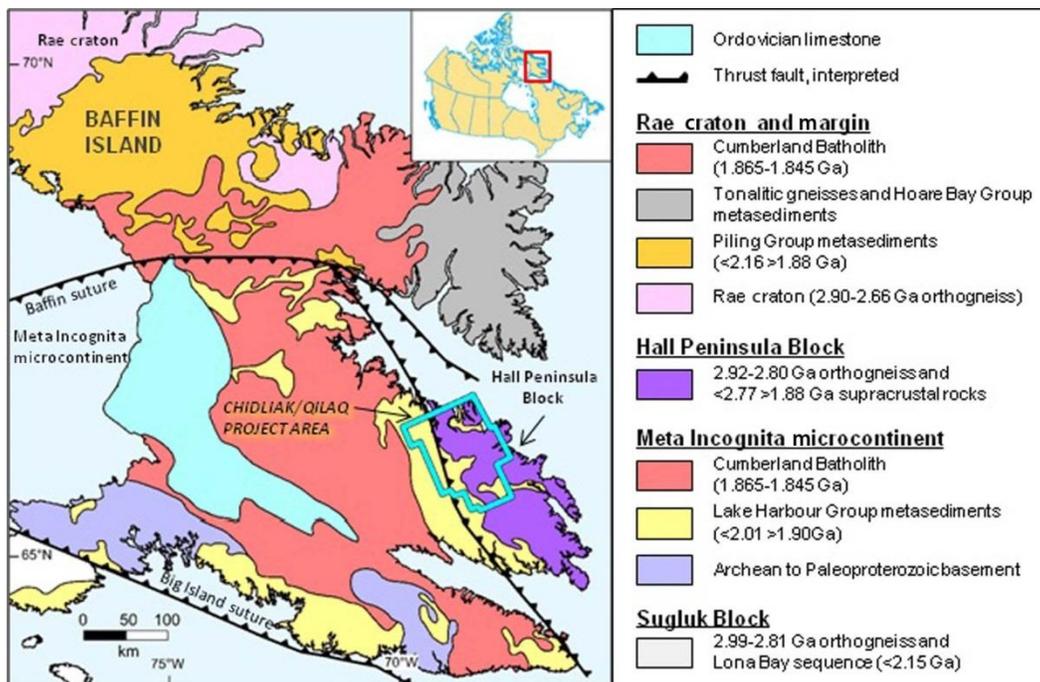
Figure 2.1. Simplified regional geological map of southern Baffin Island (after St-Onge et. al., 2006; Whalen et. al., 2010), showing the location of the Hall Peninsula Block (purple) and the Chidliak project area (light blue box) (Fig. 1, Pell et al., 2012).

2.2 Chidliak Kimberlites:

Kimberlites were identified after a suite of kimberlite indicator minerals (KIMs) were discovered during the 2005 field season. In 2005, diamond exploration employing traditional methods for a previously glaciated terrain was done by collecting glacial till sediments on a grid spacing of 15 km; this lead to the identification of KIMs – such as garnet and clinopyroxene – and kimberlite mineral trains. Since the initial sampling, more than 3000 glacial till samples have been collected using a smaller grid size of 500 to 2500 m (Pell et al., 2013; Neilson et al., 2012). Subsequently, in 2008, a helicopter-borne magnetic/electromagnetic survey was flown, totaling 11 700 line-kilometers (Pell, 2009). The first kimberlite (CH-1) was found in 2008 by ground prospecting in an area of high interest KIMs and an airborne geomagnetic anomaly (Pell et al., 2013). Further kimberlites were identified by core drilling, reverse circulation drilling or ground prospecting (Pell et al., 2013). During the 2013 field season, another 3 confirmed kimberlites have been identified, bringing the total count to 67 kimberlites, 64 at Chidliak, and 3 at the neighbouring Qilaq project (Peregrine Diamonds Ltd, 2013).

The Chidliak kimberlites have varying surface expressions such as a thin veneer of till or vegetation anomalies. Surface areas range from <1 ha to >5 ha, and seven kimberlites are located beneath lakes (Pell et al., 2013).

In addition to kimberlite pipes there are sheet like kimberlite bodies (dykes); the dykes have characteristics typical of hypabyssal kimberlites and may contain basement xenoliths (Pell et al., 2013). Kimberlite pipes also contain

sedimentary xenoliths in addition to basement xenoliths; combined, the crustal xenoliths found in the kimberlites typically account for less than 10 vol.% (Pell et al., 2013).

The pipe-like Chidliak kimberlite bodies can contain what has been interpreted to be melt-free and melt-bearing juvenile pyroclasts which formed during volcanic eruptions (magmaclasts), and are typically mixed with variably fragmented melt-free olivine crystals (Pell et al., 2013 and references therein). The kimberlites contain olivine phenocrysts and macrocrysts; some kimberlites contain mantle xenoliths including garnet lherzolite, garnet harzburgite, websterite and eclogite that can range up to 35 cm in size (Pell et al., 2013). Neilson et al. (2012) studied kimberlite indicator minerals at Chidliak and found that eclogitic (G3D) and eclogitic-websteritic (G4D) facies garnets are significant for the northern lobe of the CH-7 kimberlite (90.1% of garnets) and for the CH-6 kimberlite (71.6% of garnets).

2.2.1 Kimberlite CH-7:

An outcrop, ~65 m by 10 m in size, of kimberlite CH-7 was discovered through investigating a high magnetic geophysical anomaly (Pell, 2009). Pell et al. (2013) found that the CH-7 kimberlite is comprised of at least two elliptical shaped distinct lobes, with a surface area of 1 ha. The smaller northern lobe contains massive macrocrystic coherent (i.e. magmatic) kimberlite, with rare basement gneiss xenoliths, while supracrustal xenoliths are notably absent (Pell et al., 2013). The larger southern lobe is a steeply plunging asymmetrical pipe and contains four distinct units of kimberlite; three of the four units are pyroclastic

kimberlite and are characterized by internally variable olivine content, packing, grain size and xenolith distribution. None of the pyroclastic units shows distinct bedding but each contains a juvenile pyroclast population. The contacts between the units are sharp and steeply dipping (Pell et al., 2013). It appears that each of the three pyroclastic units were consolidated before any mixing between kimberlite types could occur (Pell et al., 2013). The fourth unit is a coherent kimberlite and has a carbonate rich crystalline groundmass and unique to this unit, some carbonate xenoliths have distinct zonal alteration and irregular boundaries with impinging olivine grains (a feature typically associated with high temperature deposition) (Pell et al., 2013).

All four units contain both carbonate and basement xenoliths (generally <20 cm) in varying amounts but rarely exceed 5% each, although large carbonate and basement xenolith rich blocks up to 1.5 and 4.9 m core length, respectively have also been identified (Pell et al., 2013). There are numerous broken olivine and garnet grains (Pell et al., 2013). The kimberlite sample P5500 from kimberlite CH-7 was collected from float and subcrop.

2.2.2 Kimberlite CH-6:

Kimberlite CH-6 was discovered by diamond drilling of a magnetic low geophysical anomaly (Pell, 2009). It was also described in Pell et al. (2013) with has a surface area of approximately 1 ha; it has steep sides, is kidney to elliptical shaped and is plunging slightly southwest. There are two main types of pipe infill textures, separated based on the presence or absence of carbonate xenoliths (Pell et al., 2013 and references therein). The main textural pipe infill is a carbonate

xenolith bearing kimberlite, which generally contains <5% carbonate xenoliths smaller than 15 cm, but rare xenolith rich zones up to 13 m have also been identified in drill core (Pell et al., 2013). The second and less abundant textural pipe infill is a carbonate xenolith poor, locally magmaclastic kimberlite which is typically found in layers (<15 m) intercalated with the main infill.

There are three main units in this kimberlite. The dominant unit in the upper part of the pipe is a pyroclastic kimberlite unit (carbonate xenolith-bearing kimberlite, with magmaclasts); below this is a kimberlite unit that is homogeneous and carbonate xenolith-free, with low amounts of basement xenoliths and minor magmaclasts. This unit resembles hypabyssal kimberlite in regard to distribution of olivine and the crystalline groundmass but likely is effusive ("kimberlite lava flows") in origin (Pell et al., 2013). It is intercalated with clastogenic apparently coherent kimberlite (Pell et al., 2013), (i.e. originally pyroclastic kimberlite). Underlying this hypabyssal-like kimberlite unit is a carbonate xenolith-bearing, apparently coherent kimberlite (Pell et al., 2013). The boundaries between textural varieties are complex, with sharp contacts between units lacking, and as such it is difficult to trace boundaries through the kimberlite body (Pell et al., 2013). The P6807 kimberlite sample from kimberlite CH-6 was collected from NQ core drilling.

2.3 Kimberlite Ages:

Thirty one kimberlites, twenty nine from Chidliak and two from the neighbouring Qilaq project, have been dated using the perovskite U-Pb ID-TIMS method to determine kimberlite ages and duration of emplacement (Figure 2.2;

Heaman et al., 2012). The duration of emplacement was approximately 18 m.y.,

from 156 to 138 Ma, although the majority of kimberlites (22/31) were emplaced

within a short time span of 7 m.y. from 150 to 143 Ma (Heaman et al., 2012). The

timing of Chidliak/Qilaq kimberlite emplacement establishes a relationship with

the Attawapiskat, Kirkland Lake, and Timiskaming kimberlite provinces in

Eastern Canada (Heaman et al., 2012), which have been previously linked to the

Great Meteor hot spot track (Heaman and Kjarsgaard, 2000). Kimberlites that

have been dated at Attawapiskat (180-156 Ma), Kirkland Lake (165-152 Ma),

Timiskaming (155-134 Ma), Victoria Island (286-256 Ma), Churchill (225-170

Ma), Jericho-Muskox (173 Ma), and Somerset Island (105-88 Ma) contain

sedimentary carbonate xenoliths that are stratigraphically equivalent to those

identified at Chidliak (Heaman et al., 2012).
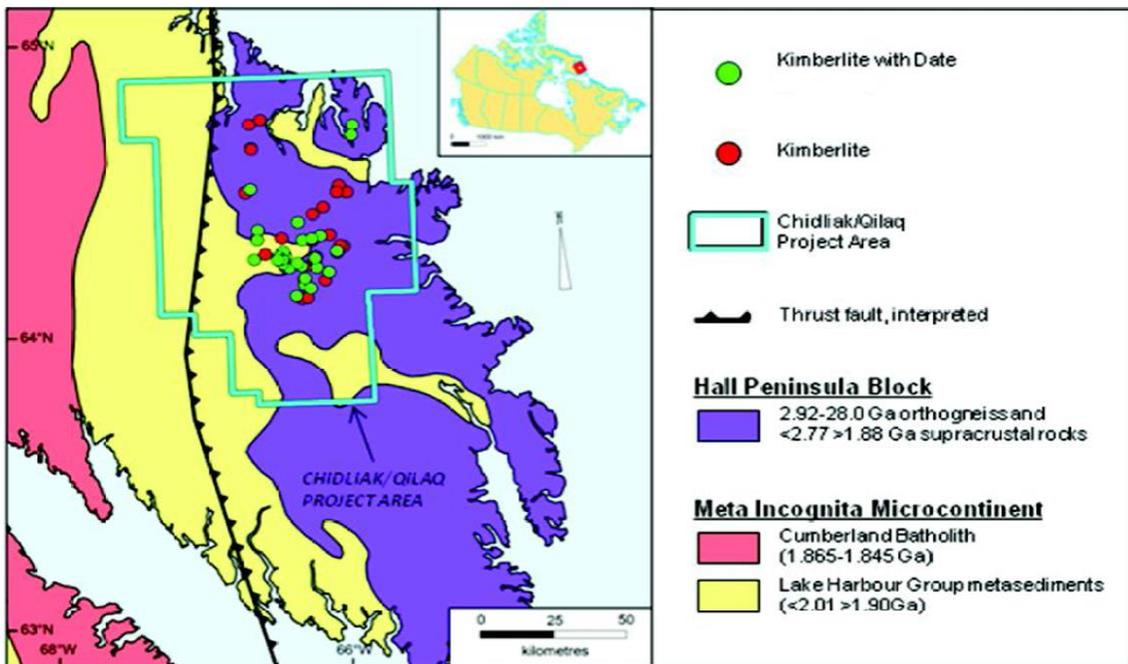
Figure 2.2. The spatial distribution of kimberlites from the Chidliak and neighbouring Qilaq project areas (outlined with the light blue box); kimberlites that have been dated are green, kimberlites without dates are red (Fig. 1, Heaman et al., 2012).

16

2.4 Further Exploration:

In 2013, a 508 tonne bulk sample from kimberlite CH-6 will be processed at Saskatchewan Research Council (SRC) and ultimately will result in a "preliminary revenue model and establish an initial resource for kimberlite CH-6" (Peregrine Diamonds Ltd, 2013). This work will serve as a foundation for future independent resource calculations and together with the mining study being completed by De Beers will enable the completion of a Preliminary Economic Assessment for CH-6 in the first half of 2014 (Peregrine Diamonds Ltd, 2013).

References:

Heaman, L.M., Grütter, H.S., Pell, J., Holmes, P. and Grenon, H., 2012. U-Pb geochronology, Sr- and Nd-isotope compositions of groundmass perovskite from the Chidliak and Qilaq kimberlites, Baffin Island, Nunavut. 10th International Kimberlite Conference, Bangalore, India. 2012, conference CD (abstract 193).

Heaman, L.M., Kjarsgaard, B.A. and Creaser, R.A., 2004. The temporal evolution of North American kimberlites. Lithos, 76(1-4 spec. iss.): 377-397.

Neilson. S, G.H., Pell. J, Grenon. H, 2012. The Evolution of Kimberlite Indicator Mineral Interpretation on the Chidliak Project, Baffin Island, Nunavut. 10th International Kimberlite Conference, Bangalore, India, 2012, conference CD (abstract 162).

Pell, J., 2008. Technical report on the Chidliak Property, Baffin Region, Nunavut; Peregrine Diamonds, pp. 73.

Pell, J., 2009. 2009 Technical report on the Chidliak Property, Baffin Region, Nunavut; Peregrine Diamonds, pp. 116.

Pell, J., Grütter, H., Dempsey, S. and Neilson, S., 2012. Exploration and discovery of the Chidliak kimberlite province, Baffin Island, Nunavut: Canada's newest diamond district. 10th International Kimberlite Conference, Bangalore, India. 2012, conference CD (abstract 40).

Pell, J., Farrow, D., 2012b. Updated 2011 Technical report on the Chidliak Property, Baffin Region, Nunavut; Peregrine Diamonds, pp. 148.

Pell, J., Grütter, H., Neilson, S., Lockhart, G., Dempsey, S. and Grenon, H., 2013. Exploration and Discovery of the Chidliak Kimberlite Province, Baffin Island, Nunavut: Canada's Newest Diamond District. In: D.G. Pearson, H.S. Grütter, J.W. Harris, B.A. Kjarsgaard, H. O'Brien, N.V.C. Rao and S. Sparks (Editors), Proceedings of 10th International Kimberlite Conference. Springer India, Bangalore, India. 209-227.

Peregrine Diamonds Ltd., Sept 9, 2013. Peregrine Provides Chidliak Update and Announces Discovery of Three New Kimberlites.

Scott, D.J., 1996. Geology of the Hall Peninsula east of Iqaluit, southern Baffin Island, Northwest Territories. Current Research 1996-C: 83-91.

Scott, D.J., 1999. U–Pb geochronology of the eastern Hall Peninsula, southern Baffin Island, Canada: a northern link between the Archean of West Greenland and the Paleoproterozoic Torngat Orogen of northern Labrador.

Precambrian Research, 93(1): 5-26.

Snyder, D.B., 2010. Mantle lithosphere structure beneath southeast Baffin Island, Nunavut from teleseismic studies. Geological Survey of Canada, Current Research 2010-8: 6.

St-Onge, M.R., Jackson, G.D. and Henderson, I., 2006. Geology, Baffin Island (south of 70ᵒN and east of 80ᵒW), Nunavut. Geological Survey of Canada, Open File 4931.

St-Onge, M.R., Scott, D.J. and Wodicka, N., 2001. Terrane boundaries within the Trans-Hudson Orogen (Quebec–Baffin segment), Canada: changing structural and metamorphic character from foreland to hinterland. Precambrian Research, 107(1-2): 75-91.

Thériault, R.J., St-Onge, M.R. and Scott, D.J., 2001. Nd isotopic and geochemical signature of the Paleoproterozoic Trans-Hudson Orogen, southern Baffin Island, Canada: implications for the evolution of eastern Laurentia. Precambrian Research, 108(1–2): 113-138.

Whalen, J.B., Wodicka, N., Taylor, B.E. and Jackson,G.D., 2010. Cumberland batholiths, Trans-Hudson Orogen, Canada: petrogenesis and implications for Paleoproterozoic crustal and orogenic processes. Lithos, 117: 99-118.

Chapter 3: Chidliak Diamond Physical Characteristics

3.0 Introduction:

Two hundred and ten diamonds were chosen from an original sample of ~740 diamonds on the basis of size; diamonds from the largest size class were chosen first, through each size class to progressively smaller sizes. All diamonds in the size range of 850 μm to 300 μm were sampled, and an approximately equal number of diamonds from the smallest sieve size (-300 μm +212 μm) were excluded from both kimberlite samples; the upper stone size is -850 μm +650 μm and the lower stone size is -300 μm +212 μm. One-hundred and five diamonds come from kimberlite sample P6807 (kimberlite pipe CH-6) and the other 105 are from kimberlite sample P5500 (kimberlite pipe CH-7). For the purpose of this study the description of surface features will be limited to features seen on octahedral, cuboid and dodecahedral diamonds with the aid of a binocular microscope.

A JEOL 6301F scanning electron microscope (SEM) was used to image a small subset of diamonds at high resolution to aid in identification of surface features. The characteristics identified using SEM confirmed those seen with the binocular microscope and revealed additional smaller scale features beyond the resolution of light microscopy. Internal growth structures can be studied by polishing diamond to reveal the inner portion and subsequent cathodoluminescence (CL) imaging. Besides surface features, the shape, size, color, and number of diamond crystals is described. Combined, these data provide

information about diamond formation and the sequence of events experienced from diamond genesis in the mantle throughout its ascent to the surface.

3.1 Physical Characteristics:

3.1.1 Diamond Shapes:

Diamond is an allotrope of carbon, in which the carbon atoms are bonded by strong covalent bonds in the crystal lattice. Because they have grown as a regular lattice of atoms, diamond crystals often have sharp edges and flat faces (Wilks, and Wilks, 1991). The final morphology of a crystal is determined by the growth plane which moves outward most slowly, as the quickest growing plane becomes increasingly smaller and eventually disappears completely (Sunagawa, 1981). Variations of the rates of growth of the different crystal faces may result in some of the faces becoming larger than others, while still maintaining the same crystal orientation (Robinson, 1979).

A diamond's shape depends on how it has grown; growth may occur by spreading of layers (Wilks and Wilks, 1991) with layer by layer growth proceeding through a spiral growth mechanism (Sunagawa, 2005). This growth can be complex, the layers may be stepped, and the edges may be kinked (Wilks and Wilks, 1991).

Diamond may crystallize in two primary forms: octahedra, including macles (flat triangular twins with two prominent parallel {111} faces), and cuboids, including re-entrant cubes (e.g., Robinson 1978; Welbourn et al., 1989). Diamond aggregates may also form and consist of two or more intergrown diamonds; when a distinct crystal shape is discernible it is classified as an

21

aggregate of that shape, (e.g., a cuboid aggregate). Secondary diamond shapes include dodecahedral and irregular. Intermediate stages of dodecahedral resorption are classified as do (octahedral faces dominant) and od (dodecahedral faces dominant but some octahedral faces still visible). Classification of irregular diamonds adheres to Harris et al. (1975): if ≥50% of the original morphology remains a diamond will be classified based on the observed shape, if <50% of the original morphology remains it will be classified as irregular. Diamonds are classified as fragments when only broken surfaces remain; if part of the original morphology remains this observation is added as a modifier (e.g., octahedral fragment). Breakage may occur either pre- or post- kimberlite ascent.

3.1.2 Diamond Color:

Diamonds may display a large range of colors, the most common of these being colorless, yellow and brown, and less commonly grey, black and pink. For small diamonds, perceived color is a function of thickness; for diamonds in the size range of 212-850 μm perceived color can, therefore, be misleading.

Diamonds with little to no nitrogen impurities (Type II) and diamonds with partially or fully aggregated nitrogen impurities (Type Ia) are both commonly colorless (Robinson, 1979). Brownish yellow coloration is attributed to single nitrogen centres (C centres) and paler yellow colors (Cape yellow) are caused by N2 centres invariably associated with nitrogen N3 centres (Wilks and Wilks, 1991). Brown coloration (sometime with a mauve tinge) results from a shearing stress causing plastic deformation of diamond (eg. Orlov, 1977; Robinson, 1979), creating clusters of vacancies responsible for the brown

22

coloration within the diamond lattice (Fisher et al., 2009). However, not all diamonds with plastic deformation lines on the diamond surfaces are brown. High temperature and high pressure conditions may anneal these vacancy clusters during mantle residence; therefore it is suggested that brown coloration occurs in diamonds that were plastically deformed during kimberlite emplacement whereas diamonds that were plastically deformed during mantle residence would lose the brown coloration to annealing (Fisher et al., 2009). Grey and black diamond coloration likely is due to submicroscopic inclusions creating a cloudy appearance, or caused by internal graphitization (Robinson, 1979).

3.1.3 Diamond Surface Features:

Octahedral diamonds may show both primary growth surface features and secondary surface features, cuboid diamonds and dodecahedral diamonds can show only secondary surface features. Some secondary surface features are not restricted to any particular diamond shape.

Primary surface features found on octahedral diamonds are triangular plates, known as stacked growth layers, which have sharp edges (Robinson, 1979). Secondary surface features on octahedral diamonds include shield shaped laminae, negative trigonal pits (trigons), positive trigons, and hexagonal pits (Robinson, 1979). These features are not seen on every octahedral diamond, nor are they always seen together. During resorption the sharp edges of stacked growth layers convert to rounded edges, producing a "shield like appearance" (Orlov, 1977). Trigons may be positive (same orientation as the crystal face) or negative (the opposite orientation of the crystal face), and may be either

pyramidal- or flat-bottomed; pyramidal trigons are formed at the earliest stages of resorption although flat bottomed trigons can also develop simultaneously with pyramidal trigons (Orlov, 1977). Hexagonal pits are rare and are a combination of positive and negative trigons (Evans and Sauter, 1961).

Currently, no primary surface features of cuboid diamonds are known, however secondary surface features may be present and include negatively (45°orientation to crystal face) and positively (same orientation as crystal face) oriented tetragonal pits (tetragons) (Robinson, 1979).

Dodecahedral diamonds lack primary surface features because they are a product of resorption of the primary forms of diamond. Secondary surface features on dodecahedral diamonds include: terraces, hillocks, pyramidal hillocks, drop-shaped hillocks, corrosion sculpture, shallow depressions, and micro-disk patterns (Robinson, 1979). Terraces are 3-or 6-sided concentric bands that develop around the 3-fold symmetry axes of dodecahedral diamond faces (Moore and Lang, 1974) and represent the exhumation of octahedral growth layering during resorption. Hillocks also form around the 3-fold axes of dodecahedral diamond faces and also relate to exhumation of primary growth layers; pyramidal hillocks convert to drop-shaped hillocks with increasing resorption (Tappert and Tappert, 2011). Corrosion sculpture in the form of elliptical or curved pits, and shallow depressions with flat bottoms are caused by late stage etching that postdates the formation of terraces and hillocks. Micro-disks are raised circular disks which likely form due to either gaseous or liquid micro-bubbles protecting

the diamond from etchants during kimberlite ascent and final emplacement (Pandeya and Tolansky, 1961).

Surface features that are not restricted to any particular diamond shape include: plastic deformation lines, ruts, circular micro-pits, frosting, and graphite coatings (Robinson, 1979). Plastic deformation is the dislocation of atoms and the formation of vacancies in the diamond crystal lattice, formed in response to stress (eg., Phaal 1964; Fisher et al., 2009). Plastic deformation may be present on diamond surfaces as single or multiple intersecting lines, with variable spacing and may run along a portion or around the whole diamond (Harris, 1987), these lines are typically on (111) faces along (011) planes (Fisher et al., 2009). Orlov (1977) speculated that ruts form on diamonds at the same time in the mantle that diamondiferous xenoliths are broken up, with fluids penetrating the xenoliths and causing "etch channels" on the diamond surface, that do not follow any crystallographic orientation but are likely related to pre-existing planes of weakness. Micro-pits (circular pits) are caused by late stage etching that postdates the formation of terraces and hillocks (Tappert and Tappert, 2011). Small etch effects result in a roughening of the surface, which may cause diamonds to appear opaque instead of translucent (Wilks, and Wilks, 1991) giving the diamond a frosted appearance.

3.1.4 Diamond Resorption:

Diamond may experience resorption during mantle residence and kimberlite ascent. The dissolution of diamond occurs when the amount of particles leaving the crystal surface is greater than what is being added

(Sunagawa, 1981). The extent of resorption can be identified through characteristic morphologies and surface features: octahedral and cuboid diamonds gradually convert to dodecahedral morphologies (Harris et al., 1975). Certain surface features, such as corrosion sculpture, shallow depressions and microdisk patterns, can be used to constrain the timing of resorption, whether it was early or late stage during kimberlite emplacement (Robinson et al., 1989).

The extent of resorption of a diamond, whether it is weak, moderate, strong or uneven, is noted. Weak resorption is identified as rough surfaces or minor resorption features, moderate resorption is defined as one or more resorption features present on the diamond and strong resorption is identified when there is significant rounding of the diamond edges and faces. Strong resorption leads to partially (od or do) or completely dodecahedral morphology. Uneven resorption creates regions with definite differences in level of resorption on a single diamond. In extreme cases diamond may exhibit pseudohemimorphism, or "half diamond resorption". Pseudohemimorphic diamond forms when part of the diamond is enclosed in a xenolith and therefore protected from the oxidizing kimberlitic fluid, while the portion that is exposed shows resorption features such as dodecahedral rounding and terraces, whereas the enclosed protected portion remains flat faced and sharp edged (Robinson, 1979).

3.1.5 Diamond Breakage:

Diamond breakage may occur during mantle residence, during kimberlite ascent and emplacement or during sampling procedures. Diamonds that

experience breakage during mantle residence or kimberlite ascent usually exhibit resorption or etch features on the broken surfaces, whereas breakage occurring post emplacement typically has sharp edges and fresh breakage surfaces.

For the Chidliak diamonds, whether breakage occurred pre- or post-diamond resorption was noted. Fresh diamond breakage surfaces are not likely due to processing of the kimberlite samples at the Saskatchewan Research Council as a non-destructive method (caustic fusion) is used to liberate the diamonds from the surrounding kimberlite material.

3.1.6 Cathodoluminescence:

Ninety-four diamonds were imaged using cathodoluminescence (CL); CL allows for the identification of internal growth structures, with the differences in luminosities being related to differences in concentrations of impurities and defects (Wilks and Wilks, 1991). Common blue CL is generally assigned to either the A-band (a broad band feature centred at 435 nm that is related to dislocations in the diamond lattice), or the N3 centre (for naturally occurring centre 3 but related to the nitrogen N3 centre) at 415.2 nm (Zaitsev 2001 and references therein). Internal growth structures reveal the stages of diamond growth and resorption.

3.2 Physical Characteristics of Diamonds from Kimberlite CH-7:
3.2.1 Color:

The majority of diamonds are colorless (45.7%) followed by light brown (16.2%). Minor colors (<10%) include light grey (7.6%), brown (5.7%), very light brown (4.8%), bright yellow (2.9%), light yellow, dark yellow, grey, mixed-color diamonds of brown/grey and colorless/light brown (1.9% each) (Table 3.1). Very

minor colors (1 diamond =1% each) are light green-grey, cloudy light-grey, light brown/pink, dark grey/colorless, grey/colorless, light brown/dark grey, light brown/grey and then a diamond exhibiting three colors light brown/grey/colorless. Small inclusions (typically black or grey) are present in 28% of diamonds.

3.2.2 Shape:

Diamonds from kimberlite CH-7 are predominantly irregular (41%), which is followed closely by octahedral fragments (29.5%) (Table 3.1). Minor shapes (<10%) include octahedra (8.6%), dodecahedral fragments, octahedral aggregates (3.8% each), do, do-aggregates, do-fragments (1.9% each) and one sample each (=1%) of an aggregate, cuboid, cuboid aggregate, dodecahedroid, macle, od, od-fragment and octahedral aggregate fragment.

Sample ID	Sieve Size (µm)	Weight (ng)	Color	Shape	Stacked growth layers	Shield shaped laminae	Trigons	Hexagons	Tetragons	Hillocks	Terraces	Etching	Pits	Ruts	Corrosion Sculpture	Plastic Deformation	Inclusion	Resorption	Broken No Resorption	Broken with Resorption
CH6-1	600	1220	colorless	do-agg	y		y	y	y	y			y		y			pseudohemimorphic		
CH6-2	600	680	cloudy	od			y -/+				y				y			moderate		
CH6-3	600	770	colorless	o	y	y	y -			y								moderate		
CH6-4	600	980	lyellow	dodec								y					y	moderate		
CH6-5	600	570	colorless	dodec (flattened)		y								y				moderate		
CH6-6	600	1020	colorless	od-agg	y	y	y	y		y	y	y			y		y	local, mod	y	
CH6-7	600	910	colorless	dodec macle			y				y	y					y	moderate	y	y
CH6-8	600	1220	colorless	od-agg	y		y			y	y	y		y			y	local, strong	y	
CH6-9	600	430	colorless	I			y			y	y	y	y					moderate	y	y
CH6-10	600	510	colorless	o-agg		y	y	y		y	y	y					y	local, mod	y	y
CH6-11	425	340	dyellow	cf					y -	y								local, mod		y
CH6-12	425	340	dyellow	c					y	y		y						local, weak		y
CH6-13	425	380	dyellow	od			y		y	y	y						y	strong		
CH6-14	425	440	lbrown	od			y -/+			y	y							strong		
CH6-15	425	310	colorless	agg			y+		y	y	y							strong	y	
CH6-16	425	410	colorless	od-agg	y		y			y	y	y		y			y	moderate		
CH6-17	425	310	colorless	I						y		y			y		y	local, mod	y	
CH6-18	425	340	lbrown	o		y	y -			y		y			y		y	pseudohemimorphic		
CH6-19	425	200	lbrown	of	y		y	y				y					y	local, weak		
CH6-20	425	440	lyellow	c					y -									slightly re-entrant		
CH6-21	425	230	colorless	dodec						y								strong		
CH6-22	425	440	colorless	I			y -/+			y		y		y				local, mod	y	y
CH6-23	425	443	yellow	cf					y	y						y		strong		y
CH6-24	425	340	brown	I			y					y		y					y	
CH6-25	425	130	lyellow	I																
CH6-26	425	120	colorless	I															y	
CH6-27	425	160	colorless	I						y	y	y						moderate	y	
CH6-28	425	440	yellow	dodec-agg														strong	y	
CH6-29	425	360	lbrown	od			y			y	y						y	local, strong	y	
CH6-30	425	290	colorless	I						y	y	y					y	moderate	y	
CH6-31	425	190	cloudy-grey (opaque)	m									y							
CH6-32	425	182	colorless	I			y										y	local, weak	y	
CH6-32b	425	135	colorless	I		y	y -											moderate	y	
CH6-33	425	187	colorless	of	y							y						weak	y	
CH6-34	300	126	brown	I			y			y							y	local, mod		y
CH6-35	300	78	bright yellow	thh						y								moderate		
CH6-37	300	191	colorless	I								y					y	moderate		y
CH6-38	300	148	colorless	I			y			y		y						moderate	y	
CH6-39	300	97	colorless	od	y					y	y	y		y				strong	y	

29

Sample ID	Sieve Size (μm)	Weight (ng)	Color	Shape	Stacked growth layers	Sheild shaped laminae	Trigons	Hexagons	Tetragons	Hillocks	Terraces	Etching	Pits	Ruts	Corrosion Sculpture	Plastic Deformation	Inclusion	Resorption	Broken No Resorption	Broken with Resorption
CH6-40	300	70	colorless	I			y					y						local, weak	y	
CH6-41	300	53	vl yellow	I														local, weak	y	
CH6-42	300	213	yellow	dodec frag					y	y								strong	y	
CH6-43	300	120	colorless	od			y			y				y				mod-strong	y	
CH6-44	300	49	colorless	I						y							y	mod	y	
CH6-45	300	83	lgreen-yellow	c					y			y						moderate		
CH6-46	300	171	colorless	c					y -			y						mod-strong		
CH6-47	300	91	colorless	dodec (flattened)						y		y						strong	y	
CH6-48	300	131	colorless	I						y								moderate		
CH6-49	300	110	yellow	od							y							moderate		
CH6-50	300	54	grey	of			y							y				mod-strong		
CH6-51	300	142	colorless	do	y		y -							y			y	local, weak		
CH6-52	300	180	colorless	I						y		y		y				moderate	y	
CH6-53	300	127	colorless	of	y	y	y		y		y	y		y				local, strong	y	
CH6-54	300	61	grey	of	y		y -			y			y	y				mod-strong	y	
CH6-55	300	127	colorless	of		y				y				y				moderate	y	
CH6-56	300	61	colorless	I														moderate	y	
CH6-57	300	85	black	of		y							y	y				moderate	y	
CH6-58	300	101	bright yellow	cf						y		y		y				weak-mod	y	
CH6-59	300	124	colorless	I						y		y		y				moderate		
CH6-60	300	99	colorless	I						y								moderate	y	
CH6-61	300	63	colorless	I								y	y				y	weak	y	y
CH6-62	300	63	bright yellow	I								y						weak	y	y
CH6-63	300	73	colorless	of			y					y		y					y	
CH6-64	300	25	colorless	I															y	
CH6-65	300	139	lbrown	I						y		y		y				moderate	y	y
CH6-66	300	96	vl brown	of	y							y	y			y		weak	y	y
CH6-67	212	48	colorless	I								y						moderate		
CH6-68	212	41	colorless	I						y								moderate	y	y
CH6-69	212	25	lgrey (cloudy)	dodec (elongate)			y			y	y	y	y				y	strong	y	
CH6-70	212	65	dgrey	I-agg f							y	y						strong	y	
CH6-71	212	39	colorless									y								
CH6-72	212	43	lgrey (cloudy)	dodec (rounded)			y											strong		
CH6-73	212	28	vl yellow	o-agg			y											weak		
CH6-74	212	27	colorless	I			y			y	y	y						moderate	y	y
CH6-75	212	25	vl brown	I			y					y	y					weak	y	y
CH6-76	212	36	lyellow	I						y								moderate	y	y
CH6-77	212	31	colorless	f															y	
CH6-78	212	79	colorless	f															y	

Sample ID	Sieve Size (µm)	Weight (ng)	Color	Shape	Stacked growth layers	Sheild shaped laminae	Trigons	Hexagons	Tetragons	Hillocks	Terraces	Etching	Pits	Ruts	Corrosion Sculpture	Plastic Deformation	Inclusion	Resorption	Broken No Resorption	Broken with Resorption
CH6-79	212	67	colorless	I			y			y		y						moderate		
CH6-80	212	43	lbrown	of		y			y -	y		y		y				moderate	y	
CH6-81	212	33	colorless	cf														moderate	y	
CH6-82	212	49	cloudy grey	cf								y		y					y	
CH6-83	212	37	cloudy green-grey	I			y					y								y
CH6-84	212	47	lbrown	I	y							y		y						y
CH6-85	212	45	colorless	I						y								moderate	y	y
CH6-86	212	20	colorless	I																
CH6-87	212	38	dgrey	I			y			y		y	y					weak		y
CH6-88	212	30	lyellow	do						y					y			moderate		
CH6-89	212	16	colorless	f															y	
CH6-90	212	13	colorless	f															y	
CH6-91	212	24	colorless	I								y		y		y			y	y
CH6-92	212	7	colorless	I								y							y	y
CH6-93	212	23	lyellow	dodec frag	y		y			y		y						strong		y
CH6-94	212	14	lyellow	of			y											pseudohemimorphic		y
CH6-95	212	35	colorless	dodec frag			y				y							strong		y
CH6-96	212	47	colorless	of	y		y -					y							y	y
CH6-97	212	33	lbrown	of	y							y								
CH6-98	212	17	colorless	I								y								
CH6-99	212	28	colorless	I														weak		
CH6-100	212	10	colorless	I															y	
CH6-101	212	38	cloudy	c						y									y	
CH6-102	212	7	colorless	I														moderate	y	
CH6-103	212	12	colorless	f						y										y
CH6-104	212	23	colorless	dodec frag	y	y	y			y		y						strong	y	
CH6-105	212	40	colorless	I						y		y		y				moderate	y	
CH5-1	600	840	colorless/lbrown	of		y	y -/+													
CH5-2	600	830	lbrown	dodec			y -/+			y				y		y	y	moderate		
CH5-3	600	830	lbrown	o-agg	y		y					y				y	y	local, weak		
CH5-4	600	531	lbrown	I			y			y		y				y		moderate		
CH5-5	425	390	vl brown	of		y	y -/+			y	y	y					y	weak-mod	y	
CH5-6	425	250	grey	I			y					y	y					weak		
CH5-7	425	330	lgrey	I		y	y			y		y					y	local, mod		y
CH5-8	425	210	colorless	I			y -/+					y					y	local, mod		y
CH5-9	425	290	brown	of	y		y -/+	y		y		y					y	local, mod		
CH5-10	425	230	lgrey	dodec-frag		y	y			y		y				y	y	strong		y
CH5-11	425	186	colorless/lbrown	I						y		y	y				y	moderate		y
CH5-12	425	211	grey	I			y			y		y	y	y			y	mod-strong		y

Sample ID	Sieve Size (μm)	Weight (ng)	Color	Shape	Stacked growth layers	Sheild shaped laminae	Trigons	Hexagons	Tetragons	Hillocks	Terraces	Etching	Pits	Ruts	Corrosion Sculpture	Plastic Deformation	Inclusion	Resorption	Broken No Resorption	Broken with Resorption
CH5-13	425	180	colorless	o	y	y				y		y					y	moderate		
CH5-14	425	570	brown/grey	I			y					y					y	local, weak		
CH5-15	425	420	brown	o-agg	y		y -/+	y		y		y				y		moderate		
CH5-16	300	115	colorless	of	y		y			y						y		weak-mod	y	
CH5-17	300	59	colorless	I						y		y				y	y	moderate		y
CH5-18	300	185	lgrey	c-agg					y -									weak		
CH5-19	300	183	colorless	dodec-frag							y					y		strong		
CH5-20	300	134	lbrown	of	y		y			y		y		y		y		weak-mod		y
CH5-21	300	132	lbrown/pink	of	y		y -/+					y				y		weak		
CH5-22	300	98	colorless	of	y		y -					y		y			y		y	
CH5-23	300	100	colorless	I			y -					y						moderate		y
CH5-24	300	88	colorless	o	y	y	y											moderate		
CH5-25	300	85	colorless	I								y						weak		y
CH5-26	300	142	colorless	do-agg	y		y -	y		y								pseudohemimorphic	y	
CH5-27	300	128	colorless	of	y		y -													y
CH5-28	300	73	lyellow	I			y				y							local, weak		y
CH5-29	300	300	brown	of	y		y -			y	y	y				y	y	local, mod		
CH5-30	300	71	vl brown	od			y					y				y		strong		y
CH5-31	300	60	lbrown	I				y				y							y	
CH5-32	300	104	vl brown	o-agg frag	y		y					y				y		local, weak		
CH5-33	300	79	brown/grey	of	y		y -					y					y	weak		y
CH5-34	300	72	brown	do-frag		y	y			y		y					y	pseudohemimorphic		
CH5-35	300	69	lgrey	of	y		y					y						local, weak		y
CH5-36	300	33	colorless	m			y										y			
CH5-37	300	70	lbrown	of	y							y					y	weak		y
CH5-38	300	52	lgrey (cloudy)	I			y											weak		y
CH5-39	300	58	bright yellow	I			y											local, weak		
CH5-40	300	105	colorless	I								y								
CH5-41	300	66	lgrey	od-frag			y					y		y		y		weak		y
CH5-42	300	67	lyellow	I			y					y					y	local, weak		y
CH5-43	300	86	lgrey	I								y		y				moderate		y
CH5-44	300	34	colorless	I				y		y			y					moderate	y	
CH5-45	300	59	lbrown	o-agg	y	y	y -/+					y						moderate		
CH5-46	300	184	colorless	o	y		y -					y						moderate	y	
CH5-47	300	194	colorless	I		y								y						
CH5-48	300	67	dyellow	do			y					y				y		moderate		
CH5-49	300	85	colorless	do	y	y	y -	y		y					y			pseudohemimorphic		y
CH5-50	300	70	colorless	do-agg	y	y	y					y					y	strong		y
CH5-51	300	53	colorless	I		y	y					y						strong		y

Sample ID	Sieve Size (µm)	Weight (ng)	Color	Shape	Stacked growth layers	Shield shaped laminae	Trigons	Hexagons	Tetragons	Hillocks	Terraces	Etching	Pits	Ruts	Corrosion Sculpture	Plastic Deformation	Inclusion	Resorption	Broken No Resorption	Broken with Resorption
CH5-52	300	114	dyellow	c					y -			y						weak		
CH5-53	300	73	colorless	I			y										y	strong		y
CH5-54	300	71	colorless	I								y						strong	y	
CH5-55	300	50	colorless	I												y			y	y
CH5-56	300	92	lbrown	I		y										y		local, mod	y	y
CH5-57	300	127	colorless	do	y	y	y -				y							pseudohemimorphic		
CH5-58	212	53	colorless	o	y		y -			y		y		y		y		local, mod		
CH5-59	212	67	lbrown	I			y -/+													
CH5-60	212	54	colorless	of	y		y					y				y		local, weak		y
CH5-61	212	33	colorless	of(twin)	y							y				y				y
CH5-62	212	51	lbrown	I								y						local, weak		y
CH5-63	212	52	colorless	of	y		y													
CH5-64	212	42	colorless	of	y		y -					y					y	local, weak		y
CH5-65	212	35	brown	I	y		y -										y			y
CH5-66	212	62	colorless	I															y	
CH5-67	212	26	dgrey/colorless	I			y -					y				y	y			
CH5-68	212	32	lbrown	I			y	y				y		y			y	weak	y	y
CH5-69	212	19	colorless	I								y					y	local, weak	y	
CH5-70	212	18	lbrown	of	y	y						y	y					local, mod	y	y
CH5-71	212	21	colorless	of-agg	y							y					y	weak	y	
CH5-72	212	26	colorless/grey	agg-frag			y					y		y				weak	y	
CH5-73	212	9	colorless	I			y											weak		
CH5-74	212	28	lbrown/grey/colorless	of	y		y													y
CH5-75	212	17	lbrown/grey	I								y						local, weak		y
CH5-76	212	19	lbrown/dgrey	I								y	y	y				local, weak		
CH5-77	212	18	lgrey	I	y		y					y		y			y	weak		y
CH5-78	212	11	lgreen-grey	of	y		y -					y	y	y			y		y	
CH5-79	212	50	colorless	of	y		y													
CH5-80	212	34	colorless	of(elongate)	y		y -					y				y		moderate		y
CH5-81	212	32	lbrown	I						y		y				y				y
CH5-82	212	36	colorless	o	y		y					y								
CH5-83	212	60	colorless	I			y					y						micro-disk	y	
CH5-84	212	46	colorless	dodec-frag		y	y					y		y		y		strong		
CH5-85	212	23	lbrown	of	y		y					y				y				
CH5-86	212	42	colorless	of	y		y												y	
CH5-87	212	21	colorless	of	y													weak		y
CH5-88	212	49	colorless	o	y							y								
CH5-89	212	36	bright yellow	of	y							y		y				weak	y	
CH5-90	212	50	colorless	o	y															

Sample ID	Sieve Size (µm)	Weight (ng)	Color	Shape	Stacked growth layers	Shield shaped laminae	Trigons	Hexagons	Tetragons	Hillocks	Terraces	Etching	Pits	Ruts	Corrosion Sculpture	Plastic Deformation	Inclusion	Resorption	Broken No Resorption	Broken with Resorption
CH5-91	212	37	colorless	o	y	y											y	moderate		
CH5-92	212	21	lbrown	o (elongate)	y								y							
CH5-93	212	44	bright yellow	l										y						y
CH5-94	212	24	colorless	of			y -					y						moderate		y
CH5-95	212	58	brown	l						y		y				y		weak-mod	y	y
CH5-96	212	15	lbrown	of	y		y -			y		y	y			y		weak		y
CH5-97	212	36	colorless	of			y -											weak	y	y
CH5-98	212	38	lbrown	of	y							y	y			y			y	
CH5-99	212	27	colorless	l						y		y						weak-mod	y	
CH5-100	212	28	vl brown	l								y							y	
CH5-101	212	14	vl brown	of	y							y	y							y
CH5-102	212	41	colorless	of	y							y	y	y						
CH5-103	212	26	colorless	do-frag	y		y			y		y						moderate		y
CH5-104	212	36	colorless	dodec frag						y	y							strong		y
CH5-105	212	36	lgrey	l								y								y

Table 3.1. Physical Characteristics of Chidliak diamonds. If the surface feature is present it is indicated by a 'y'. For trigons and tetragons, if the orientation is known it indicated by 'y – ' for negatively oriented pits, 'y +' for positively oriented pits, and 'y -/+' for both orientations. Blanks mean the surface feature wasn't observed.

34

3.2.3 Surface Features:

Trigons occur on 71% of octahedral diamonds (including octahedral fragments, octahedral aggregates, do, and do-aggregates), and on the single macle. Stacked growth layers are present on 86% of octahedral diamonds, whereas shield shaped laminae are much less common at 17%. Both flat bottomed and pyramidal bottomed trigons are observed. Negative and positive trigons are observed on 40% and 12% of octahedral diamonds, respectively. Negatively oriented tetragons are observed on 100% (N=2) of cubiod diamonds (including cuboid aggregates). Hillocks are present on 67% and terraces on 25% of dodecahedral diamonds (including od, dodecahedral aggregates and fragments). Hexagons are found on 4% of irregular diamonds and on 10% of octahedral diamonds. Diamond CH5-12 has circular pits that were identified during SEM imaging, with roughly hexagonal outlines. On diamond CH5-9 (of) there is an example of a negative trigon inside the hexagonal pit (Figure 3.1). Plastic deformation lines are present on 24% of diamonds, ruts are identified on 16%, while corrosion sculpture and micro-disk patterns are found on 1% of diamonds.
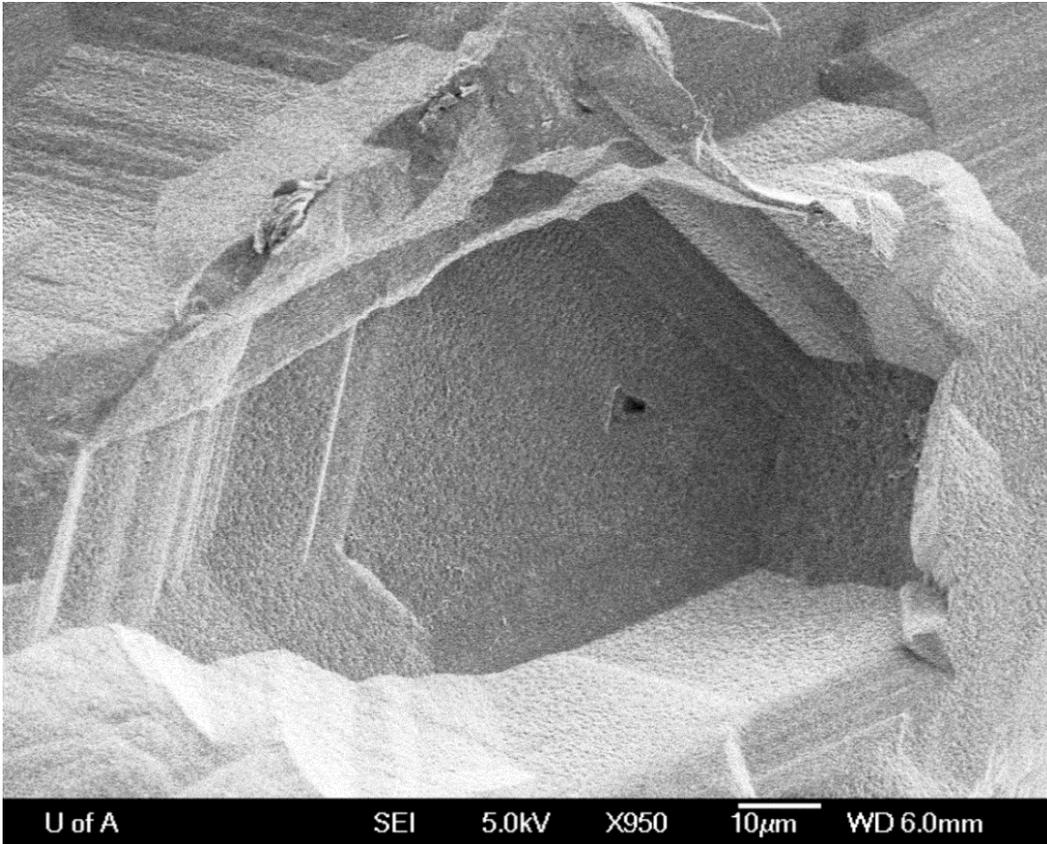
Figure 3.1. SEM image of a hexagonal pit on diamond CH5-9 with a negative trigon in the bottom of the pit.

3.2.4 Breakage and Resorption:

Kimberlite sample P5500 was collected from subcrop and float on the surface of pipe CH-7. 25% of diamonds show breakage surfaces without subsequent resorption, and 44% of the diamonds show breakage surfaces with subsequent resorption or etching. 56% of diamonds show some degree of resorption including rounding, and rough surfaces in addition to the surface features attributed to resorption (see above).
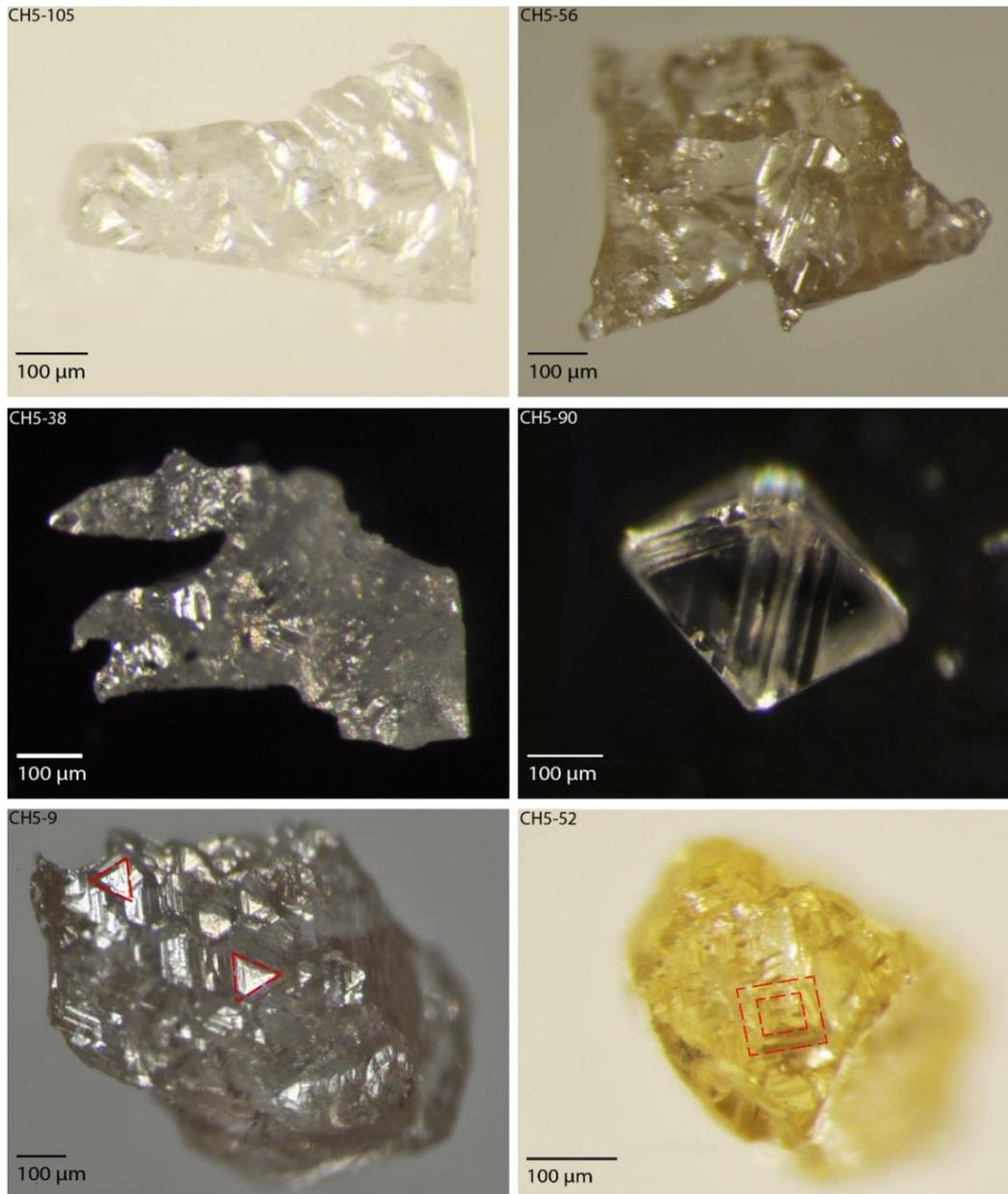
Figure 3.2. Examples of physical characteristics of diamonds from kimberlite CH-7, including: a colorless irregular diamond (CH5-105), a light brown irregular diamond (CH5-56), a cloudy light grey irregular diamond with rough surfaces (CH5-38), a colorless octahedral diamond with stacked growth layers (CH5-90), a brown octahedral fragment with both orientations of trigons (CH5-9) and a dark yellow cube with negative tetragons (CH5-52).

3.3 Physical Characteristics of Diamonds from Kimberlite CH-6:

3.3.1 Color:

The majority of diamonds are colorless (58.1%) followed by light brown (7.6%) and light yellow (6.7%). Yellow diamonds are 3.8%, whereas dark yellow, bright yellow, and cloudy light grey are 2.9% each. Very light yellow, very light brown, brown, dark grey, grey, and cloudy are 1.9% each. Very minor colors (1%=1 diamond each) are light green-yellow, cloudy grey, black, and cloudy green-grey. Small inclusions (typically black or grey) are identified in 18% of diamonds.

3.3.2 Shape:

Similar to diamonds from kimberlite CH-7, diamonds from kimberlite CH-6 are also predominantly irregular (41.2%) followed by octahedral fragments (12.4%). Minor shapes include od (6.7%), dodecahedral diamonds (5.7%), fragments (5.7%), cuboid (4.8%), cuboid fragments (4.8%), dodecahedral fragments (3.8%), od aggregates (2.9%) octahedral, octahedral aggregates, and do diamonds (1.9% each). Morphologies observed for only one diamond (1%) each are: do aggregate, dodecahedral macle, dodecahedral aggregate, irregular aggregate, macle, and a tetrahexahedroid.
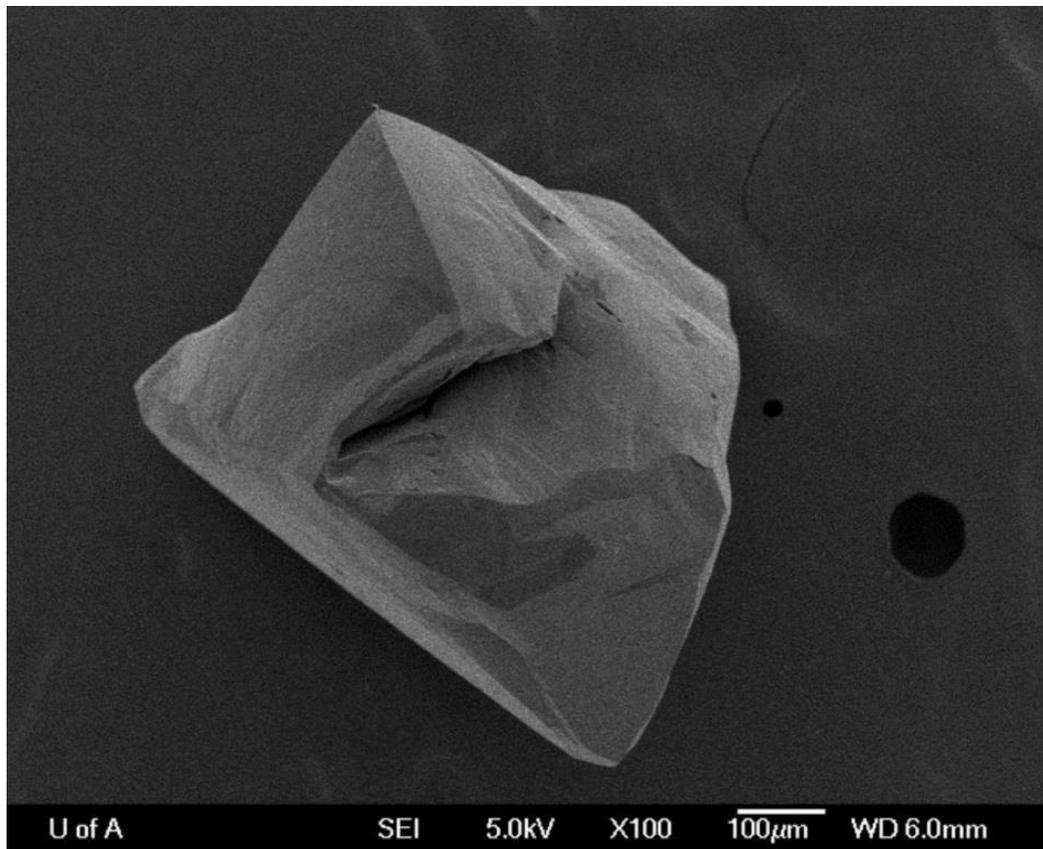
Figure 3.3. An SEM image of diamond CH6-18 clearly showing pseudohemimorphism (half-resorbed) for an originally octahedral diamond. The sharp-edged portion of the diamond was protected from kimberlitic fluid by an enclosing xenolith/mineral, while the round portion was exposed and subsequently resorbed.

3.3.3 Surface Features:

Diamonds display trigons on 67% of octahedral diamonds (including octahedral fragments, octahedral aggregates, do, and do-aggregates). Negative trigons are present on 25% of octahedral diamonds, whereas no positive trigons are identified on any octahedral diamonds. Both orientations of trigons are found on a single irregular diamond without a primary octahedral face. Stacked growth layers are present on 55% of octahedral diamonds, whereas shield shaped laminae are found on 35%. Tetragons are present on 70% (N=10) of cuboid diamonds (including cuboids and cuboid fragments). On dodecahedral diamonds (including

od, dodecahedral macles, dodecahedral aggregates and fragments) hillocks are present on 59% and terraces on 55%. Plastic deformation is visible on 3% of diamonds, corrosion sculpture is present on 6% of diamonds, whereas pits and ruts are present on 10% and 2% of diamonds, respectively.

3.3.4 Breakage and Resorption:

Kimberlite sample P6807 was collected from NQ core drilled from pipe CH-6. 52% of diamonds have breakage surfaces with no resorption and 25% exhibit some level of resorption on breakage surfaces. 55% of diamonds show some characteristics of resorption (see above).
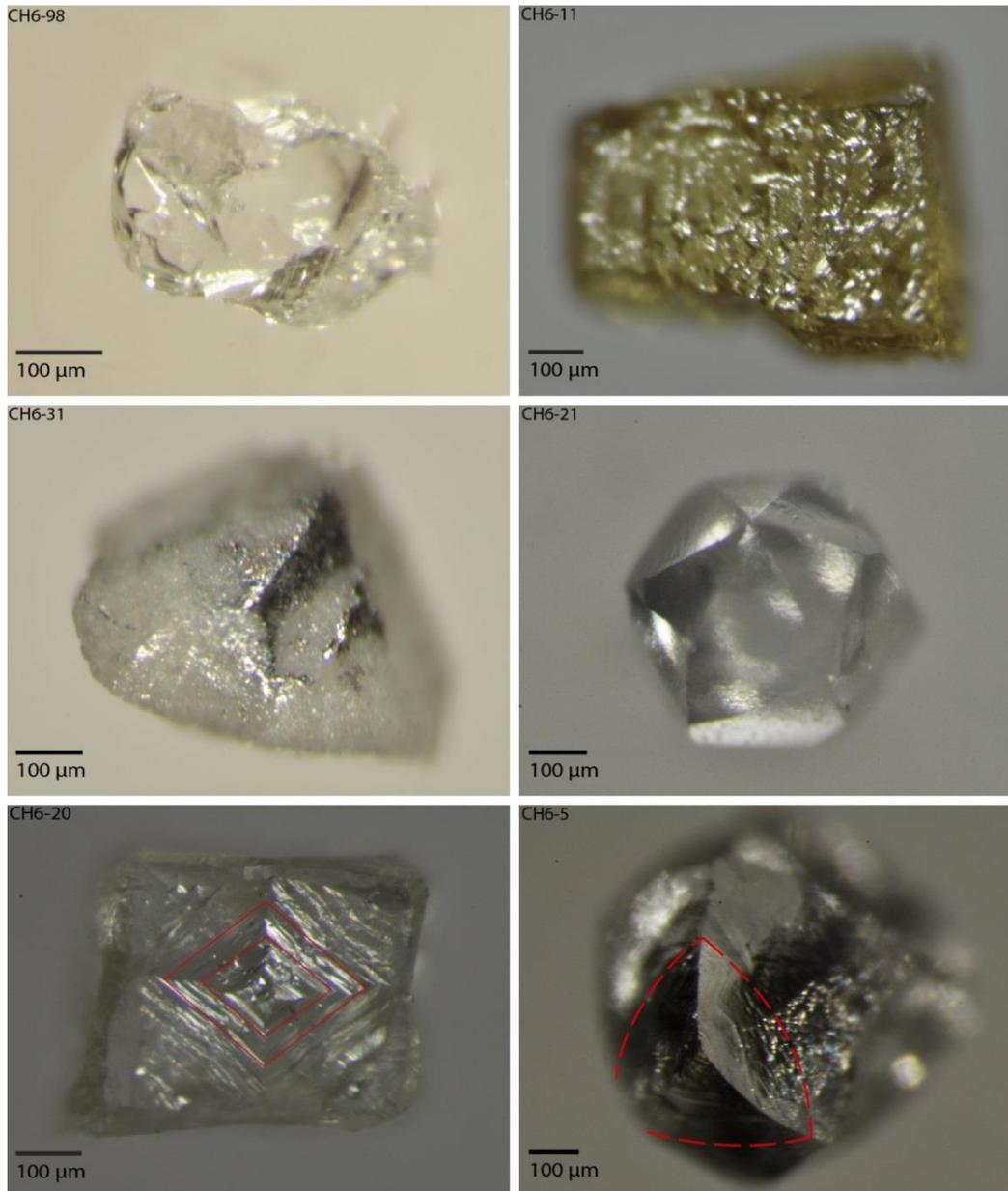
Figure 3.4. Examples of physical characteristics of diamonds from kimberlite CH-6 including: a colorless irregular diamond (CH6-98), a yellow cuboid (CH6-11), an opaque macle with graphite surface coating (CH6-31), colorless dodecahedron (CH6-21), a light yellow cube with negative tetragons and rounded edges (CH6-20) and a colorless dodecahedron with terraces and pyramidal hillocks (CH6-5).

3.4 Cathodoluminescence Imaging:

The diamonds imaged by cathodoluminescence (CL) in the current study were not oriented on specific growth faces due to mounting procedures. In addition, as multiple diamonds were polished in single mounts, sections through

the crystal centres were only achieved in rare cases. Such random sections

through only a part of diamond crystals introduce artificial complexities to the CL

images.

Identified types of CL for Chidliak diamonds include: (1.) "hiatus", (2.)

"homogenous", (3.) "agate-like banding", (4.) "octahedral", (5) "cuboid" and (6.)

"complex" (Figure 3.5). "Hiatus" involves abrupt and strong changes in CL

response, and are usually associated with resorption fronts (truncation of growth

bands) or a sharp change in diamond growth. Diamonds with "homogenous" CL

show neither growth bands, nor strong changes in CL response. "Agate-like

banding" is present as multiple narrow growth bands with strong changes in CL

response. "Octahedral" and "cuboid" CL types have growth bands that can be

identified based on the angles between growth layers, and by a hummocky

appearance for cuboid growth. "Complex" CL is either chaotic, mixed habit

growth, or the mode of growth is unclear; "complex" internal growth structures

could be a result of diamond polishing in random orientations adding artificial

complexity.
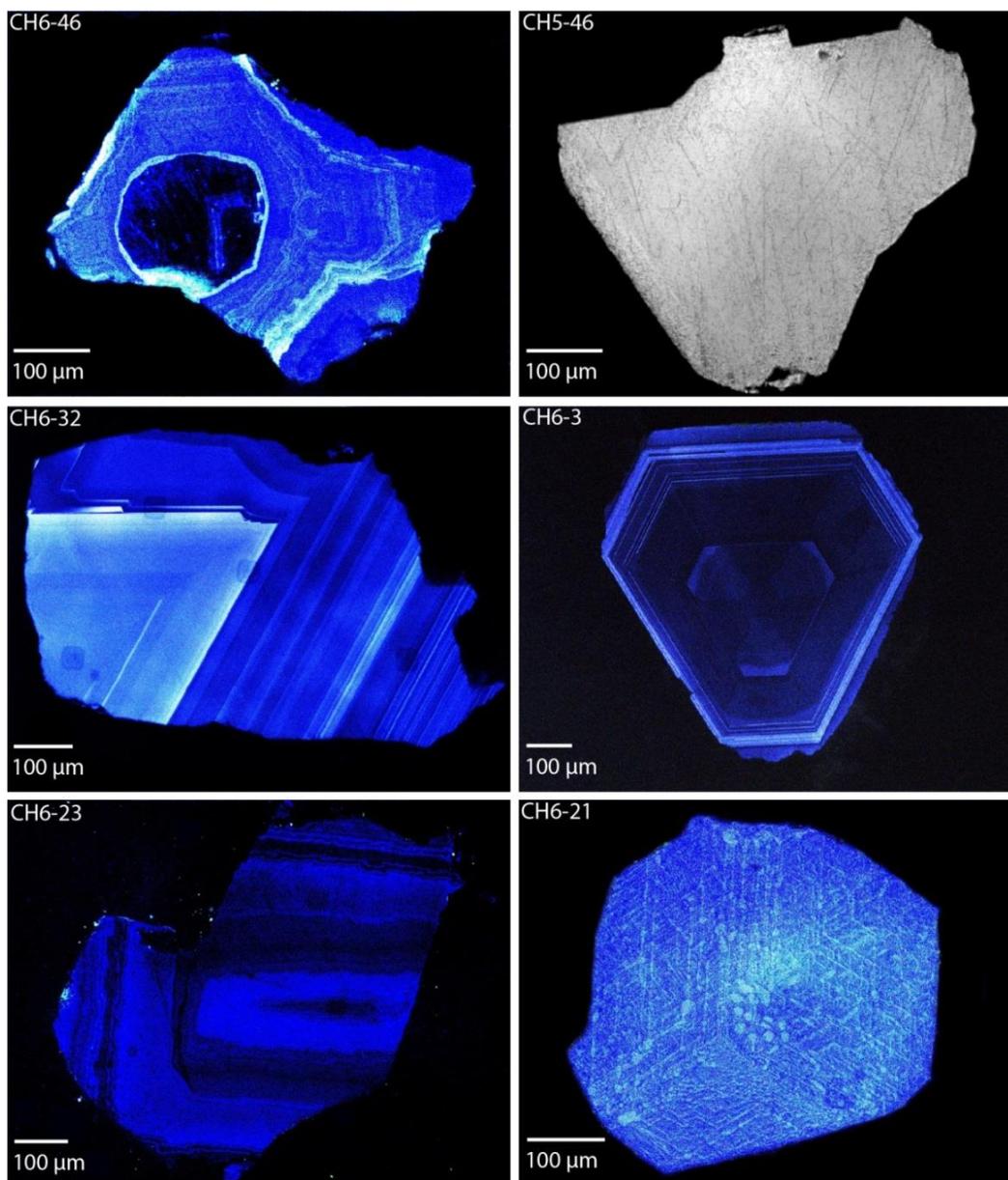
Figure 3.5. Examples of CL internal growth structures, blue images are obtained using the Gatan Chroma CL detector, while the grey scale image was taken using the Robinson wide spectrum CL detector. Diamond CH6-46 exhibits "hiatus" CL, from the dark rounded CL in the centre of the diamond to brighter CL with concentric growth bands. Diamond CH5-46 is "homogenous" CL, diamond CH6-32 shows "agate-like banding". Diamond CH6-3 is polished on a (111) face and has mixed growth in the central portion of the diamond: three cuboid and three octahedral growth sectors are characteristic of mixed habit growth when polished along (111) faces. The external concentric growth bands represent octahedral growth. Diamond CH6-23 shows hummocky cuboid growth and diamond CH6-21 is an example of "complex" internal growth structures, in this case the bright colored blebs may be platelets along octahedral planes.

3.4.1 Abundance of CL Types

For diamonds from kimberlite CH-7 (N=48) the majority of internal growth is complex (50%), followed by homogenous CL (25%). Less common CL types are octahedral (8.3%), hiatus (6.3%), cuboid (4.2%), diamonds with a homogenous portion and a banded portion (4.2%), and agate-like banding (2.1%). Plastic deformation lines are present for 46% of diamonds, while resorption fronts are identified on 27% of diamonds.

Complex internal growth (24%) is also the most common CL type for diamonds from kimberlite CH-6 (N=46). Cuboid growth and homogenous CL 19.6% each) are followed closely by octahedral growth and agate-like banding (13% each). Hiatus and homogenous/banded diamonds comprise 6.5% and 4.3%, respectively, of the internal growth structures. Plastic deformation lines (24%) and resorption fronts (15%) are less common for diamonds from kimberlite CH-6.

3.5 Discussion:
3.5.1 Internal Growth Structures:

Single crystalline diamond growth occurs under conditions of relatively low carbon supersaturation, whereas fibrous diamonds, fibrous coats and polycrystalline diamonds grow much faster under higher carbon supersaturation conditions (Sunangawa, 1984; Gurney, 1989). Neither nucleation nor growth will occur as long as the solid and liquid phases are in equilibrium, changes in the environment to disrupt the equilibrium causing more particles to arrive onto the surface of the crystal must occur prior to growth (Sunagawa, 1984). Further changes in the growth environment during crystal growth can also cause complex shapes and features (Sunagawa, 1984).

Although diamonds were polished in random orientations, many of the imaged diamonds, nevertheless, show order. Diamonds showing hiatus CL either underwent resorption before the next episode of growth, or show a strong change in internal growth structures and CL response across the hiatus. Hiatus internal growth reveals that diamond resorption occurred during mantle residence, followed by at least one more episode of diamond growth. Other evidence for diamond growth in temporally distinct events is provided by truncations of growth layers followed by renewed growth on the truncated surface. The differences in imaged resorption fronts and truncated growth layers suggest that at least two resorption events took place during mantle residence. Some complex growth structures show evidence of two to three stages of growth; chaotic growth structures near the cores of some diamonds are interpreted to represent initial nucleation where particles cluster together before reaching the critical size at which point nucleation is complete and structured growth may occur (Figure 3.6) (Sunagawa, 2005). In some cases it appears that two small diamond "seeds" are joined by later overgrowths creating a single diamond. Some diamonds show brittle deformation with possible zones of strain, and one diamond shows a zone of fibrous growth impinging on agate-like banded growth. Plastic deformation lines are easily identified; up to three orientations of lines are observed and appear to be more abundant than those identified during binocular microscope diamond physical characterization.
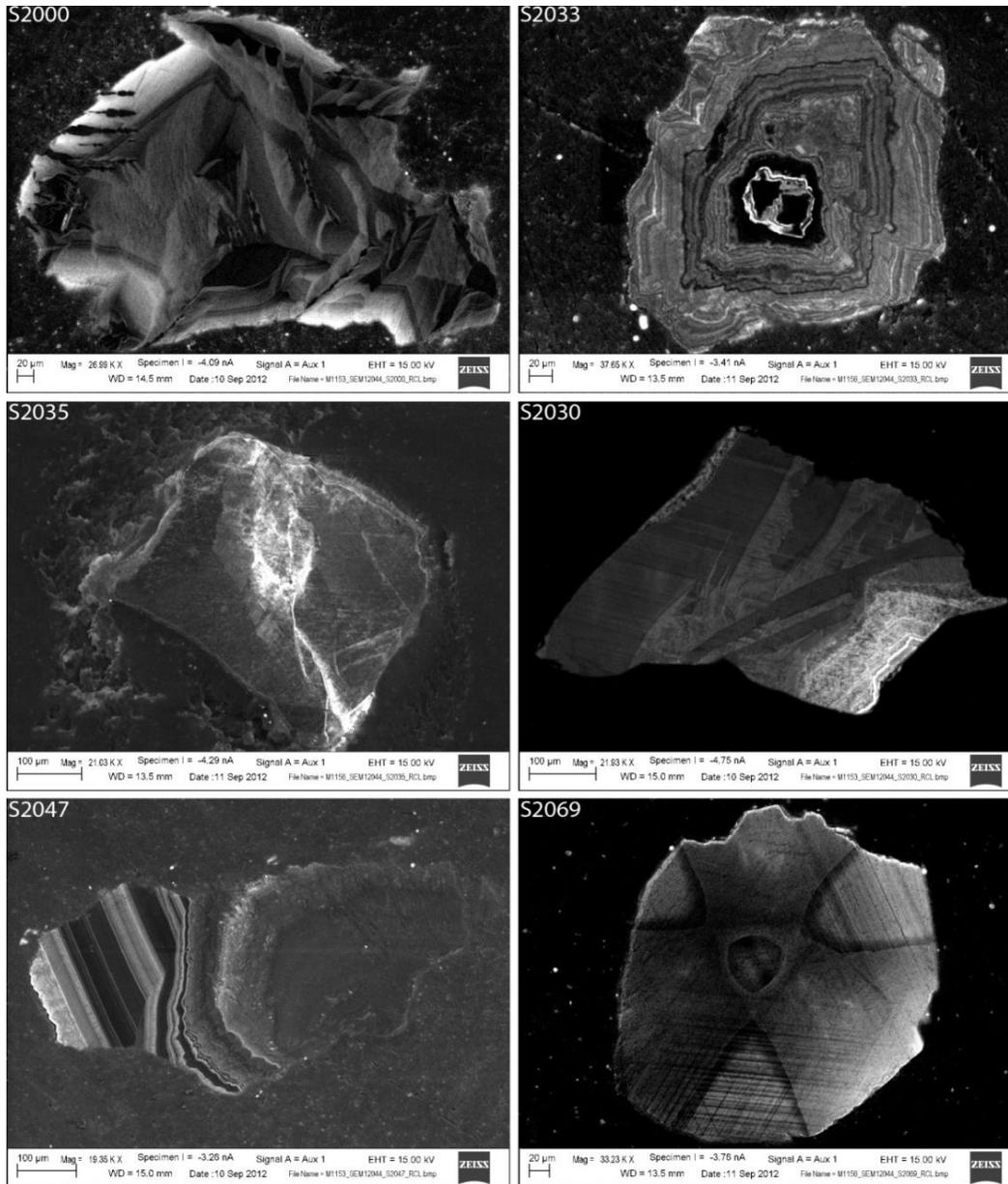
Figure 3.6. Diamond S2000 exhibits a possible chaotic nucleus region; it is a flat polished surface, with a discontinuous set of thin alternating dark and light CL bands along the bottom and left portion of the diamond. There appears to be a dislocation and offset of these growth bands in the NW section of the diamond, which intersects the growth bands in the bottom of the diamond. There is a second small fracture also intersecting the growth bands in the SW. Diamond S2033 shows two small diamonds (which may be two diamond "seeds") that are joined by later overgrowths and may represent an aggregate. Diamond S2035 and S2030 show possible zones of brittle deformation; diamond S2030 also exhibits plastic deformation lines. Diamond S2047 shows fibrous growth adjacent to "agate-like" banded growth, while diamond S2069 is a centre-cross diamond with 3 orientations of plastic deformation lines.

46

Centre-cross patterns are recognized in CL images of 5 diamonds (1 diamond from kimberlite CH-6 and 4 diamonds from kimberlite CH-7). A centre-cross originates from mixed habit growth with competing cuboid and octahedral growth sectors (Lang, 1979). The diamonds showing centre-cross patterns in this study must have been placed on octahedral faces ({111}) prior to polishing and, therefore, show only three cuboid and three octahedral growth sectors instead of the four typically observed in samples cut parallel to (100), (see Figure 3.7, from Rondeau et al. (2004)). In the case of mixed habit growth diamonds it is often seen that some sectors (commonly the cuboid sectors) pinch out and the remaining growth sectors (often the octahedral sectors) then define the external morphology.
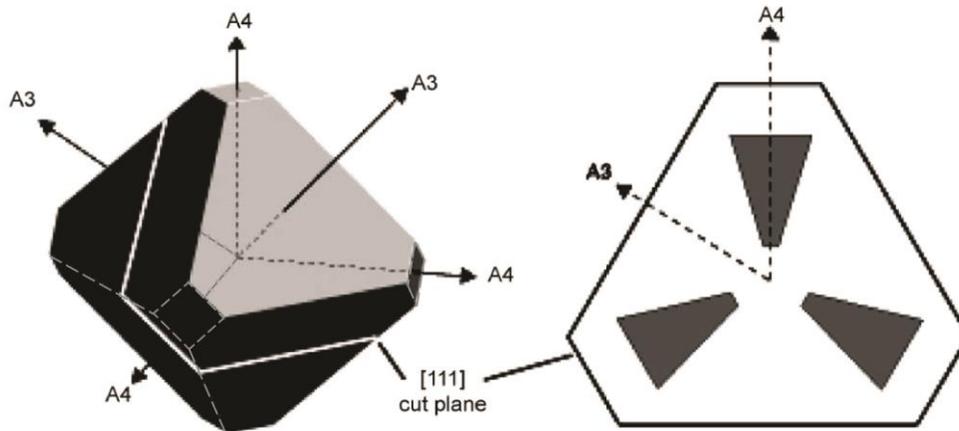
Figure 3.7. Drawing of a mixed habit growth diamond cut along an octahedral plane (111) showing equilibrium growth between cuboid (grey) and octahedral growth sectors; the abrupt straight termination of the cuboid growth sectors is simply due to growth of these sectors out of the plane of the section (Fig. 5 of Rondeau et al, 2004). In natural examples the fast growing cuboid growth sectors often pinch out and octahedral growth becomes dominant. The four-fold cuboid and the three-fold octahedral symmetry axes are labeled A4 and A3, respectively. CH6-3 (see above) shows this characteristic internal growth structure.

3.5.2 Etching:

Etching of diamond begins after genesis while the diamond is still deep in the Earth's mantle and acts on the crystal faces of diamond (eg., Orlov, 1977). The orientation of etch pits on diamond surfaces change with temperature and etchant compositions. Although the exact processes may not be agreed upon by all authors, it is well known that the majority of trigons on natural diamonds are in the negative orientation (eg., Wilks, and Wilks, 1991), and that trigons are often associated with lattice imperfections on octahedral surfaces, pyramidal trigons are specifically associated with the piercing points of dislocations (Lang, 1964); early etching produces small trigons and as it continues fewer and larger trigons develop (Omar et al., 1954).

Experiments on etching of diamond show that temperature affects the orientation of the etch pits. As kimberlite magma ascends, fluids such as CO_2 and H_2O are exsolved and can etch diamond surfaces (Harris and Vance, 1974). Evans and Sauter (1961) found that on octahedral diamonds, etching at atmospheric pressures using air, at temperatures of 850°C, produced trigons of positive orientation, while increasing the temperature to 1000°C produced negative trigons; therefore the temperature between 900-1000°C could be the threshold for orientation reversals of trigons where hexagonal pits could form. Similar results are found when using a combination of 4 parts nitrogen, 1 part oxygen plus water vapour, in that lower temperatures (850°C) produced positive trigons and higher temperatures (1250°C) produced negative trigons (Evans and Sauter, 1961). Further experiments using kimberlite melt at 1450°C showed that negatively oriented trigons formed and that, over time, the same melt (but not necessarily the

same processes) that produces trigons may also subsequently convert octahedral to dodecahedral morphologies (Frank and Puttick, 1958).

3.5.3 Resorption:

Resorption of diamond in the mantle may be caused by an influx of a hot melt, causing a rapid change in temperature and subsequent related dissolution of diamond (Bulanova, 1995). If diamond is exposed to a fluid/melt that is not supersaturated in carbon, it can dissolve into the carbon undersaturated solution (Sunagawa, 1984). For Chidliak diamonds there are cases where breakage pre-dates diamond resorption and etching; resorption on diamond breakage surface includes slight rounding of edges and roughening of surfaces. Processes that cause plastic deformation may in part be responsible for diamond breakage during mantle residence, in which whole diamonds may fragment or diamond cracks may occur (Orlov, 1977). The extent of resorption in smaller size fraction diamonds is higher when they are liberated from their host xenoliths early in the ascent of the kimberlite. Whole diamonds can effectively be eliminated from the diamond population if they are released from mantle xenoliths/xenocrysts early on during kimberlite ascent, whereas sharp-edged crystals would be released just prior to kimberlite emplacement or during processing (crushing or caustic fusion). Small diamonds have a large surface area for their volume, causing etching and resorption to act faster than for macro-diamonds released at the same time. For example, during resorption a micro-diamond would lose 50% of its original diamond volume in the same time that a macro-diamond would be resorbed by

20% (Robinson et al., 1989). Late stage liberation from the diamond hosting xenoliths could explain the presence of uneven resorption on some diamonds.

3.5.4 Sequence of Events:

Surface features and internal growth structures enable us to reconstruct the history of diamond crystals from genesis to kimberlite emplacement: initial diamond growth in some cases is documented by a chaotic nucleus region in diamond cores. This initial growth was followed by at least one episode of resorption and re-growth; during this period of new growth, stacked growth layers may form on octahedral diamonds and strain may affect the diamonds causing plastic deformation. Chidliak diamonds with ruts typically have etch features such as trigons in them, suggesting that not all ruts are late stage features; ruts containing secondary etch features, therefore, may already form during mantle residence.

Resorption ensues during mantle residence or kimberlite ascent; the observation of a negative trigon in a hexagonal pit indicates that processes forming trigons postdate that for hexagon formation. During this period of resorption, positive trigons, followed by hexagons, and then negative trigons may form; tetragons may form on cuboid faces. Rounding of stacked growth layers, creating shield shaped laminae may form on octahedral faces, hillocks and terraces may form on the resorbed faces of dodecahedral diamonds. For diamonds contained in kimberlite root zones (i.e., residing in slowly cooling magmatic kimberlite), late stage etching may attack any crystal face, creating surface features including corrosion sculpture, micro-pits, micro-disk patterns, and ruts

(Robinson et al., 1989). At some point prior to a resorption episode either during mantle residence or kimberlite emplacement some diamonds were broken and subsequently resorbed and etched. Freshly broken diamond surfaces may have formed during late stage kimberlite emplacement.

3.6 Conclusions:

Based on the internal growth structures imaged using CL, it is clear that there was a period of initial diamond growth followed by resorption, plastic deformation and then subsequent new diamond growth. Many types of diamond growth occurred, including mixed-habit, octahedral, and cuboid with some very complex growth episodes. The majority of the Chidliak diamonds are irregular, followed by octahedral fragments. Most of the diamonds are colorless, the range of observed colors indicates that there are nitrogen impurities (yellow), plastic deformation (brown colors/plastic deformation lines), and fibrous diamonds/diamonds with many submicroscopic inclusions (grey-black).

Surface features found on the diamonds indicate that both high and low temperature etching acted on the Chidliak diamonds, with low temperature etch affecting the diamond surface followed by high temperature etch. Typical late stage etching is also present on some Chidliak diamonds. Diamond breakage occurred during mantle residence or during kimberlite ascent, and also post-dates etching processes. It is clear that the Chidliak diamond suite experienced a complicated history from genesis to emplacement.

References:

Bulanova, G.P., 1995. The formation of diamond. Journal of Geochemical
    Exploration, 53(1-3): 1-23.

Evans, T. and Sauter, D.H., 1961. Etching of diamond surfaces with gases.
    Philosophical Magazine, 6(63): 429-440.

Fisher, D., 2009. Brown diamonds and high pressure high temperature treatment.
    In: S. Foley, S. Aulbach, G. Brey, H. Grütter, H. Höfer, D. Jacob, V.
    Lorenz, T. Stachel and A. Woodland (Editors), The 9th International
    Kimberlite Conference. Proceedings of the 9th International Kimberlite
    Conference, Lithos, Frankfurt, Germany: 619-624

Frank, F.C. and Puttick, K.E., 1958. Etch pits and trigons on diamond II.
    Philosophical Magazine, 3(35): 1273-1279.

Gurney, J.J., 1989. Diamonds. Kimberlites and Related Rocks (14): 935-965.

Harris, J.W., 1987. Recent physical, chemical, and isotopic research of diamond.
    In: P.H. Nixon (Editor). Mantle Xenoliths. John Wiley & Sons Ltd,
    Chichester, UK: 477-500.

Harris, J.W., Hawthorne, J.B., Oosterveld, M.M. and Wehmeyer, E., 1975. A
    classification scheme for diamond and a comparative study of South
    African diamond characteristics. Physics and Chemistry of the Earth,
    9(C): 765-785.

Harris, J.W. and Vance, E.R., 1974. Studies of the reaction between diamond and
    heated kimberlite. Contributions to Mineralogy and Petrology, 47(4): 237-
    244.

Lang, A.R., 1964. Dislocations in Diamond and the Origin of Trigons.
    Proceedings of the Royal Society of London. Series A. Mathematical and
    Physical Sciences, 278(1373): 234-242.

Lang, A.R., 1979. Internal Structure. In: J.E. Field (Editor), The Properties of
    Diamond. Academic Press, London, pp. 425-469.

Moore, M. and Lang, A.R., 1974. On the origin of the rounded dodecahedral habit
    of natural diamond. Journal of Crystal Growth, 26(1): 133-139.

Omar, M., Pandya, N.S. and Tolansky, S., 1954. The Etching of Diamond. I.
    Octahedron Faces. Proceedings of the Royal Society of London. Series A,
    Mathematical and Physical Sciences, 225(1160): 33-40.

Orlov, Y.L., 1977. The mineralogy of the diamond. John Wiley and Sons Inc., New York, 275 pp.

Pandeya, D.C. and Tolansky, S., 1961. Micro-disk Patterns on Diamond Dodecahedra. Proceedings of the Physical Society, 78(1): 12.

Pandya, N.S. and Tolansky, S., 1954. The Etching of Diamond. II. Cleavage, Dodecahedron and Cube Faces. Proceedings of the Royal Society of London. Series A, Mathematical and Physical Sciences, 225(1160): 40-48.

Phaal, C., 1964. Plastic Deformation of Diamond. Philosophical Magazine, 10(107): 887-891.

Robinson, D.N., 1978. Characteristics of Natural Diamond and Their Interpretation. Minerals Science and Engineering, 10(2): 55-72.

Robinson., D.N., 1979. Surface Textures and other Features of Diamonds, University of Cape Town, unpublished PhD thesis, Cape Town,South Africa, 221 pp.

Robinson, D.N., Scott, J.A., van Niekerk, A. and Anderson, V.G., 1989. The sequence of events reflected in the diamonds of some southern African kimberlites. In: J. Ross (Editor), Proceedings of the Fourth International Kimberlite Conference, Perth, Australia. Blackwell Scientific, Carlton, Australia, Perth, Australia, pp. 990-1000.

Rondeau, B., Fritsch, E., Guiraud, M., Chalain, J.P. and Notari, F., 2004. Three historical 'asteriated' hydrogen-rich diamonds: Growth history and sector-dependent impurity incorporation. Diamond and Related Materials, 13(9): 1658-1673.

Stachel, T., 2007. Diamond. Mineralogical Association of Canada Short Course Series, 37: 1-22.

Stachel, T. and Harris, J.W., 1997. Diamond precipitation and mantle metasomatism - evidence from the trace element chemistry of silicate inclusions in diamonds from Akwatia, Ghana. Contributions to Mineralogy and Petrology, 129(2-3): 143-154.

Stachel, T. and Harris, J.W., 2009. Formation of diamond in the Earth's mantle. Journal of Physics Condensed Matter, 21(36).

Sunagawa, I., 1981. Characteristics of crystal growth in nature as seen from the morphology of mineral crystals. Bulletin de Mineralogie, 104: 81-87.

Sunagawa, I., 1984. Morphology of natural and synthetic diamond crystals. Materials Science of the Earth's Interior: 303-330.

Sunagawa, I., 2005. Crystals: Growth, Morphology, and Perfection. Cambridge University Press, United States of America, 295 pp.

Tappert, R. and Tappert, M.C., 2011. Diamonds in Nature: A Guide to Rough Diamonds. Springer Heildelberg Dordrecht, London New York.

Welbourn, C.M., Rooney, M.-L.T. and Evans, D.J.F., 1989. A study of diamonds of cube and cube-related shape from the Jwaneng mine. Journal of Crystal Growth, 94(1): 229-252.

Wilks, J. and Wilks, E., 1991. Properties and applications of diamond. Butterworth-Heinemann, Oxford, UK, 525 pp.

Zaitsev, A.M., 2001. Optical properties of diamond: a data handbook. Springer, Berlin, 502 pp.

Chapter 4: Diamond sources beneath the Hall Peninsula, Baffin Island, Nunavut:

A preliminary assessment based on Chidliak diamonds

4.0 Introduction:

The Chidliak diamond discoveries have led to the identification of a previously unidentified fragment (the Hall Peninsula) of what is likely an Archean craton that has significant diamond potential on the eastern edge of Southern Baffin Island. Here we present the first information about the paragenesis of Chidliak diamonds and their mantle residence history.

Starting in 2005, extensive work on the Hall Peninsula resulted in the discovery of the diamondiferous Chidliak kimberlite field. The Chidliak kimberlites tap mantle source regions of unknown paragenesis, age and history. Of the 44 kimberlites (out of 64) tested for diamonds, 18 of the kimberlites contained commercial-sized diamonds; seven kimberlites have proven to be distinctly diamondiferous with coarse diamond distributions with the presence of gem quality diamonds (Pell et al., 2012).

Approximately 740 diamonds ≤850 μm have been provided by Peregrine Diamonds Ltd. for this study, of which 210 are utilized for physical descriptions and geochemical analyses. The diamonds were separated from the kimberlite by SRC Geoanalytical Laboratories in Saskatoon, Saskatchewan, using crushing techniques and caustic fusion. The diamonds were then sieved (850-600 μm, 600-425 μm, 425-300 μm, 300-212 μm, 212-150 μm, 150-106 μm) and placed on sticky tape slides grouped according to sample number and sieve size.

Diamonds can form in the lithospheric mantle, the sublithospheric mantle, certain meteorites and impactites, and some ultra-high pressure rocks. Greater

than 99% of diamonds that are mined worldwide are derived from the lithospheric mantle (Stachel and Harris, 2008). Lithospheric diamonds form in the subcontinental lithospheric mantle (SCLM) and are associated with mantle peridotite, eclogite (Meyer 1987) and sometimes pyroxenite (websteritic suite of Gurney et al. 1984).

In the current study, diamond physical characteristics, carbon isotopes, nitrogen concentrations and aggregate states will be used to constrain the mantle source(s) and the temperature of residence in the mantle beneath the Hall Peninsula.

4.1 Geologic Background:

The diamonds utilized for this study come from two kimberlites, CH-7 (kimberlite sample P5500) and CH-6 (kimberlite sample P6807) from the Chidliak Project area (Figure 4.1), 120 km northeast of Iqaluit, located on the Hall Peninsula, southern Baffin Island (Pell, 2008; Pell and Farrow, 2012). Kimberlite bodies were initially identified after a suite of kimberlite indicator minerals (KIMs) had been discovered during the 2005 field season; subsequently, in 2008, a helicopter-borne magnetic/electromagnetic survey was flown, totaling 11 700 line-kilometres, leading to the discovery of numerous kimberlite bodies (Pell, 2009). After completion of the 2012 field season, the total number of kimberlites identified was 64 (61 at Chidliak; 3 at the neighbouring Qilaq project). Another 3 confirmed kimberlites have been identified during the 2013 field season at Chidliak, bringing the total count to 67 kimberlites (Peregrine Diamonds Ltd, 2013). Based on U-Pb perovskite age-determinations from 31 kimberlites, (29 at

Chidliak and two at the neighbouring Qilaq project), Heaman et al. (2012)

demonstrated that kimberlite emplacement took place from 156 to 138 Ma,

spanning approximately 18 m.y, with the majority of kimberlite emplacement

occurring in just 7 m.y. from 150 to 143 Ma.
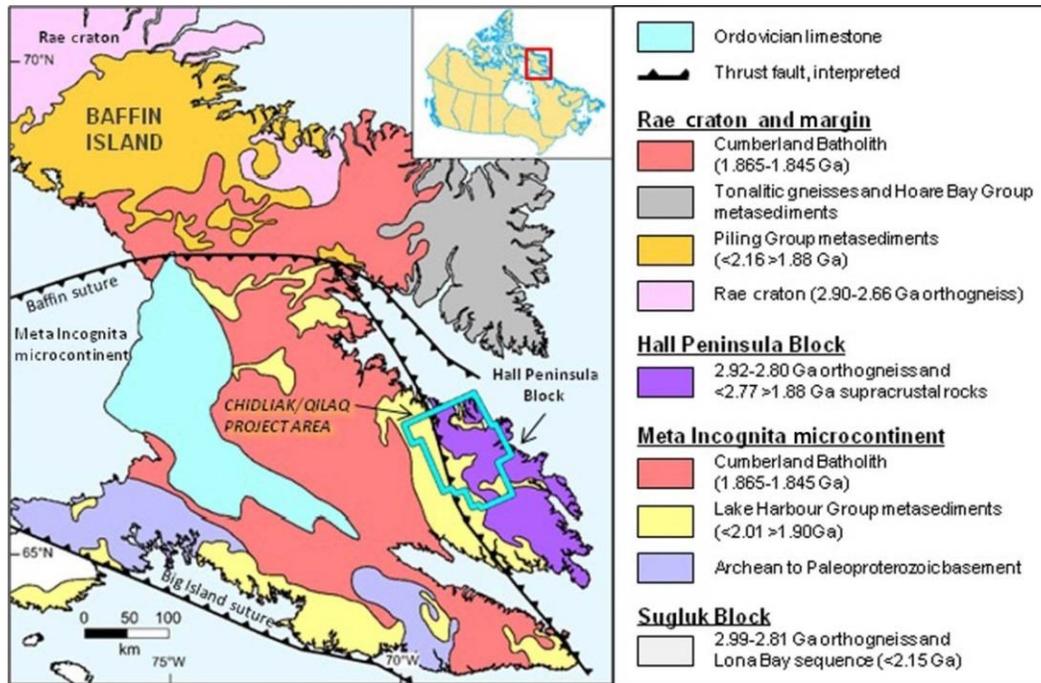
Figure 4.1. Simplified regional geological map of southern Baffin Island (after St-Onge et. al., 2006 and Whalen et. al., 2010), showing the location of the Hall Peninsula Block (purple) and the Chidliak (and neighbouring Qilaq) project area (light blue box) (Fig. 1, Pell et al., 2012).

The Hall Peninsula is separated from northern Baffin Island by the Baffin

suture; and contains three crustal segments, the eastern edge of the

Paleoproterozoic Cumberland Batholith, which is in contact with

Paleoproterozoic metasediments to the east and the Archean gneissic terrain

called the Hall Peninsula block (St. Onge, 2001; Whalen et al., 2010). The origin

of the Hall Peninsula block is currently unresolved, with three competing models

being outlined in Pell et al. (2013): (1.) that it may be a microcontinent that was

accreted during a two-phase, three-way collision between the Superior, Rae and

North Atlantic cratons at about 1.87-1.85 Ga and 1.82-1.79 Ga; the initial

collision pre-dates the emplacement of the Cumberland Batholith which connects

the Rae craton, North Atlantic craton and the Hall Peninsula block (Snyder, 2010;

Whalen et al., 2010). (2.) That it is a part of the Nain/North Atlantic craton (Scott,

1996; Scott, 1999, Theriault et al., 2001). (3.) That it is reworked fragment of

Archean gneisses correlative with those of the Trans Hudson Orogen in Canada

and the Nagssugtoqidian Orogen of west Greenland (St. Onge et al. 2007, Pell et

al., 2013).

4.2 Results:
4.2.1 Diamond Physical Descriptions:

Diamond may crystallize in two primary forms: octahedra, including

macles (spinel twin), and cuboids, including re-entrant cubes (e.g., Robinson

1978; Welbourn et al., 1989). Diamonds may also form aggregates (two or more

intergrown diamonds). Diamond may experience resorption during mantle

residence and kimberlite ascent; the extent of resorption can be identified through

characteristic morphologies and surface features: octahedral and cuboid diamonds

gradually convert to dodecahedral morphologies (Harris et al., 1975). Secondary

shapes include irregular, dodecahedral, and mixed octahedral-dodecahedral

morphologies, do and od (where the last letter represents the predominant

morphology; d-dodecahedral and o-octahedral). Classification of irregular

diamonds adheres to Harris et al. (1975): as long as ≥50% of the diamond shape

remains it will be classified based on the observed shape, if <50% of the diamond

remains, after either breakage or resorption leading to a diamond with no

definable shape, it will be classified as irregular. Octahedral and cuboid diamonds

may show growth-related primary surface features and secondary surface features.

Diamonds from both kimberlite CH-7 and CH-6 are predominantly irregular (41% and 42%, respectively), followed closely by octahedral fragments (30% and 12%, respectively). Dodecahedroids, cuboids, macles, aggregates and mixed octahedral-dodecahedral morphologies (do and od) are also present. Etch features on primary faces such as trigons and tetragons, and resorption features on rounded dodecahedral faces including plastic deformation lines, hillocks and terraces, are observed throughout this suite of diamonds. The majority of studied diamonds from kimberlite CH-7 are colorless (46%) followed by brown colors (27%), grey colors (10%) and yellow (7%). The diamonds from kimberlite CH-6 are also predominantly colorless (58%), followed by yellow colors (19%), brown colors (10%) and grey colors (9%).

4.2.2 FTIR:

Fourier-transform infrared spectroscopy (FTIR) is employed to determine nitrogen concentrations and aggregation states of Chidliak diamonds. This is used to constrain their residence history and time-averaged mantle residence temperature. Since carbon and nitrogen have a similar ionic radius, nitrogen substitutes and bonds very strongly with carbon in the crystal structure (Cartigny, 2005), which is why nitrogen is by far the most abundant substitutional impurity (and elemental impurity) in diamond, with values as high as 0.55% (Sellschop et al. 1980).

Diamond can be classified into different Types based on the presence and aggregation state of nitrogen impurities; on the basis of infrared (IR) absorption

spectroscopy, two main Types of natural diamond have been recognized, Type I and Type II (Harris, 1987). Type I has nitrogen present and Type II has no detectable nitrogen (Harris, 1987); Type I diamonds can be further subdivided based on whether the nitrogen is single substitutional (Type Ib), or if it has aggregated within the carbon lattice (Type Ia; Evans and Qi, 1982). Nitrogen enters the crystal lattice as single substitutional atoms (C centre), but during mantle residence quickly aggregates into pairs of nitrogen atoms (A centre) and then, more slowly, into groups of 4 atoms surrounding a vacancy (B centre) (Evans et al., 1995). The aggregation state of nitrogen in the diamond crystal lattice is related to the temperature and the time of residence in Earth's mantle, and the nitrogen concentration (Harris, 1987, Evans & Harris, 1989, Taylor et al. 1990). The process of nitrogen aggregation stops once diamond is emplaced in the (cold) Earth's crust (Allen and Evans, 1981; Evans and Qi, 1982).

Nitrogen in the B centre is expressed as $\%B \left(\left(\frac{B}{A+B} \right) \times 100 \right)$ where A and B refer to the amount of nitrogen in A centre and B centre (N_A and N_B, respectively). Diamonds with >90% of the total nitrogen in the A centre are classified as Type IaA. Intermediate diamonds with 10–90% of their total nitrogen content in the B centre are categorized as Type IaAB. Diamonds with >90% of the total nitrogen in the B centre are Type IaB.

Chidliak diamonds have nitrogen contents ranging from no detectable nitrogen ($\leq$ about 15 atomic ppm) to 3356 atomic ppm (at. ppm), with a median nitrogen concentration of 1103 at. ppm (Table 4.1). The diamonds from kimberlite CH-6 are 50.6% Type IaAB, 34.6% Type IaA, 4.9% Type II, 1.2%

Type IaB and 8.6% of diamonds have mixed aggregation states, meaning that one out of the two measured spots is Type IaA and one is Type IaAB. The diamonds from kimberlite CH-7 are predominantly Type IaA (56.5%), 30.6% Type IaAB, 9.4% Type II, 1.2% Type IaB, and only 2.4% have a mixed aggregation state between Type IaA and Type IaAB. The percentage of Type II Chidliak diamonds observed is less than that of inclusion bearing lithospheric diamonds worldwide (20%; Stachel, 2007), although it is broadly compatible with diamonds containing inclusions of eclogitic paragenesis (10%; Stachel and Harris, 2009).

Sample ID	Spot	Type	Total N (at. ppm)	%B	TN 1Ga (°C)	Platelet Peak Area (cm⁻²)	Platelet Peak Location (cm⁻¹)	3107 Peak Area (cm⁻²)	1405 Peak Area (cm⁻²)
CH6-2	1	IaA	1682	0.7	1014			23	
CH6-2	2	IaA	1627	0.0	1010			23	
CH6-6	1	IaAB	1425	31.9	1112	187	1373	29	
CH6-6	2	IaAB	1228	28.9	1112	180	1373	34	
CH6-8	1	IaAB	1359	63.6	1144	164	1377	26	
CH6-8	2	IaAB	1422	55.5	1135				
CH6-9	1	IaAB	1058	24.9	1111	118	1369		
CH6-9	2	IaAB	1346	29.8	1111	223	1369		
CH6-10	1	IaAB	875	26.2	1117	139	1371		
CH6-10	2	IaAB	951	29.7	1119	138	1369	3	
CH6-11	1	IaA	1371	2.5	1047			38	
CH6-11	2	IaA	1326	0.7	1022			40	
CH6-12	1	IaA	1446	5.8	1065			19	
CH6-12	2	IaA	1166	0.3	1016			9	
CH6-13	1	IaA	1842	0.4	1007			35	
CH6-13	2	IaA	2080	4.7	1053			35	
CH6-14	1	II	–	–	NA				
CH6-14	2	II	–	–	NA				
CH6-15	1	IaAB	335	15.6	1124				
CH6-15	2	IaA	332	2.8	1081				
CH6-17	1	IaAB	525	13.2	1109	50	1363		
CH6-17	2	IaAB	536	14.5	1111	48	1363		
CH6-18	1	IaA	435	4.4	1085	15	1367	1	
CH6-18	2	IaA	532	9.7	1100	18	1369	2	
CH6-20	1	IaA	1194	0.3	1016			22	
CH6-20	2	IaA	1119	0.0	1017			20	
CH6-21	1	IaA	2194	4.1	1048			71	19
CH6-21	2	IaA	2001	3.6	1047			70	18
CH6-22	1	IaA	2046	4.5	1052			60	12
CH6-22	2	IaA	2034	3.4	1045			57	12
CH6-23	1	IaA	2128	7.1	1061			53	9
CH6-23	2	IaA	2233	2.1	1033			49	9
CH6-24	1	IaA	276	0.2	1047	7	1363		
CH6-24	2	IaA	246	0.0	1049	6	1363		
CH6-25	1	IaA	1782	2.9	1045			32	
CH6-25	2	IaA	1659	6.4	1064			21	
CH6-26	1	IaAB	1154	23.6	1107	201	1369		
CH6-26	2	IaAB	758	15.9	1105	110	1368		
CH6-27	1	IaAB	2229	35.9	1106	276	1375	27	
CH6-27	2	IaAB	2089	33.9	1105	297	1375	54	
CH6-28	1	IaAB	2144	20.2	1088	100	1375	34	
CH6-28	2	IaAB	2162	27.7	1097	90	1375	33	
CH6-29	1	IaAB	1386	29.8	1110	78	1377	27	
CH6-29	2	IaAB	1684	29.8	1106	77	1379	14	
CH6-33	1	IaAB	3034	28.5	1091	53	1383	323	49
CH6-33	2	IaAB	2952	26.9	1089	63	1383	341	53
CH6-35	1	IaA	1968	2.7	1041			57	9
CH6-35	2	IaA	1863	0.8	1017			50	9
CH6-37	1	IaAB	627	21.9	1119	52	1365		
CH6-37	2	IaAB	524	11.3	1105	44	1365		
CH6-38	1	IaAB	1253	31.6	1115	245	1371	3	
CH6-38	2	IaAB	1609	41.3	1119	346	1371	5	
CH6-40	1	IaAB	385	26.1	1137	25	1363	30	
CH6-40	2	IaAB	342	21.0	1132	28	1363	31	7
CH6-43	1	IaAB	2885	12.9	1069			74	21
CH6-43	2	IaAB	2908	13.3	1070			84	26
CH6-44	1	II	–	–	NA				
CH6-44	2	II	–	–	NA				

Sample ID	Spot	Type	Total N (at. ppm)	%B	TN 1Ga (°C)	Platelet Peak Area (cm⁻²)	Platelet Peak Location (cm⁻¹)	3107 Peak Area (cm⁻²)	1405 Peak Area (cm⁻²)
CH6-45	1	IaA	1352	1.3	1034			65	11
CH6-45	2	IaA	1559	6.2	1065			74	11
CH6-46	1	IaA	185	0.0	1055			4	
CH6-46	2	IaA	299	9.5	1113			3	
CH6-47	1	II	–	–	NA				
CH6-47	2	II	–	–	NA				
CH6-48	1	IaAB	2311	17.3	1082	108	1377	8	
CH6-48	2	IaAB	2464	23.1	1089	130	1377	10	
CH6-49	1	IaAB	2955	13.3	1070			20	
CH6-49	2	IaAB	2748	13.7	1072			47	15
CH6-51	1	IaAB	1071	10.6	1087	17	1375	101	16
CH6-51	2	IaA	913	7.5	1082	20	1379	85	15
CH6-52	1	IaAB	1441	21.0	1098			59	16
CH6-52	2	IaAB	1570	16.2	1089			75	17
CH6-53	2	IaA	905	5.7	1075	102	1369		
CH6-53	3	IaAB	1103	19.4	1102	130	1369		
CH6-55	1	IaAB	887	17.9	1105	103	1367		
CH6-55	2	IaAB	1149	17.1	1098	40	1375	10	
CH6-56	1	IaAB	1120	23.9	1108	176	1369		
CH6-56	2	IaAB	1043	22.0	1107	174	1369		
CH6-58	1	IaAB	962	27.3	1116	54	1367	11	
CH6-58	2	IaAB	1115	12.1	1089	84	1367	12	
CH6-59	1	IaA	1647	6.8	1066			7	
CH6-59	2	IaA	967	5.7	1074			7	
CH6-60	2	IaA	423	1.9	1067	21	1365		
CH6-60	3	IaA	525	0.0	1033	48	1367		
CH6-61	2	IaAB	435	19.8	1125	55	1367	12	
CH6-61	3	IaA	534	0.0	1033	89	1367	11	
CH6-62	1	IaA	2090	7.0	1062			98	16
CH6-62	2	IaA	2307	5.8	1055			113	16
CH6-63	1	IaAB	931	29.1	1119	219	1367	12	
CH6-63	2	IaAB	918	28.9	1119	214	1367	7	
CH6-64	1	IaAB	1796	12.5	1079			84	23
CH6-64	2	IaA	1287	5.5	1067			45	
CH6-65	1	IaAB	348	13.9	1120	33	1363		
CH6-65	2	IaAB	348	11.0	1114	39	1363		
CH6-66	1	IaAB	532	37.2	1141	135	1365	11	
CH6-66	2	IaAB	716	43.5	1140	149	1365	28	
CH6-67	1	IaAB	1106	36.6	1123	61	1373		
CH6-72	1	IaA	1819	9.3	1071			36	
CH6-72	2	IaA	1540	0.0	1011			28	
CH6-73	1	IaA	1110	0.0	1017			68	
CH6-73	2	IaA	1110	0.0	1017			26	
CH6-74	1	IaAB	1482	14.6	1088			22	
CH6-74	2	IaAB	914	13.7	1097			20	
CH6-75	1	IaA	723	0.0	1026			6	
CH6-75	2	IaA	690	0.0	1027				
CH6-76	1	IaA	1424	0.0	1012			43	
CH6-76	2	IaA	1390	0.0	1013			32	
CH6-77	1	IaA	1610	8.8	1073	53	1379		
CH6-77	2	IaAB	1613	12.7	1082	56	1377		
CH6-78	1	IaAB	796	17.0	1106	87	1373	28	
CH6-78	2	IaAB	1229	23.7	1106	173	1373	47	
CH6-79	1	IaAB	1078	67.2	1155	325	1375	169	13
CH6-80	1	IaAB	1187	15.9	1095	159	1373	8	
CH6-80	2	IaAB	1177	16.3	1096	140	1373	7	
CH6-81	1	IaA	1397	3.8	1056			39	7
CH6-81	2	IaA	1455	2.4	1045			31	5

Sample ID	Spot	Type	Total N (at. ppm)	%B	TN 1Ga (°C)	Platelet Peak Area (cm⁻²)	Platelet Peak Location (cm⁻¹)	3107 Peak Area (cm⁻²)	1405 Peak Area (cm⁻²)
CH6-82	1	IaA	1133	7.7	1077			37	
CH6-82	2	IaA	1290	0.0	1014			30	
CH6-83	1	IaA	997	6.0	1074			8	
CH6-83	2	IaAB	1261	26.8	1109			9	
CH6-85	1	IaAB	1947	28.7	1101	283	1375	180	21
CH6-85	2	IaAB	1692	28.8	1104	258	1375	163	15
CH6-86	1	IaAB	850	38.3	1131	289	1371		
CH6-86	2	IaAB	713	39.8	1137	263	1371		
CH6-89	1	IaAB	913	22.4	1111	123	1369	16	
CH6-89	2	IaAB	829	18.3	1107	98	1369	20	
CH6-90	1	IaAB	502	25.3	1129	42	1367		
CH6-90	2	IaAB	516	14.4	1112	32	1367		
CH6-91	1	IaAB	873	15.9	1102	90	1369		
CH6-91	2	IaAB	855	17.3	1105	66	1369		
CH6-92	1	IaAB	907	26.7	1117	93	1369		
CH6-92	2	IaAB	1176	29.4	1114	154	1367		
CH6-93	1	IaA	1249	0.0	1015			17	
CH6-93	2	IaA	1239	0.7	1023			17	
CH6-94	1	IaA	1345	1.4	1035			29	
CH6-94	2	IaA	824	0.8	1034			19	
CH6-95	1	IaA	569	8.8	1096	44	1367		
CH6-95	2	IaA	587	5.9	1086	47	1367		
CH6-96	1	IaA	1917	1.4	1028			48	13
CH6-96	2	IaA	1805	6.5	1063			77	20
CH6-97	1	II	–	–	NA			6	
CH6-97	2	II	–	–	NA			6	
CH6-98	1	IaAB	1783	46.0	1121	520	1371	10	
CH6-98	2	IaAB	1626	43.7	1121	520	1371	11	
CH6-99	1	IaAB	1686	33.9	1110	299	1375	6	
CH6-99	2	IaAB	1565	38.3	1116	260	1375	6	
CH6-100	2	IaAB	2151	52.8	1123	628	1375		
CH6-101	1	IaAB	1532	11.2	1080			22	
CH6-101	2	IaA	1531	1.6	1035			24	
CH6-102	1	IaB	160	90.4	1246			11	
CH6-102	2	IaB	98	99.9	1408			11	
CH6-103	1	IaAB	1527	49.4	1128	456	1369	7	
CH6-103	2	IaAB	1236	46.1	1130	304	1369		
CH6-104	1	IaAB	583	20.0	1118	112	1367	14	
CH6-104	2	IaAB	596	19.8	1117	110	1367	14	
CH6-105	1	IaAB	357	43.0	1157	37	1363		
CH6-105	2	IaAB	379	38.8	1151	86	1363		
CH5-1	1	IaA	1090	2.0	1047			25	9
CH5-1	2	IaA	1096	0.4	1015			26	6
CH5-2	1	IaA	857	6.8	1081			16	
CH5-2	2	IaA	836	8.0	1085			18	
CH5-4	1	IaA	1126	4.3	1064			20	
CH5-4	2	IaA	1170	3.0	1054			16	
CH5-5	1	II	–	–	NA				
CH5-5	2	II	–	–	NA				
CH5-7	1	IaAB	1742	23.7	1098			55	11
CH5-7	2	IaAB	1425	16.5	1092			46	12
CH5-10	1	II	–	–	NA			1	
CH5-10	2	II	–	–	NA			1	
CH5-11	1	IaA	1143	1.3	1037	3	1363	33	7
CH5-11	2	IaA	1118	3.2	1057			32	7
CH5-15	1	IaAB	567	89.8	1209	276	1369	32	5
CH5-15	2	IaAB	505	88.2	1208	245	1369	28	6
CH5-16	1	IaA	1145	4.8	1066			22	

Sample ID	Spot	Type	Total N (at. ppm)	%B	TN 1Ga (°C)	Platelet Peak Area (cm⁻²)	Platelet Peak Location (cm⁻¹)	3107 Peak Area (cm⁻²)	1405 Peak Area (cm⁻²)
CH5-16	2	IaA	1112	8.1	1079			23	
CH5-17	1	IaA	1030	4.1	1064			17	
CH5-17	2	IaA	1227	6.1	1070			30	
CH5-18	1	IaAB	892	20.6	1109			101	15
CH5-18	2	IaAB	1025	19.8	1105			99	21
CH5-19	1	IaA	783	1.0	1040			17	
CH5-19	2	IaA	884	0.0	1022			11	
CH5-20	1	IaAB	1208	17.3	1097	102	1377	8	
CH5-20	2	IaAB	1415	24.0	1103	109	1375	6	
CH5-21	2	IaA	859	3.0	978			15	
CH5-21	3	IaA	894	3.4	1063			14	
CH5-22	1	IaAB	1692	22.9	1097	142	1375	18	
CH5-22	2	IaAB	1691	22.0	1096	155	1375	19	
CH5-23	1	II	–	–	NA				
CH5-23	2	II	–	–	NA				
CH5-24	1	IaAB	1078	16.4	1098	33	1375	123	20
CH5-24	2	IaAB	957	15.6	1099	26	1375	111	19
CH5-25	1	IaA	1130	0.2	1001			14	
CH5-25	2	IaA	1241	1.2	1034			17	
CH5-26	1	IaA	1040	4.0	1064	9	1379	121	21
CH5-26	2	IaA	1261	7.5	1074	7	1379	101	20
CH5-27	1	IaA	1180	6.7	1073	19	1377	70	13
CH5-27	2	IaA	1153	5.2	1067	21	1375	78	13
CH5-28	1	IaAB	1030	15.4	1097			155	25
CH5-28	2	IaAB	1232	16.2	1095			158	36
CH5-30	1	IaA	1436	0.3	1004			47	10
CH5-30	2	IaA	1554	1.8	1037			64	15
CH5-31	1	IaAB	905	23.7	1113	105	1365	3	
CH5-31	2	IaAB	804	22.5	1114	116	1365	4	
CH5-32	1	IaA	892	0.0	1022			9	
CH5-32	2	IaA	575	0.0	1031			20	
CH5-35	1	IaAB	414	14.7	1117			11	
CH5-35	2	IaAB	425	10.9	1109			9	
CH5-36	1	IaAB	1108	23.6	1108	74	1367	134	29
CH5-36	2	IaAB	899	12.6	1095	81	1367	128	33
CH5-38	1	IaA	1151	7.2	1076			56	11
CH5-38	2	IaA	1002	7.9	1081			48	9
CH5-39	1	IaA	1361	0.0	1013			27	
CH5-39	2	IaA	1081	0.0	1018			30	
CH5-40	1	IaA	1875	0.0	1007			37	
CH5-40	2	IaA	2609	6.8	1056			35	
CH5-41	1	IaA	1814	0.0	1007			22	
CH5-41	2	IaA	1592	0.0	1010			24	
CH5-42	1	IaA	1497	1.1	1028			94	19
CH5-42	2	IaA	1675	2.4	1042			96	18
CH5-43	1	IaA	1703	2.4	1042	8	1363	196	24
CH5-43	2	IaA	1550	0.0	1011	9	1363	226	37
CH5-44	1	IaA	2220	1.3	1022			50	13
CH5-44	2	IaA	1222	1.3	1035			111	31
CH5-45	1	IaA	116	0.0	1066				
CH5-45	2	IaA	110	0.0	1067				
CH5-46	1	IaA	753	1.3	1045	32	1367		
CH5-46	2	IaA	793	7.7	1086	33	1367		
CH5-47	1	IaAB	1025	14.5	1096	142	1367	2	
CH5-47	2	IaAB	1015	14.2	1096	147	1367	2	
CH5-48	1	IaA	1583	0.0	1010			41	
CH5-48	2	IaA	1502	0.0	1011			36	
CH5-49	1	II	–	–	NA			4	

Sample ID	Spot	Type	Total N (at. ppm)	%B	TN 1Ga (°C)	Platelet Peak Area (cm⁻²)	Platelet Peak Location (cm⁻¹)	3107 Peak Area (cm⁻²)	1405 Peak Area (cm⁻²)
CH5-50	1	II	–	–	NA				
CH5-51	1	IaA	940	0.3	1007			13	
CH5-51	2	IaA	973	0.0	1020			12	
CH5-52	1	IaAB	1315	12.3	1086			27	9
CH5-52	2	IaAB	889	11.1	1092			24	5
CH5-54	1	II	–	–	NA				
CH5-54	2	II	–	–	NA				
CH5-55	1	IaA	2457	1.2	1018			145	40
CH5-55	2	IaA	2545	3.6	1042			152	43
CH5-57	1	IaA	2577	0.7	1006			17	
CH5-57	2	IaA	2570	5.4	1051			47	8
CH5-59	1	IaA	1645	0.0	1009			21	
CH5-59	2	IaA	1805	1.0	1022			30	
CH5-60	1	IaA	919	0.0	1021			20	
CH5-60	2	IaA	1036	4.9	1069			33	
CH5-61	1	IaA	494	1.4	1034	48	1365		
CH5-61	2	IaA	521	6.0	1089	49	1369		
CH5-62	1	IaA	774	4.8	1075			8	
CH5-62	2	IaA	898	7.5	1082			8	
CH5-63	1	IaAB	1784	38.1	1113	379	1375	8	
CH5-63	2	IaAB	1606	37.5	1115	319	1373	11	
CH5-64	1	IaA	1034	6.9	1077			85	15
CH5-64	2	IaA	984	1.0	1035			83	14
CH5-66	1	IaA	268	0.0	1047			8	
CH5-68	1	IaAB	417	12.0	1112			4	
CH5-69	1	IaA	239	0.0	1050				
CH5-70	1	IaA	119	7.8	1130				
CH5-72	1	IaA	625	1.2	1049			3	
CH5-72	2	IaAB	542	11.9	1105			12	
CH5-73	1	IaAB	1716	18.7	1091	117	1379		
CH5-73	2	IaAB	2746	51.1	1115	298	1373	14	
CH5-75	1	IaA	345	0.0	1042			7	
CH5-75	2	IaA	267	5.4	1102			7	
CH5-76	1	IaAB	259	36.2	1158				
CH5-76	2	IaA	197	8.2	1119				
CH5-77	1	IaAB	2880	63.4	1126	306	1379	569	95
CH5-77	2	IaAB	2094	56.6	1127	304	1379	505	101
CH5-78	1	IaAB	279	28.1	1147			14	
CH5-79	1	II	–	–	NA				
CH5-79	2	II	–	–	NA				
CH5-80	1	IaA	1024	3.1	1058			25	5
CH5-80	2	IaA	903	0.0	1022			22	7
CH5-81	1	IaA	893	5.0	1073			21	
CH5-81	2	IaA	944	7.2	1080			20	
CH5-82	1	IaA	1770	0.0	1008			29	6
CH5-82	2	IaA	1959	0.0	1006			33	7
CH5-83	1	IaA	2791	6.6	1054			80	17
CH5-83	2	IaA	2434	0.0	1002			53	11
CH5-84	1	IaA	1045	0.0	1019			29	7
CH5-84	2	IaA	1024	0.0	1019			30	7
CH5-85	1	IaAB	1370	28.1	1109	223	1373		
CH5-85	2	IaAB	1428	27.1	1106	187	1373		
CH5-86	1	IaAB	1873	25.2	1098			45	
CH5-86	2	IaAB	1966	19.9	1090			47	
CH5-87	1	IaA	2379	7.1	1059			49	
CH5-87	2	IaA	1991	2.7	1041			45	
CH5-89	1	IaAB	1365	13.4	1087			68	
CH5-89	2	IaAB	1173	32.8	1117			58	

Sample ID	Spot	Type	Total N (at. ppm)	%B	TN 1Ga (°C)	Platelet Peak Area (cm⁻²)	Platelet Peak Location (cm⁻¹)	3107 Peak Area (cm⁻²)	1405 Peak Area (cm⁻²)
CH5-90	1	IaA	1213	6.3	1071	28	1379	65	11
CH5-90	2	IaA	1027	4.8	1068	27	1377	63	14
CH5-91	1	IaA	954	5.2	1072	26	1377	20	4
CH5-91	2	IaA	1016	5.7	1072	34	1377	33	8
CH5-92	2	IaA	1218	8.8	1079	35	1377	60	10
CH5-92	3	IaA	1112	3.7	1061	28	1377	58	10
CH5-93	1	IaAB	1128	18.3	1100			48	
CH5-93	2	IaAB	1191	10.1	1083			54	
CH5-94	1	IaAB	1158	11.0	1086			38	8
CH5-94	2	IaAB	1071	13.5	1093			38	10
CH5-95	1	IaAB	745	10.2	1094	38	1369	19	
CH5-95	2	IaAB	679	11.6	1099	38	1375	24	
CH5-96	1	IaA	862	0.0	1023			24	
CH5-96	2	IaA	859	0.0	1023			23	
CH5-97	1	IaA	819	9.2	1089			9	
CH5-97	2	IaA	1014	1.4	1041			8	
CH5-98	1	IaAB	173	19.8	1147	6	1371		
CH5-99	1	IaAB	1125	12.6	1090	136	1373		
CH5-99	2	IaAB	1165	21.4	1104	117	1373		
CH5-100	1	IaB	567	100.0	1350	131	1365	40	12
CH5-100	2	IaB	624	99.7	1313	262	1367	47	11
CH5-101	1	II	–	–	NA				
CH5-101	2	II	–	–	NA			4	
CH5-102	1	IaAB	768	39.7	1135	25	1377	314	60
CH5-102	2	IaAB	960	42.0	1132	39	1377	413	78
CH5-103	1	IaA	1083	6.8	1075				
CH5-103	2	IaA	1106	3.0	1056				
CH5-105	1	IaA	185	0.7	1063	15	1362		
CH5-105	2	IaA	157	1.8	1088	28	1362		

Table 4.1. Compilation of Chidliak FTIR data, showing diamond Type, total nitrogen content, percentage of nitrogen in the B centre (%B) and mantle residence temperatures. Additional observations include the platelet peak area, the location of the platelet peak, and the area under hydrogen peaks at 3107 cm⁻¹ and 1405 cm⁻¹.

4.2.2.1 Platelet Peak:

Platelets are nm to µm sized planar defects in the diamond lattice, and cause a strong absorption peak, usually between 1360 to 1375 cm⁻¹ (Sobolev et al., 1968). The peaks shift along this range is due to variation in the size of platelets; larger platelets are found at lower wave numbers while smaller platelets are found at the higher wave numbers (Mendelssohn and Milledge, 1995). For a long time the composition of platelets was controversial and it was believed that platelets were composed of nitrogen (Evans and Phaal, 1962). Subsequently, it

was realized that nitrogen associated with platelets relates to rare nitrogen interstitials (Woods, 1986). Now it is widely accepted that platelets are formed by interstitial carbon atoms (eg., Woods, 1986; Howell et al., 2012). A model of formation by Woods (1986) suggests that with the conversion from nitrogen A to B centres, vacancies are created and the released carbon interstitials migrate to form platelets; the peak at ~1370 cm^{-1} is attributed to the stretching vibration of C-C bonds within platelets.

Accordingly, Woods (1986) showed a linear correlation between the integrated strength of the platelet peak, I(B'), and the strength of the B centre absorption at 1282 cm^{-1}, μ_B. Diamonds following this relationship are considered to be "regular", and diamonds falling below the linear trend (i.e., showing weaker platelet related absorption than predicted from their nitrogen content in B centres) are termed "irregular" (Figure 4.2). The regular diamonds are assumed to have a smooth progression of nitrogen aggregation; irregular diamonds are caused by platelet degradation, which may occur during thermal events (Evans et al., 1995) or during strain (Woods, 1986) (Figure 4.3).

Platelet formation is more pronounced in octahedral than in cuboid growth sectors (Lang, 1974). Howell et al. (2012b), observed that for mixed growth habit diamonds, with coevally precipitated octahedral and cuboid growth sectors, the former follow the regular relationship between B' and N_B of Woods (1986), whereas the latter appear irregular. Considering that these growth sectors experienced the same thermal and strain events, this observation is likely due to significantly slower platelet development in cuboid diamonds (Howell et al.,

2012b). Howell et al. (2012b) related the slow platelet formation in cuboid growth sectors to abundant disk crack-like defects (Walmsley et al., 1987). This implies that diamonds with cuboid growth sectors must not be included in an evaluation of a regular or irregular relationship between platelets and nitrogen B centres.

Howell et al. (2012b) found that cuboid growth sectors were also strongly enriched in hydrogen (using the absorption strength at 3107 cm^{-1} as a measure of hydrogen content) relative to coeval octahedral growth sectors. From CL imaging (see below) it is apparent that some Chidliak diamonds are of mixed habit growth. Since only a subset of the diamonds were imaged by CL we use the absorption strength at 3107 cm^{-1} to filter out diamonds showing the high hydrogen contents typically associated with cuboid growth (e.g., Fritsch et al., 2007). Hydrogen-rich diamonds are defined as having an absorbance at the main H-peak (3107 cm^{-1}) greater than that of the intrinsic diamond absorbance band at 2450 cm^{-1} (Fritsch et al., 2007). All hydrogen-rich diamonds were removed from platelet degradation calculations.

For diamonds from kimberlite CH-7 a total of 25% of diamonds with suitable spectra for quantitative analysis exhibit a platelet peak. The single Type IaB diamond observed also has a platelet peak. Platelet peaks are observed for 55% of diamonds from kimberlite CH-6. The only Type IaB diamond from this sample does not have a platelet peak, which is likely due to platelet degradation. As predicted by Woods (1986), platelets are rare in Chidliak diamonds with a pure A component (0%B) with only 4 diamonds exhibiting a small platelet peak with the exception of one spot on diamond CH6-61 with a prominent platelet peak

(89 cm^{-2}) and one spot on diamond CH6-60 with a platelet peak intensity of 48 cm^{-2}.
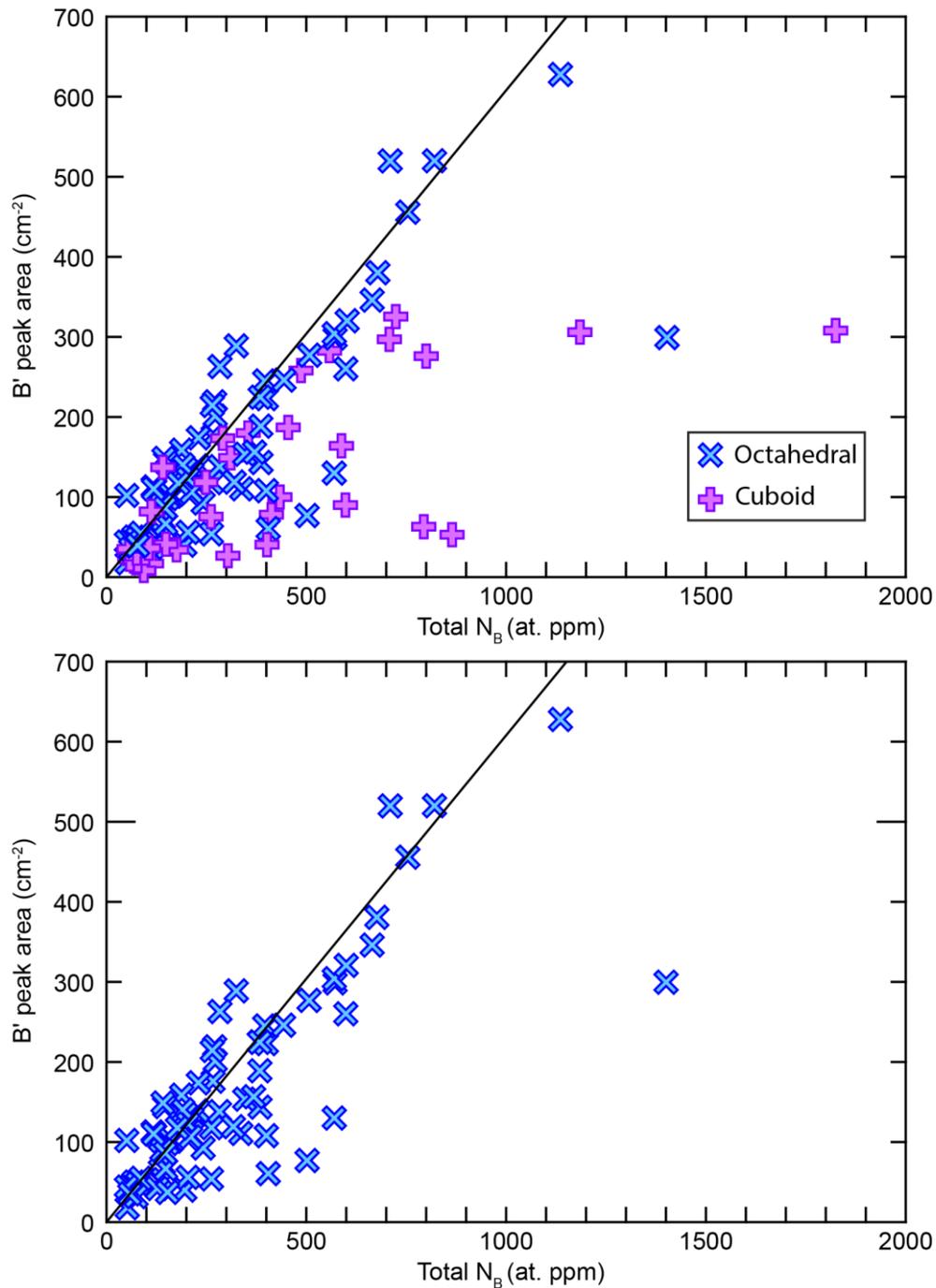
Figure 4.2. The relationship between platelet peak intensity and nitrogen in B centres (N_B) for diamonds with high quality spectra. The solid line represents the linear relationship (slope of 0.61) from Woods (1986) between peak intensity and N_B for regular diamonds. A) Including diamonds with cuboid growth sectors

identified in CL images and hydrogen rich diamonds: most of the cuboid diamonds plot below the regular line. B) Diamonds with octahedral growth only. A few "irregular diamonds" plot below the regular trend. Where possible two spots per diamond are shown.
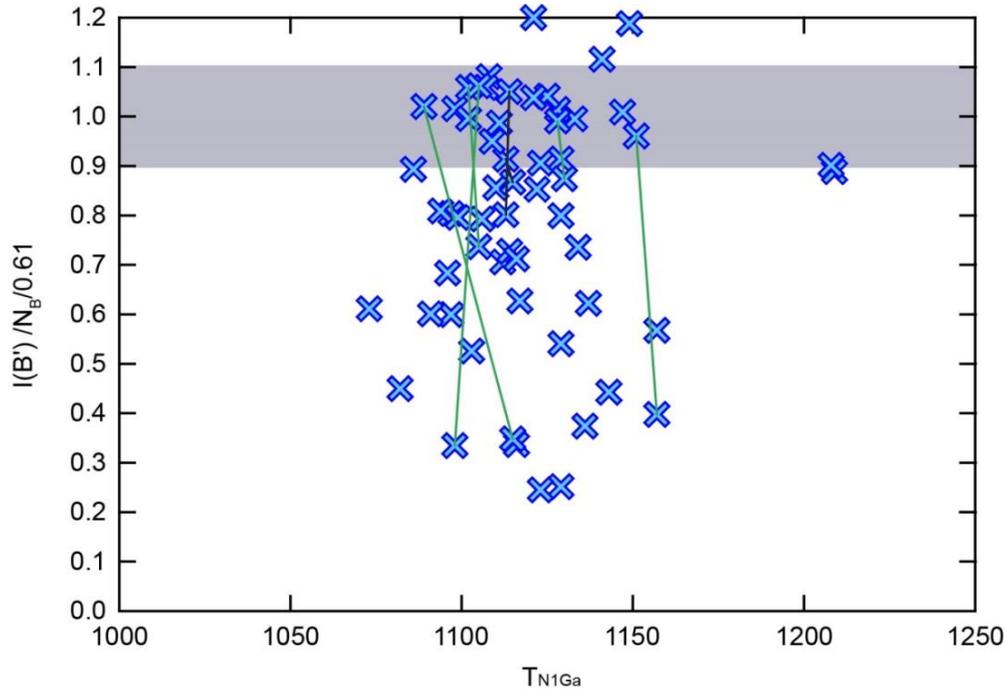
Figure 4.3. Degree of platelet degradation versus mantle residence temperature. The grey band represents regular diamonds, the area below the grey band represents increasing levels of platelet degradation. Only diamonds with octahedral growth are shown. There is no relationship between the degree of platelet degradation and residence temperature, suggesting that platelet degradation principally results from strain (Woods, 1986). Where possible two spots per diamond are shown, 7 diamonds with tie lines (green tie lines for diamonds from kimberlite CH-6 and black tie lines for diamonds from kimberlite CH-5) where one spot indicates platelet degradation and one spot does not.

4.2.2.2 Hydrogen Peak:

Hydrogen impurity concentrations in diamond can reach as high as 1 atomic % (Goss et al., 2003 and references therein); there are numerous peaks in the absorption spectrum from 4000 to 1500 cm^{-1} that at are attributed to hydrogen; the main peak is at 3107 cm^{-1}, with secondary peaks at 3237 cm^{-1}, 2786 cm^{-1}, and 1405 cm^{-1} being only visible when there is a peak at 3107 cm^{-1} (Woods and

71

Collins, 1983). The peaks at 3107 cm^{-1} and 1405 cm^{-1} are likely caused by bond vibrations between carbon-hydrogen (Chrenko et al., 1967) specifically, in the vinylidene group, C=CH$_2$ (Woods and Collins, 1983).

Hydrogen peak intensities (measured as peak area) show a total range from 0 to 569 cm^{-2} but the vast majority (98%) of diamonds fall within the range of 0 to 196 cm^{-2}. For diamonds from kimberlite CH-7, 81% of the spectra have a hydrogen peak at 3107 cm^{-1}, (including the single Type IaB diamond) as well as 50% of the Type II diamond spectra. For diamonds from kimberlite CH-6, 70% of diamonds have a hydrogen peak; again, the hydrogen peak is present in the only Type IaB diamond from this sample and for 20% of the Type II diamond spectra.

4.2.2.3 Other Spectral Peaks:

Absorbance peaks are also commonly found at ~2960 cm^{-1}, 1734 cm^{-1}, ~1009 cm^{-1}, 845 cm^{-1} and less commonly at 2930 cm^{-1}, 2876 cm^{-1}, ~2850 cm^{-1}, 2830 cm^{-1}, 2784 cm^{-1}, 1739 cm^{-1}, 1737 cm^{-1}, 1550 cm^{-1}, 1525 cm^{-1}, 1465 cm^{-1}, 1095 cm^{-1}.

Titus et al. (2005) took an in depth look into the "CH stretching region" between 2700 cm^{-1} to 3100 cm^{-1} for diamond films and identified seven peaks that may occur in this region, including five peaks that are also identified for Chidliak diamonds at ~2960 cm^{-1}, 2930 cm^{-1}, 2876 cm^{-1}, ~2850 cm^{-1}, 2830 cm^{-1}. Peaks within this area indicate strongly bonded hydrogen; absorbance at ~2960 cm^{-1} and 2876 cm^{-1} is attributed to asymmetric stretching of sp^3 bonded CH$_3^-$ groups, peaks at 2930 cm^{-1}, and ~2850 cm^{-1} are due to symmetric stretching of sp^3 bonded CH$_2^{2-}$ groups (Janssen et al., 1991; Dischler et al., 1993; Titus et al., 2005), and the peak

at 2830 cm^{-1} peak may be caused by C-H stretching vibrations in O–CH$_3$ groups (Titus et al., 2005). The peak at 1465 cm^{-1} is attributed to H-C-H bending mode of the CH$_2{}^{2-}$ group (Janssen et al., 1991). The peak at 1739 cm^{-1} is possibly related to the C=O stretching of carboxyl groups (Janssen et al., 1991). Ferrer and Nogués-Carulla (1996) identified a peak at 1547 cm^{-1}, which occurs in some Type IaAB diamonds containing hydrogen impurities. Chidliak diamonds with peaks at 1734 cm^{-1} and 1525 cm^{-1} are predominantly associated with diamonds containing hydrogen peaks at 3107 cm^{-1}.

Weiss et al. (2010) identified a secondary apatite band at 1095 cm^{-1}, which overlaps with quartz (~1100 cm^{-1}); the main phlogopite band is at ~1000 cm^{-1} (Weiss et al., 2009). The absorption band at 1095 cm^{-1} in some Chidliak diamonds, therefore, is likely related to submicroscopic mineral inclusions but cannot be unequivocally assigned to apatite.

4.2.3 Inclusions in Diamond:

Typically, recoverable inclusions in diamond are on the order of 100-200 μm (Stachel and Harris, 2009); in the current study most diamonds barely exceed this size range and hence cannot be expected to contain recoverable inclusions. In general, only graphite inclusions and a single rusty orange inclusion (likely altered olivine) were observed.

4.2.4 SIMS Analyses:

Spatially highly resolved (15 μm spot size) analyses of nitrogen concentrations and carbon isotope compositions via secondary ion mass

spectrometry (SIMS) were conducted to fingerprint mantle source regions and fluid sources of Chidliak diamonds.

4.2.4.1 Nitrogen:

Ninety-four diamonds were analyzed for nitrogen concentrations using SIMS (Table 4.2). The range in nitrogen concentration is from ~1 at. ppm to 3833 at. ppm with a median of 1130 at. ppm (Figure 4.4), which is comparable to the set of values measured using FTIR (Figure 4.5). Diamonds ≥425 µm and diamonds <425 µm have similar nitrogen characteristics measured via SIMS and FTIR.

The nitrogen isotopic composition ($\delta^{15}N$) was measured for 86 diamonds, 8 diamonds with low nitrogen concentrations (<40 at. ppm) were excluded. Spots were placed adjacent to the original spots for $\delta^{13}C$ and nitrogen contents, but within the same growth zones. Nitrogen has two stable isotopes, ^{14}N and ^{15}N and the ratio is expressed as $\delta^{15}N$ in per mil relative to air. Cumulatively, a range in $\delta^{15}N$ from -5.9 to +18.7‰ is observed with a principle mode about -3‰ and secondary modes at +3‰ and +6‰ (Figure 4.6). The $\delta^{15}N$ modes are, however, distinct for diamonds from the two kimberlites: diamonds from kimberlite CH-7 show a range from -5.7 to +18.7‰ with a mode at -3‰; diamonds from kimberlite CH-6 have a similar range from -5.9 to +15.6‰, but show a large shift in mode to +3‰.
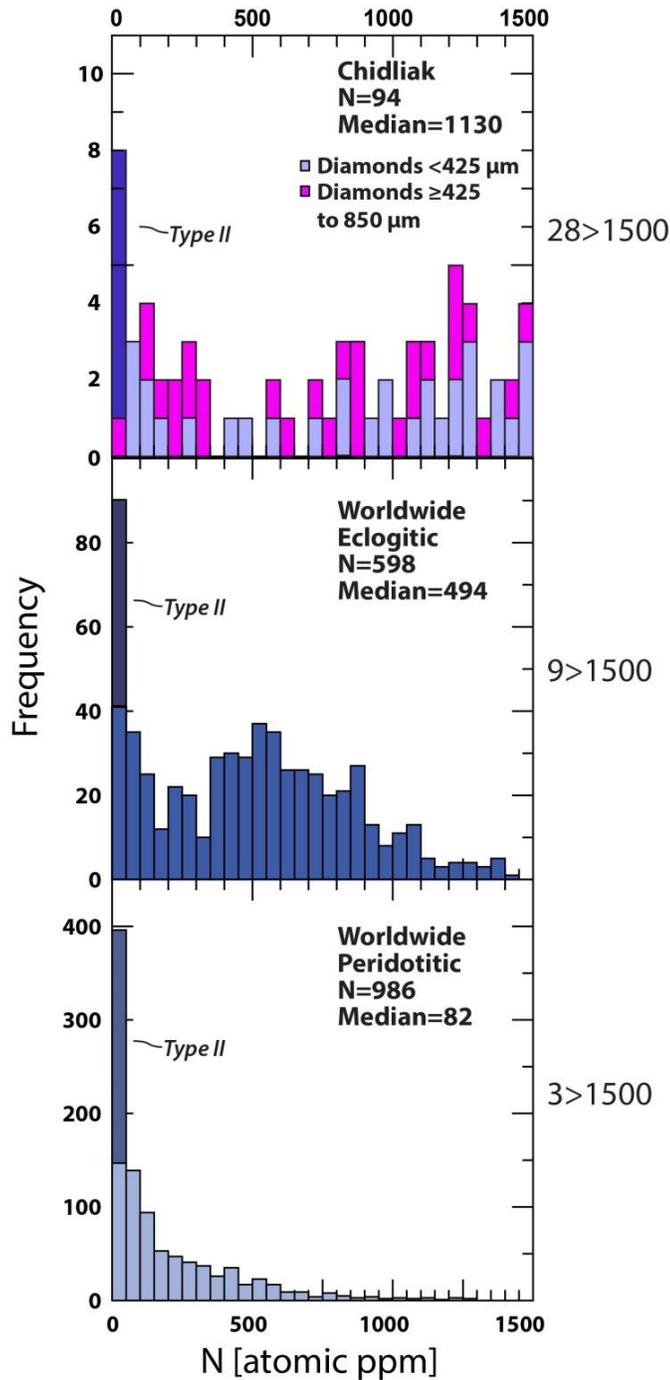
Figure 4.4. Nitrogen concentration of Chidliak diamonds measured using SIMS. The nitrogen concentration was averaged for each diamond. Chidliak diamonds are compared to eclogitic and peridotitic diamonds from worldwide sources (database of Stachel and Harris, 2008). Chidliak diamonds have high nitrogen concentrations (median 1130 at. ppm), 28 diamonds exceed 1500 at. ppm.
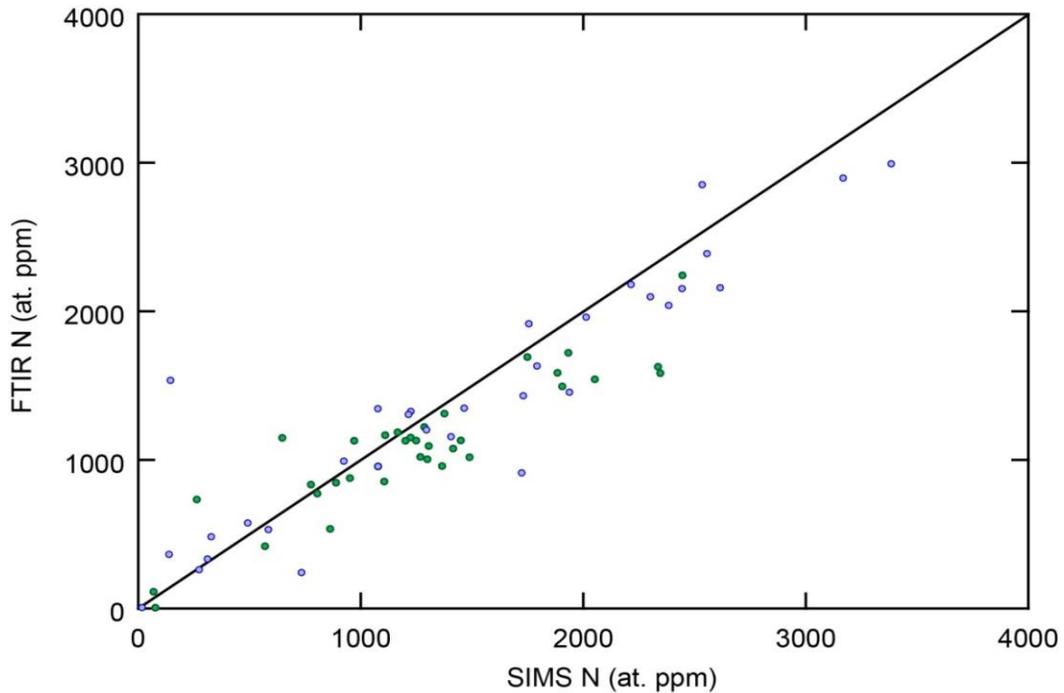
Figure 4.5. Comparison of average nitrogen values determined with FTIR and SIMS. A strong linear correlation is observed; the black line represents a 1:1 ratio. Green circles represent measurements of diamonds from kimberlite CH-6, whereas blue circles represent measurements of diamonds from kimberlite CH-7.
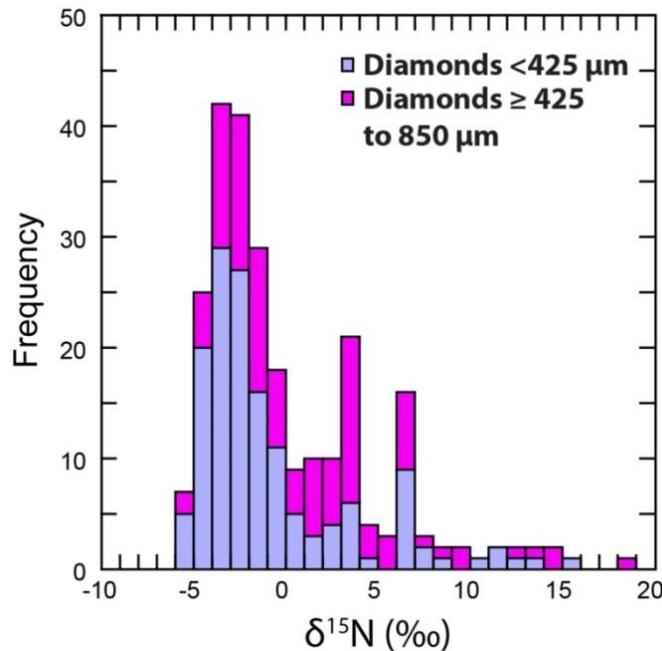
Figure 4.6. $\delta^{15}N$ values of Chidliak diamonds measured via SIMS; nitrogen isotopic compositions were not averaged (i.e., multiple measurements are reported for each diamond). A range in $\delta^{15}N$ of -5.9 to +18.7‰ is observed with a mode about -3‰ and secondary modes at +3‰ and +6‰.

Sample ID	δ¹³C (‰) (VPDB)	2σ error (‰)	N (at. ppm)	2σ error (ppm)	δ¹⁵N (AIR)	2σ error (‰)	Sample ID	δ¹³C (‰) (VPDB)	2σ error (‰)	N (at. ppm)	2σ error (ppm)	δ¹⁵N (AIR)	2σ error (‰)
CH5-1	-5.86	0.20	1245.2	125.5	-3.49	1.08	CH5-23	-22.37	0.21	0.9	0.1		
CH5-1	-5.91	0.20	1218.8	122.5	-3.47	0.94	CH5-23	-22.41	0.20	1.5	0.2		
CH5-1	-6.38	0.21	1454.6	146.3	-3.51	0.94	CH5-24	-3.66	0.20	1579.5	159.1	-2.86	0.75
CH5-2	-5.86	0.21	930.7	93.9	-3.90	1.09	CH5-24	-4.09	0.20	1547.4	156.5	-3.98	0.82
CH5-2	-5.22	0.21	905.7	92.2	-3.39	1.08	CH5-24	-3.34	0.21	1339.7	136.2	-2.66	0.83
CH5-2	-5.27	0.21	830.4	83.6	-2.20	1.22	CH5-25	-6.00	0.22	1336.5	134.7	-4.08	0.88
CH5-3	-3.18	0.21	187.8	19.2	-1.14	2.51	CH5-25	-6.15	0.21	1088.2	109.6	-5.06	0.96
CH5-3	-3.21	0.20	239.8	24.4	-3.39	1.92	CH5-25	-5.90	0.21	1073.5	108.3	-4.85	0.90
CH5-4	-5.50	0.20	741.5	74.8	-2.86	1.19	CH5-26	-4.64	0.21	1178.9	119.3	-4.17	0.84
CH5-4	-5.16	0.21	15.9	1.7	-1.90	0.96	CH5-26	-4.41	0.21	1247.1	125.7	-4.46	0.85
CH5-4	-5.73	0.21	1184.3	118.6			CH5-26	-4.53	0.20	1247.2	125.3	-3.15	0.91
CH5-5	-4.24	0.20	5.0	0.5			CH5-27	-4.17	0.21	1716.2	174.0	-4.11	0.78
CH5-5	-5.71	0.21	1.4	0.1			CH5-27	-4.31	0.21	1176.5	120.7	-4.03	1.08
CH5-5	-5.35	0.20	4.2	0.5			CH5-27	-3.91	0.20	437.8	44.3	-0.11	1.72
CH5-6	-7.07	0.21	1397.1	140.4	-2.87	0.71	CH5-28	-4.51	0.20	1883.6	190.5	-4.11	0.75
CH5-6	-6.04	0.21	878.8	90.1	-2.12	1.01	CH5-28	-4.27	0.21	1493.9	150.9	-4.57	0.83
CH5-6	-5.49	0.22	1065.8	106.8	-1.59	0.84	CH5-28	-3.93	0.22	973.0	98.8	-3.02	0.89
CH5-7	-6.16	0.21	2328.8	234.8	-3.45	0.57	CH5-30	-6.42	0.20	2228.4	223.6	-0.69	0.69
CH5-7	-6.02	0.21	2113.9	212.6	-3.07	0.60	CH5-30	-6.33	0.20	1448.0	146.1	-0.37	0.81
CH5-7	-5.51	0.20	2596.6	261.1	-2.38	0.56	CH5-30	-6.02	0.21	2042.5	205.9	-1.46	0.75
CH5-8	-5.29	0.21	1089.5	117.1	-0.85	0.83	CH5-31	-3.71	0.20	1401.2	141.2	-1.25	0.79
CH5-8	-5.24	0.21	973.6	98.6	-1.38	0.85	CH5-31	-4.17	0.21	931.3	93.9	-3.49	1.08
CH5-8	-5.36	0.21	1001.2	102.1	-0.76	0.84	CH5-31	-3.96	0.20	985.1	100.0	-2.11	0.97
CH5-9	-2.41	0.21	159.9	16.2	18.71	2.61	CH5-32	-5.36	0.21	18.7	2.2		
CH5-9	-2.45	0.22	312.4	31.9	14.50	1.77	CH5-32	-5.09	0.21	337.4	41.6		
CH5-9	-2.52	0.21	329.9	33.3	12.62	1.73	CH5-32	-5.18	0.22	433.6	45.6		
CH5-10	-2.12	0.20	3.3	0.3			CH5-33	-23.72	0.20	96.6	9.9	6.72	2.79
CH5-10	-2.08	0.21	2.4	0.2			CH5-33	-5.79	0.21	682.2	69.0	-1.85	1.15
CH5-11	-4.79	0.21	1158.9	117.3	-4.40	0.88	CH5-33	-5.96	0.21	784.1	79.1	-2.69	1.04
CH5-11	-4.82	0.21	1339.8	135.1	-4.07	0.83	CH5-33	-5.72	0.21	646.8	65.1	-2.89	1.10
CH5-12	-2.85	0.20	203.6	20.9	-2.44	2.03	CH5-33	-23.77	0.21	98.4	10.1	4.48	3.54
CH5-12	-3.36	0.20	11.9	1.3			CH5-33	-5.95	0.20	735.0	74.5	-2.78	1.11
CH5-13	-4.16	0.20	638.2	64.7	-1.23	1.20	CH5-33	-14.44	0.21	343.0	34.5	-2.29	1.16
CH5-13	-3.91	0.21	1018.4	102.4	-1.54	0.99	CH5-33	-23.76	0.21	97.1	10.0	6.83	2.60
CH5-13	-5.14	0.20	991.4	99.9	-3.15	0.90	CH5-34	-23.70	0.21	122.2	12.6	6.03	2.37
CH5-15	-12.77	0.20	17.4	1.8			CH5-34	-23.52	0.21	135.1	13.8	7.28	2.42
CH5-15	-7.16	0.20	1528.8	156.6	4.98	0.76	CH5-34	-23.87	0.20	111.1	11.5	6.66	2.54
CH5-15	-7.45	0.21	1041.1	105.7	6.03	0.86	CH5-35	-10.71	0.23	411.9	43.5	-3.12	1.23
CH5-16	-6.43	0.21	975.4	98.6	-4.57	1.13	CH5-35	-5.90	0.20	672.6	67.7	-2.55	1.19
CH5-16	-6.24	0.21	931.3	94.2	-4.49	1.23	CH5-35	-5.97	0.21	754.0	75.9	-3.99	1.13
CH5-16	-6.26	0.21	1005.6	101.4	-4.58	1.26	CH5-35	-22.34	0.22	118.8	12.2	-1.60	2.01
CH5-17	-6.25	0.20	1254.5	126.5	-4.03	0.89	CH5-35	-5.92	0.20	891.3	89.9	-4.21	1.03
CH5-17	-6.22	0.20	1190.9	119.6	-3.78	0.92	CH5-36	-5.90	0.21	1963.2	197.3	-5.45	0.79
CH5-17	-6.53	0.20	1157.2	116.4	-3.96	0.92	CH5-36	-5.51	0.21	792.5	80.8	-3.67	0.99
CH5-18	-4.23	0.22	1688.1	169.7	-0.46	0.70	CH5-36	-5.50	0.20	1142.6	115.0	-3.74	0.96
CH5-18	-6.70	0.20	1163.9	117.0	-2.33	0.86	CH5-37	-3.42	0.21	159.3	16.3	-0.83	2.49
CH5-18	-6.47	0.20	1244.9	125.5	-1.76	0.79	CH5-37	-3.47	0.21	147.0	15.2	0.49	2.61
CH5-19	-5.25	0.21	794.6	80.0	-1.93	0.98	CH5-37	-3.14	0.21	170.7	17.3	-2.14	2.32
CH5-19	-5.29	0.21	825.6	83.5	-2.49	0.95	CH5-38	-5.42	0.21	1214.7	122.9	-2.39	0.89
CH5-19	-4.91	0.21	707.8	72.9	-1.40	1.05	CH5-38	-5.96	0.20	1544.6	155.8	-3.71	0.89
CH5-20	-15.82	0.20	1086.9	114.6	11.43	2.73	CH5-38	-6.06	0.20	1487.7	149.8	-3.20	0.81
CH5-20	-15.72	0.21	1430.2	144.2	7.21	0.71	CH5-39	-6.32	0.20	1451.4	146.5	-4.64	0.85
CH5-20	-15.68	0.21	1611.7	162.4	6.47	0.72	CH5-39	-6.29	0.21	1364.7	137.9	-4.38	0.85
CH5-21	-5.81	0.21	890.4	89.9	-2.97	1.00	CH5-39	-6.11	0.20	1040.7	104.6	-3.26	0.97
CH5-21	-5.12	0.20	849.0	85.7	-2.28	0.85	CH5-40	-5.45	0.21	1725.4	173.2	-0.39	0.81
CH5-21	-5.32	0.21	1115.2	112.1	-1.57	0.80	CH5-40	-5.31	0.20	2039.4	204.9	-1.24	0.68
CH5-22	-15.72	0.20	1711.2	173.9	6.85	0.70	CH5-40	-6.48	0.20	3336.3	335.7	-2.92	0.60
CH5-22	-15.78	0.20	1787.8	180.2	6.99	0.68	CH5-40	-6.03	0.20	2683.8	271.6	-2.46	0.62
CH5-23	-22.49	0.20	0.2	0.1			CH5-42	-6.72	0.21	1835.9	184.0	-2.52	0.74

Sample ID	δ¹³C (‰) (VPDB)	2σ error (‰)	N (at. ppm)	2σ error (ppm)	δ¹⁵N (AIR)	2σ error (‰)	Sample ID	δ¹³C (‰) (VPDB)	2σ error (‰)	N (at. ppm)	2σ error (ppm)	δ¹⁵N (AIR)	2σ error (‰)
CH5-42	-6.52	0.20	2052.5	207.2	-1.95	0.72	CH6-10	-9.96	0.20	2166.9	219.0	3.56	0.73
CH5-42	-6.80	0.21	1765.9	177.8	-2.67	0.85	CH6-10	-9.89	0.21	1934.6	195.0	3.77	0.83
CH5-43	-5.15	0.20	3289.6	331.0	-2.13	0.60	CH6-10	-11.01	0.20	1068.3	107.7	6.21	1.02
CH5-43	-4.89	0.20	1906.8	192.0	-1.13	0.78	CH6-11	-6.61	0.21	1705.6	171.3	-2.89	0.68
CH5-43	-4.91	0.21	1813.8	182.7	-1.04	0.80	CH6-11	-6.59	0.21	1638.8	165.1	-2.15	0.68
CH5-44	-4.86	0.20	2602.2	261.6	-2.69	0.64	CH6-11	-6.26	0.20	1051.3	106.6	-3.16	0.70
CH5-44	-4.74	0.20	1548.0	155.9	-1.13	0.81	CH6-12	-7.01	0.20	1159.0	117.2	-3.51	0.94
CH5-44	-4.81	0.20	1649.3	165.7	-0.73	0.93	CH6-12	-7.02	0.21	1185.6	119.2	-3.99	1.08
CH5-45	-8.83	0.20	7.7	0.8			CH6-12	-6.80	0.20	1300.2	131.2	-2.96	1.05
CH5-45	-8.76	0.20	28.3	3.2			CH6-13	-3.60	0.20	2820.7	285.6	1.59	0.57
CH5-45	-9.27	0.20	171.2	17.5			CH6-13	-4.52	0.20	1294.1	129.7	2.73	0.67
CH5-46	-4.08	0.21	805.7	81.5			CH6-13	-7.01	0.20	1924.0	193.9	-3.12	0.63
CH5-46	-4.14	0.20	803.0	81.1			CH6-14	-5.57	0.21	15.6	1.8		
CH5-46	-4.08	0.21	806.2	81.5			CH6-14	-6.22	0.21	18.2	2.0		
CH5-47	-4.72	0.21	1437.1	145.0			CH6-15	-26.54	0.21	318.4	32.0	-0.74	1.90
CH5-47	-4.58	0.20	1468.4	149.0			CH6-15	-26.70	0.21	267.9	27.0	-2.50	1.53
CH5-47	-4.01	0.20	900.9	91.3			CH6-15	-26.66	0.21	347.7	35.1	-2.37	1.61
CH5-48	-5.64	0.21	2007.2	202.0	-4.56	0.73	CH6-16	-28.60	0.21	6.1	0.6		
CH5-48	-5.48	0.20	2120.5	214.0	-3.97	0.75	CH6-16	-28.60	0.20	5.6	0.6		
CH5-48	-5.16	0.21	2030.5	204.6	-3.66	0.65	CH6-16	-28.60	0.21	5.8	0.6		
CH5-49	-1.27	0.21	213.9	22.2	-5.26	1.90	CH6-17	-4.33	0.20	558.3	56.5	1.41	1.29
CH5-49	-2.88	0.20	1.7	0.2			CH6-17	-4.34	0.21	573.1	58.1	3.65	1.27
CH5-49	-4.23	0.21	17.0	1.8			CH6-17	-4.65	0.20	624.2	63.1	3.96	1.32
CH5-50	-3.27	0.21	0.7	0.1			CH6-18	-4.02	0.20	149.7	15.2	8.74	2.43
CH5-50	-4.55	0.21	20.2	2.1			CH6-18	-4.00	0.21	333.0	33.6	2.90	1.68
CH5-50	-4.63	0.20	4.5	0.5			CH6-18	-4.57	0.21	501.6	50.6	0.17	1.39
CH5-51	-5.23	0.21	975.0	98.2	-2.52	0.96	CH6-19	-3.22	0.21	176.4	17.9	5.54	2.17
CH5-51	-5.12	0.21	1147.4	115.6	-2.64	0.90	CH6-19	-3.34	0.20	138.5	14.6	7.21	2.00
CH5-51	-5.86	0.20	1197.6	121.2	-5.66	0.88	CH6-19	-3.27	0.20	279.8	28.2	3.37	1.74
CH5-51	-6.21	0.21	991.8	99.8	-4.60	1.08	CH6-20	-6.77	0.20	1499.6	151.3	-5.89	0.88
CH6-1	-3.37	0.20	775.4	78.4	2.09	1.20	CH6-20	-6.68	0.20	1447.4	145.2	-5.04	0.97
CH6-1	-3.34	0.21	655.6	66.1	2.95	1.18	CH6-20	-6.59	0.21	1270.2	128.8	-4.80	0.95
CH6-1	-3.49	0.21	744.8	75.2	1.53	1.19	CH6-21	-6.99	0.21	2299.5	231.3	-3.40	0.65
CH6-2	-6.83	0.21	1760.0	177.7	-3.25	0.74	CH6-21	-6.99	0.21	2303.9	232.5	-3.90	0.63
CH6-2	-7.00	0.21	1850.5	187.0	-2.97	0.80	CH6-22	-5.32	0.21	2048.7	206.8	-1.46	0.67
CH6-2	-6.91	0.21	1767.0	179.1	-2.45	0.79	CH6-22	-6.35	0.21	2958.1	297.8	-1.15	0.59
CH6-3	-6.18	0.21	1603.8	162.4	3.46	0.83	CH6-22	-5.74	0.20	2147.1	215.7	-1.05	0.65
CH6-3	-6.78	0.21	3206.1	323.9	1.39	0.58	CH6-23	-6.61	0.21	2239.2	224.7		
CH6-3	-6.49	0.20	2513.0	253.3	1.69	0.64	CH6-23	-6.49	0.21	2118.6	212.2	-2.19	0.66
CH6-3	-6.23	0.21	3357.6	339.0	1.06	0.58	CH6-23	-7.22	0.20	2287.4	229.2	-3.21	0.67
CH6-4	-6.03	0.21	2604.0	261.4	-0.99	0.75	CH6-24	-5.16	0.20	279.0	28.2	0.30	1.71
CH6-4	-6.27	0.20	1706.0	173.9	-1.77	0.84	CH6-24	-5.06	0.20	269.5	27.2	0.50	1.83
CH6-4	-7.44	0.21	1517.3	152.8	-4.87	0.92	CH6-24	-5.19	0.21	274.5	27.8	-0.42	1.60
CH6-5	-3.24	0.21	3.9	0.4			CH6-26	-8.13	0.20	1365.9	137.9	6.56	0.82
CH6-5	-3.06	0.21	342.6	34.5	2.21	1.82	CH6-26	-8.10	0.21	1356.6	136.9	6.89	0.83
CH6-5	-3.10	0.20	318.9	32.3	1.74	2.21	CH6-26	-8.03	0.21	512.2	51.9	13.09	1.34
CH6-6	-14.42	0.20	2868.8	289.4	-1.57	0.71	CH6-27	-8.87	0.21	2934.9	295.4	3.38	0.55
CH6-6	-14.15	0.21	491.9	50.1	9.14	1.40	CH6-27	-7.68	0.21	2342.4	236.5	3.41	0.65
CH6-6	-14.25	0.21	315.1	32.5	14.83	1.87	CH6-27	-7.93	0.20	2569.5	259.2	3.14	0.56
CH6-7	-24.40	0.21	61.4	6.5			CH6-28	-11.03	0.20	2552.3	257.2	-3.12	0.59
CH6-7	-23.73	0.20	7.1	0.8			CH6-28	-9.34	0.21	2448.8	246.2	-3.48	0.56
CH6-7	-5.05	0.20	1615.8	162.8	-1.06	0.79	CH6-28	-11.38	0.20	2333.0	237.7	-2.84	0.60
CH6-7	-3.62	0.21	1572.9	163.8	-1.82	0.80	CH6-29	-12.65	0.21	137.8	14.0	6.86	2.61
CH6-8	-15.66	0.20	2773.0	280.3	4.50	0.56	CH6-29	-12.57	0.21	172.1	17.5	4.30	2.21
CH6-8	-15.82	0.21	37.3	4.0			CH6-29	-12.89	0.21	125.1	12.8	3.73	2.30
CH6-8	-15.58	0.21	421.6	43.0	3.56	0.73	CH6-30	-8.60	0.20	2115.1	212.6	3.20	0.58
CH6-9	-7.93	0.21	1151.2	116.1	6.70	0.92	CH6-30	-9.25	0.21	2441.8	246.3	3.04	0.58
CH6-9	-8.04	0.21	1427.0	143.9	6.02	0.85	CH6-30	-8.85	0.34	2074.1	209.5	3.42	0.59
CH6-9	-8.17	0.20	1308.7	131.6	5.99	0.88	CH6-32	-8.82	0.20	2156.3	219.4	5.20	0.67

Sample ID	$\delta^{13}C$ (‰) (VPDB)	2σ error (‰)	N (at. ppm)	2σ error (ppm)	$\delta^{15}N$ (AIR)	2σ error (‰)	Sample ID	$\delta^{13}C$ (‰) (VPDB)	2σ error (‰)	N (at. ppm)	2σ error (ppm)	$\delta^{15}N$ (AIR)	2σ error (‰)
CH6-32	-7.95	0.20	1731.1	173.9	3.52	0.57	CH6-43	-4.94	0.20	3291.5	331.7	1.79	0.58
CH6-32	-5.96	0.20	3199.2	323.6	3.51	0.59	CH6-43	-5.33	0.20	2877.6	290.0	1.60	0.61
CH6-32	-8.68	0.21	3345.2	337.4	2.80	0.56	CH6-45	-9.86	0.21	2740.8	283.0	0.08	0.60
CH6-33	-7.60	0.20	3048.3	307.4	0.16	0.58	CH6-45	-6.43	0.21	1489.2	149.7	-3.74	0.72
CH6-33	-7.51	0.21	3271.3	330.2	-0.06	0.60	CH6-45	-6.91	0.20	1583.2	160.4	-4.61	0.73
CH6-33	-7.48	0.20	3832.6	386.6	-0.03	0.62	CH6-46	-22.75	0.21	4.0	0.4		
CH6-34	-17.70	0.21	48.6	5.1	13.00	3.42	CH6-46	-6.62	0.21	1376.7	138.6	-5.14	0.82
CH6-34	-17.42	0.21	56.5	6.0	12.54	3.82	CH6-46	-22.72	0.21	0.4	0.0		
CH6-34	-17.56	0.20	40.2	4.2			CH6-46	-22.68	0.20	0.4	0.0		
CH6-35	-5.60	0.21	1776.6	178.0	-3.07	0.76	CH6-46	-6.59	0.21	1305.4	131.8	-3.59	0.82
CH6-35	-6.19	0.21	1698.6	171.3	-3.18	0.79	CH6-46	-6.51	0.20	1355.9	136.6	-4.73	0.80
CH6-35	-7.18	0.20	1792.1	179.7	-4.20	0.86	CH6-46	-6.33	0.21	1093.9	109.9	-4.73	0.90
CH6-37	-4.32	0.21	498.7	50.4	3.56	1.36	CH6-47	-28.62	0.20	4.3	0.4		
CH6-37	-4.33	0.20	487.5	49.3	1.88	1.35	CH6-47	-28.38	0.21	5.5	0.6		
CH6-37	-4.38	0.22	491.2	49.6	3.26	1.32	CH6-47	-28.04	0.21	5.6	0.6		
CH6-38	-13.83	0.20	1058.3	107.3			CH6-48	-4.24	0.22	2530.8	255.2	3.20	0.65
CH6-38	-13.93	0.20	1819.5	183.6			CH6-48	-4.13	0.20	2048.0	206.5	3.39	0.67
CH6-38	-13.99	0.21	2315.0	233.4			CH6-48	-4.14	0.21	2668.4	269.2	2.20	0.62
CH6-39	-6.02	0.21	40.1	4.2	15.57	3.20	CH6-48	-4.21	0.20	2979.8	300.6	2.68	0.68
CH6-39	-5.93	0.20	1216.8	122.9	10.41	1.10	CH6-49	-6.70	0.21	1993.5	200.9	-2.79	0.76
CH6-39	-6.28	0.20	1178.7	119.2	11.31	1.05	CH6-49	-4.84	0.21	3346.8	337.7	0.81	0.57
CH6-40	-2.75	0.21	400.9	41.0	6.49	1.44	CH6-49	-4.80	0.22	2264.9	229.7	2.94	0.69
CH6-40	-3.08	0.21	8.7	0.9			CH6-50	-5.64	0.21	1347.9	136.6	-1.88	0.80
CH6-40	-3.15	0.20	7.0	0.7			CH6-50	-5.26	0.21	1228.0	124.1	-1.57	0.85
CH6-42	-6.47	0.20	76.2	7.8	-0.55	4.38	CH6-50	-5.22	0.20	1844.1	185.6	-0.77	0.70
CH6-42	-6.46	0.21	65.1	6.8	0.90	3.63	CH6-51	-5.01	0.21	611.0	61.6	-3.87	1.25
CH6-42	-5.79	0.20	86.3	8.9	-2.90	3.99	CH6-51	-4.59	0.20	1433.8	144.6	-3.50	0.87
CH6-43	-5.94	0.21	3335.6	335.1	2.56	0.59	CH6-51	-5.66	0.20	728.0	75.3	6.70	2.00

Table 4.2 $\delta^{13}C$, nitrogen content and $\delta^{15}N$ for multiple analyses of 94 Chidliak diamonds. $\delta^{13}C$ and nitrogen contents were measured on the same spots and $\delta^{15}N$ was measured on adjacent spots along the same growth zones.

4.2.4.2 Carbon:

The carbon isotopic signature of diamond can act as a robust fingerprint for its upper mantle source. Carbon has two stable isotopes, ^{12}C and ^{13}C, and the ratio is expressed as $\delta^{13}C$ (measured in ‰) relative to the international Vienna Pee Dee Belemnite (VPDB) standard. A diamond with a $\delta^{13}C$ value of -10‰ has a $^{13}C/^{12}C$ ratio that is 10‰ lower than that of the standard. Chidliak diamonds show a range in $\delta^{13}C$ between -28.6‰ to -1.3‰, with a principle mode at -6‰ near the value of mantle carbon and a minor secondary mode around -15‰ (Figure 4.7). Diamonds from kimberlite CH-6 have a slightly lower principle mode at -7‰. Multiple points (2 to 7 points, average of 3 points), were measured per diamond

and not averaged. Chidliak diamonds ≥425 μm and <425 μm also have similar

carbon characteristics.
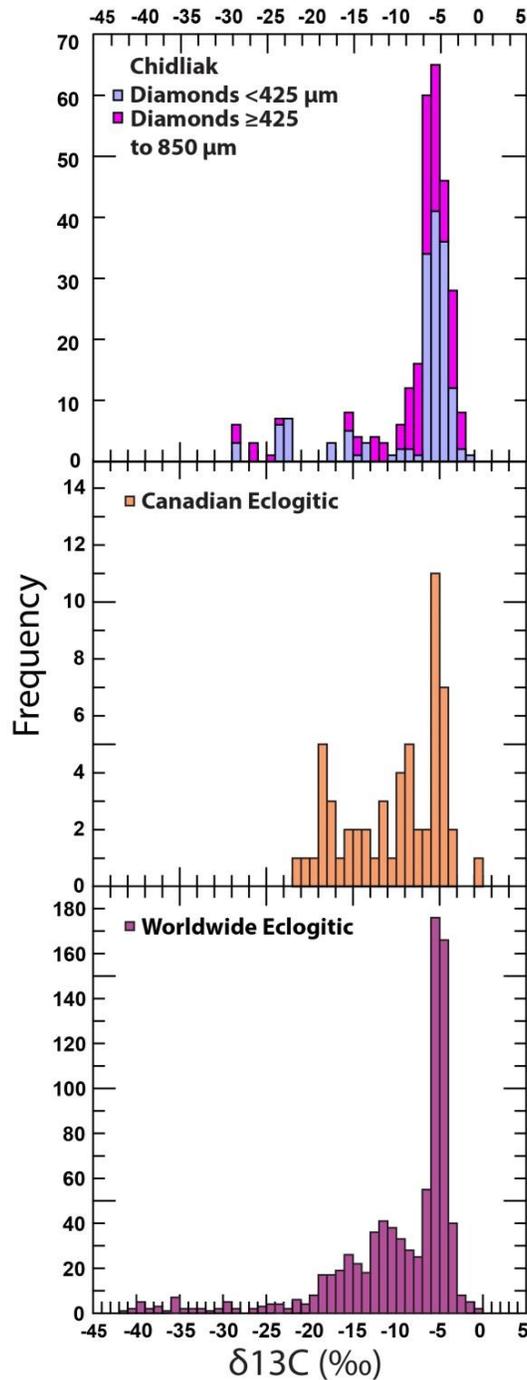
Figure 4.7. Histogram showing the range in $\delta^{13}C$ for Chidliak diamonds (multiple point analyses per diamond are shown), compared to worldwide eclogitic and peridotitic diamonds (bulk analyses) from the database of Stachel and Harris

(2008). For Chidliak diamonds, a primary mode is observed around -6‰, with a secondary mode about -15‰.

4.2.4.3 Correlations Between CL Patterns, δ^{13}C and N Content

CL images the exposed surface of diamonds, with differences in luminosity being related to differences in concentrations of impurities and defects (Wilks and Wilks, 1991). CL allows for the identification of internal growth bands and resorption fronts. The diamonds imaged by CL in the current study were not oriented on specific growth faces due to mounting procedures. In addition, as multiple diamonds were polished in single mounts, sections through the crystal centres were only achieved in rare cases. Such random sections through only part of the diamond crystals introduce artificial complexity to the CL images.

Identified types of CL for Chidliak diamonds include: (1.) "hiatus", (2.) "homogenous", (3.) "agate-like banding", (4.) "octahedral", (5) "cuboid" and (6.) "complex" (Figure 4.8). Hiatuses involve abrupt, strong changes in CL response that are usually accompanied by sharp changes in δ^{13}C from very negative to mantle-like δ^{13}C values and an increase in nitrogen content. Diamonds with homogenous CL show neither growth bands nor large changes in δ^{13}C or nitrogen content. Agate-like banding (multiple narrow growth bands) can coincide with small changes in δ^{13}C and nitrogen content. Octahedral and cuboid CL types have growth bands that can be identified as representing a particular symmetry based on the angles between growth layers, and by a hummocky appearance for cubic growth.
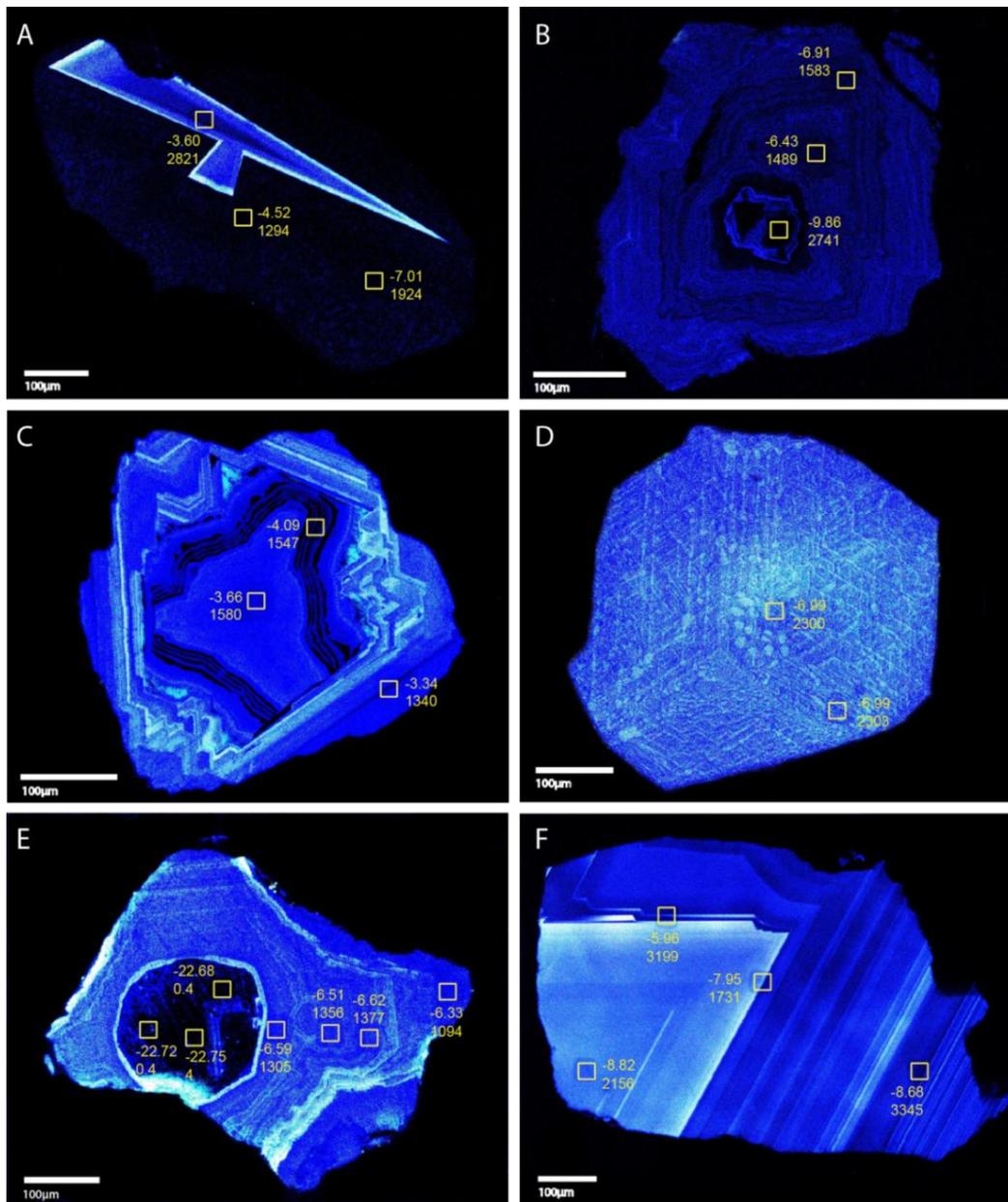
Figure 4.8. Annotated CL images. Spot size for SIMS analyses is approximately 15 µm; for each spot $\delta^{13}C$ (‰) is given above the nitrogen content (at. ppm). Diamond A has two spear like areas that likely relate to octahedral directions, with a "micro-breccia" like pattern in the dark CL zone, $\delta^{13}C$ and nitrogen contents change significantly across the diamond. Diamond B is an aggregate, with two small dark areas which likely represent two small initial diamonds with growth bands continuing around this combined core; again significant changes in $\delta^{13}C$ and nitrogen content are observed with changes in CL. Diamond C is a "centre-cross pattern" (reflecting mixed habit growth), with an external octahedral shape. The centre-cross pattern is truncated by the octahedral growth. Diamond D possibly demonstrates the CL response of platelets, which are oriented along octahedral planes. Diamond E is likely a re-entrant cube with a hiatus from very

82

dark CL to lighter banded CL. An abrupt change of $\delta^{13}C$ and nitrogen content is observed across the hiatus. Diamond F demonstrates both agate like banding and octahedral growth; changes in $\delta^{13}C$ and nitrogen content are more subtle.

4.3 Discussion:

4.3.1 Thermal History:

If the mantle residence period is known, it is possible to use the measured nitrogen abundance and aggregation in a diamond to calculate a time-averaged mantle residence temperature (Taylor et al., 1990; Leahy and Taylor, 1997). The exact mantle residence time of Chidliak diamonds is, however, unknown; based on the assumption that, like most diamonds with dated inclusions, Chidliak diamonds had a mantle residence in the 1-3 Ga range (Gurney et al. 2010), the exact choice of a residence time becomes almost irrelevant. For 1 and 3 Ga, the difference in average mantle residence temperatures for Chidliak diamonds is 21-35°C. The mantle residence time chosen here is 1 Ga, as diamonds of eclogitic paragenesis typically form during the Proterozoic (eg., Richardson., 1986; Richardson et al., 1991; Smith et al., 1991). The temperatures derived by this method usually compare reasonably well to those obtained by mineral inclusion based geothermobarometry (Leahy and Taylor, 1997).

Only high quality IR spectra were used to determine temperature and, consequently, 20% of the diamonds were excluded from temperature estimates. For pure Type IaA diamonds (0% nitrogen in the B centre), an assumed value of 0.5% B was used for the temperature calculations (i.e., calculated temperatures for these diamonds represent a maximum value). Multiple analyses were completed for each diamond to detect any variations in aggregation state and nitrogen content within individual diamonds. Variations in nitrogen content and

83

aggregation state among multiple analyses of single diamonds lead to apparent

temperature differences of up to 92°C, but the majority (75%) of diamonds have

apparent temperature differences less than 25°C. For an assumed mantle residence

of 1 Ga, Chidliak diamonds show a range in temperature from ~980 to 1410°C.

The 1410°C temperature is discarded, as an upper limit cut off of 1400°C is

applied because temperatures greater than 1400°C exceed lithospheric

temperatures (Stachel and Harris 2008), thus the true range in temperature for

Chidliak diamonds is from ~980 to 1350°C (Figure 4.9). 96% of diamonds fall

within the range of 1000-1150°C, 68% between 1050-1150°C, and 66% between

1000-1100°C (Figure 4.10).
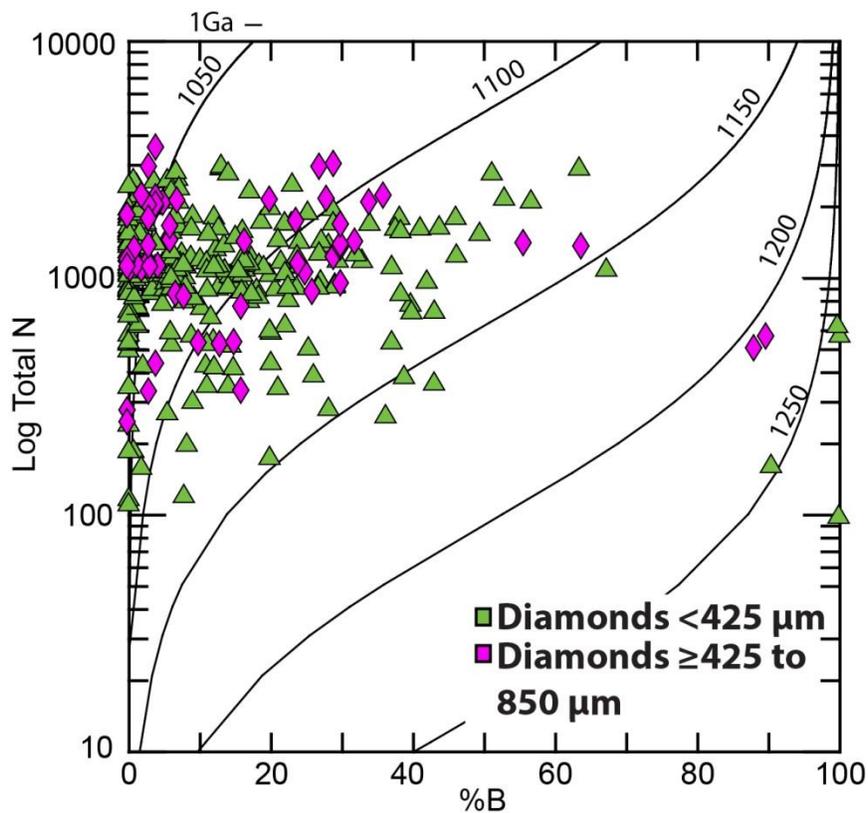
Figure 4.9. Time-averaged mantle residence temperatures for diamonds from
kimberlites CH-6 and CH-7. Isotherms are calculated using an assumed mantle
residence time of 1 Ga (after Taylor et al. 1990 and Leahy and Taylor, 1997).

Total N is in atomic ppm, nitrogen aggregation is expressed as %B, i.e., the relative proportion of nitrogen in the B centre.
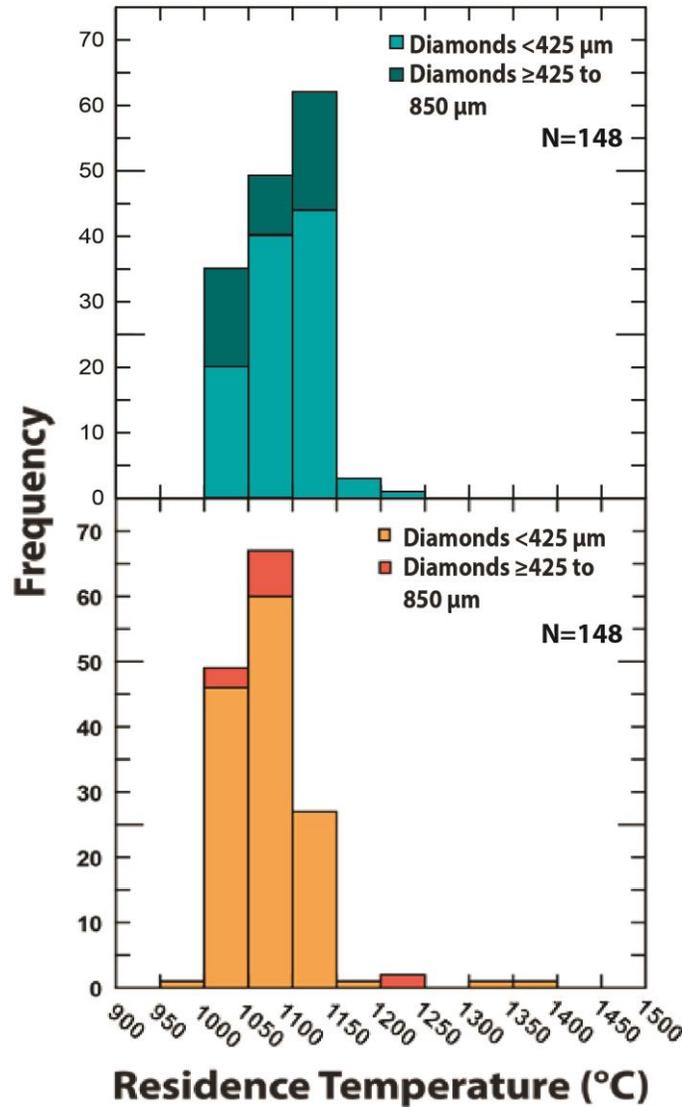
Figure 4.10. Histogram showing calculated mantle residence temperatures; the top histogram is for diamonds from kimberlite CH-6, the bottom is for diamonds from kimberlite CH-7. Chidliak diamonds show a range in temperature from ~980 to 1350°C. The majority of diamonds fall within the mantle residence temperature range of 1000-1150°C, with diamonds from kimberlite CH-6 showing slightly higher residence temperatures. N represents the number of analyses; where possible two analyses per diamond were included, but in some cases only one IR spectrum of sufficiently high quality was obtained.

Pell et al. (2012) used the geothermobarometer of Nimis and Taylor

(2000) to delineate a cool cratonic geotherm for the lithospheric mantle beneath

Chidliak and to derive an inflected geotherm entering the diamond stability field

at 900°C (corresponding to a depth of ~140 km) (Figure 4.11).
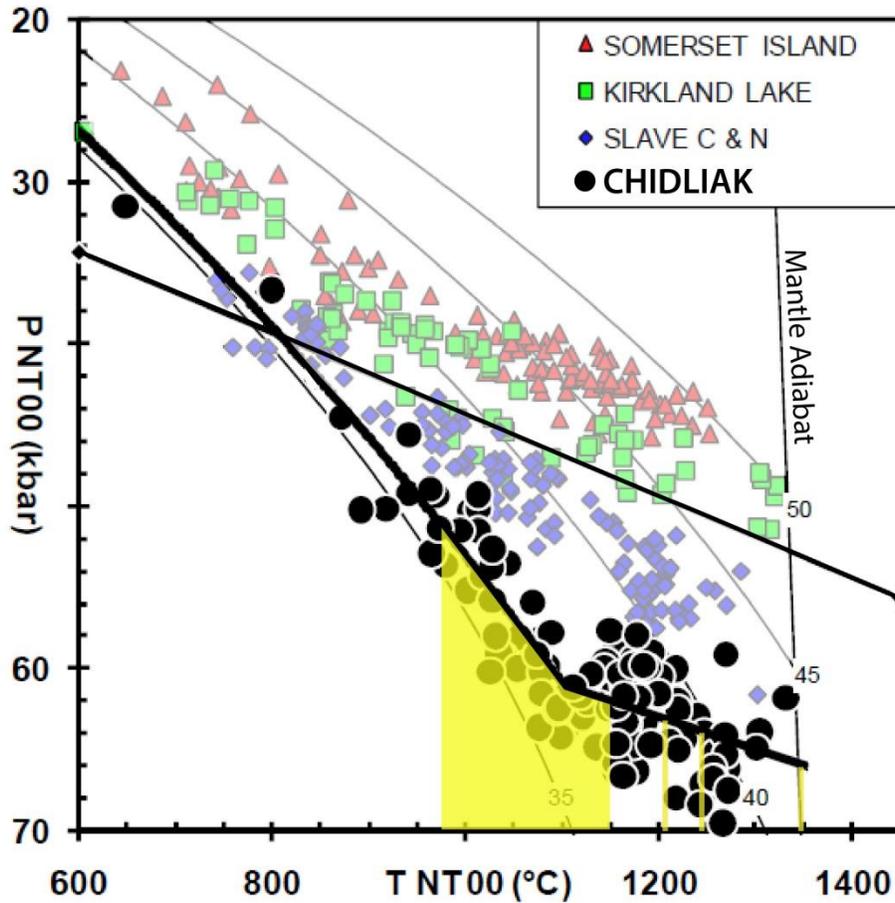
Figure 4.11. Single clinopyroxene geothermobarometry (using Nimis and Taylor 2000) and a resulting geotherm for Chidliak (Pell et al. 2012). The Chidliak geotherm is interpreted to be inflected and is "cool" relative to the central and northern Slave, Kirkland Lake and Somerset Island. The wide and the thin yellow bands represent the calculated mantle residence temperatures for Chidliak diamonds superimposed along the geotherm. There is a gap between the majority of the diamonds (1000-1150°C) and the three diamonds at higher temperatures (thin yellow bands).

Assuming that mantle residence temperatures are directly linked to the

depth at which diamonds resided, a lack of data for the deeper portion of the

lithosphere is apparent. This could be due to a number of reasons; the first

possibility is that the subcratonic lithospheric mantle is heterogeneous beneath

Chidliak, where diamonds are formed in favourable conditions at a depth corresponding to a temperature range of 1000-1150°C. The second is that the erupting kimberlites preferentially sampled diamonds within this temperature range. The third possibility is that a thermal perturbation destroyed diamonds that originally had formed at higher temperatures (=greater depth). This third possibility is considered the least likely, given that strong thermal pulses should be accompanied by platelet degradation (Evans at al., 2005), which is not the case for the vast majority of Chidliak diamonds.

The few Chidliak diamonds showing platelet degradation may have been exposed to an elevated shear stress during mantle residence. Seven diamonds have one spot indicating the diamond is regular and one spot indicating the diamond is irregular, and are shown with tie lines in Figure 4.3. Five of these diamonds come from kimberlite CH-6 and two come from kimberlite CH-7. Since FTIR in transmitted mode is a "bulk" technique it is not possible to locate where the platelet degraded zones are located in these diamonds (ie. whether they represent the diamond core or rim). It is possible that the irregular portions of these diamonds represent the presence of cuboid growth sectors. Although previous studies have shown that cuboid growth sectors are typically hydrogen-rich (e.g., Howell et al., 2012) this might not invariably be the case. If these "irregular" diamond portions actually represented cuboid growth sectors then no platelet degradation event would be required. Another possibility is that these diamonds grew slowly, with the older diamond cores having experienced a strain event, while the younger overgrowth did not. However, two episodes of diamond growth

separated by a very large (e.g., 1 Ga) period of time is inconsistent with very similar mantle residence temperatures for the diamond portions with and without platelet degradation.

4.3.2 Hydrogen and Nitrogen Relationship:

The hydrogen-related peak at 3107 cm^{-1} (stretching mode of the C-H bond) is linked to the hydrogen peak at 1405 cm^{-1} (bending mode of the C-H bond) (Fritsch et al., 2007): as the peak intensity increases at 3107 cm^{-1} it also increases at 1405 cm^{-1}. The main peak at 3107 cm^{-1} is larger than the secondary peak by almost an order of magnitude (Figure 4.12).
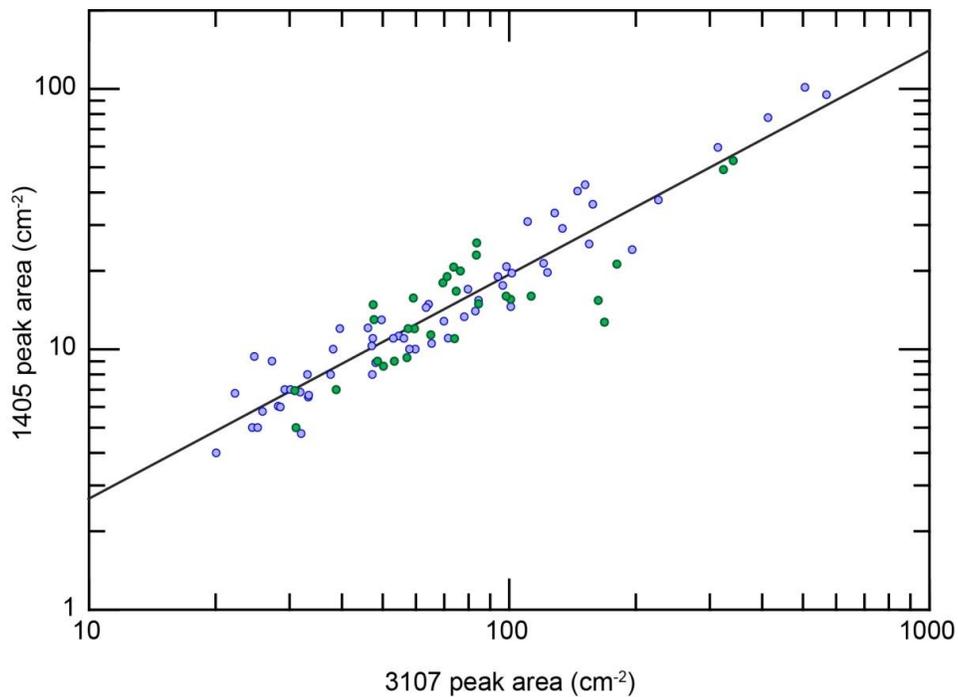
Figure 4.12. Relationship between the intensity of the 3107 cm^{-1} and 1405 cm^{-1} hydrogen peaks, a strong linear correlation is observed. Green circles represent measurements of diamonds from kimberlite CH-6, whereas blue circles represent measurements of diamonds from kimberlite CH-7.

It has also been observed in previous studies that the main IR-active hydrogen peak is correlated with the nitrogen content in diamond. Goss et al.,

(2002) assigned the peak at 3107 cm^{-1} to the high temperature stable N-H defect. Rondeau et al., (2004) suggested that the hydrogen is trapped between the diamond lattice and a nitrogen aggregate (either A or B) in a C-N bond; for cubic diamonds it is assumed that it is the nitrogen A aggregate because of the low nitrogen aggregation in their samples. A correlation was also identified between the 3107 cm^{-1} peak absorbance and nitrogen content in synthetic diamonds (Kiflawi et al., 1996).

For Chidliak diamonds the maximum peak intensity at 3107 cm^{-1} shows a blurred linear increase with nitrogen in the B centre (N_B) (Figure 4.13). A similar upper envelope was previously identified by Melton (2013), using a large database of IR spectra for diamonds from worldwide sources. This suggests that the maximum 3107 cm^{-1} peak intensity is controlled by the aggregation state of the nitrogen. This implies that hydrogen is already present in the diamond lattice but only becomes infrared active during nitrogen aggregation, due to the formation of new centres likely composed of hydrogen and nitrogen. Consequently, hydrogen contents in diamonds may be higher than represented by the 3107 cm^{-1} peak, because not all hydrogen is necessarily IR-active. Values plotting below the envelope line could relate to a lack of available hydrogen in the source fluid.
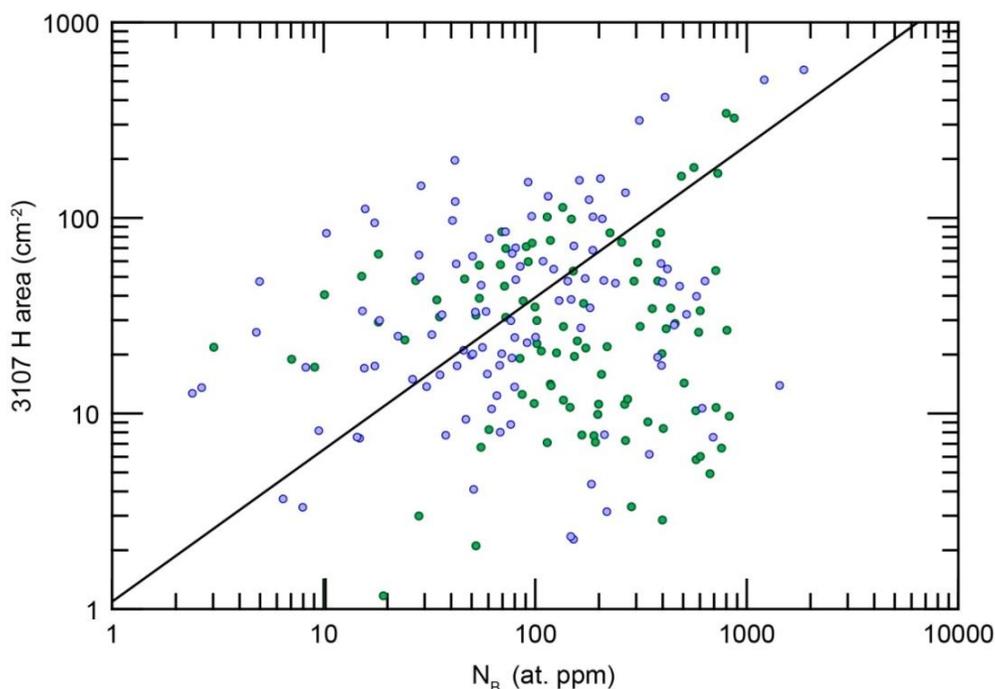
Figure 4.13. The relationship between the hydrogen peak intensity at 3107 cm^{-1} and nitrogen in B-centres (N$_B$), for diamonds with high-quality spectra from kimberlite CH-7 (blue circles) and CH-6 (green circles). Where possible, two spots per diamond were analyzed and are shown. Implicitly, Type II and pure Type IaA diamonds are excluded from this plot. The black line represents a linear relationship between maximum hydrogen peak intensity and nitrogen concentration in B centres (after Melton, 2013) Chidliak diamonds in part fall above this envelope line, suggesting that Chidliak diamonds are enriched in IR-active hydrogen.

Many of the Chidliak diamonds, however, plot above the envelope line defined by Melton (2013), suggesting that the formation of the 3107 cm^{-1} centre is not exclusively limited by how far nitrogen aggregation has progressed. This is consistent with the observation of 3107 cm^{-1} centres in the majority of Chidliak Type II diamonds.

A linear relationship between maximum peak intensity at 3107 cm^{-1} and total nitrogen content was previously observed for diamonds from Argyle and attributed to diamond formation in a NH$_3$ or NH$_4$-rich environment, while diamonds falling distinctly below the envelope line formed in an N$_2$-rich but H-

poor environment (Iakoubovskii and Adriaenssens, 2002). This model, however, fails to explain the strong relationship between nitrogen in B centres and maximum 3107 cm^{-1} peak intensity (see above); the observation of Iakoubovskii and Adriaenssens (2002) likely relates to the fact that nitrogen aggregation in Argyle diamonds is generally very high (Harris and Collins, 1985) i.e., for many Argyle diamonds total nitrogen content and nitrogen in B centres have similar values.

4.3.3 Carbon Isotope and Nitrogen Content Relationship:

Frequency distributions of diamonds of peridotitic and eclogitic paragenesis both have a prominent mode at approximately -5 ±1‰ (mantle value of carbon) (Deines, 1980; Cartigny, 2005). Diamonds of peridotitic paragenesis, however, have carbon isotopic compositions showing a much narrower range (~0 and -10‰) than eclogitic diamonds (+5 and -40‰) (e.g., Kirkley et al., 1991; Stachel et al., 2009). With few exceptions (e.g., Premier mine; Deines, 1984), a δ^{13}C distribution skewed to the ^{13}C depleted side of the mantle value and extending below -10‰ is characteristic for eclogitic diamond populations worldwide (eg., Deines, 1980; Cartigny et al, 2001; Stachel and Harris, 2009). Chidliak diamonds, with their prominent tail to ^{13}C depleted compositions, resemble the carbon isotopic distributions of eclogitic diamonds from Canada and from worldwide sources (Figure 4.7).

Nitrogen concentrations found in diamond vary greatly from below the limit of detection (about 5-10 at. ppm for FTIR) to about 3500 ppm, with an average value of approximately 200-300 at. ppm (Cartigny, 2005). Nitrogen

concentrations can be used to obtain broad constraints on possible upper-mantle diamond sources; the median nitrogen content for diamonds from peridotitic sources is 70 at. ppm and for diamond from eclogitic source it is 370 at. ppm (Stachel et al., 2009). For Chidliak diamonds, nitrogen contents range from ≤10 at. ppm (Type II) up to 3830 at. ppm, with 28 diamonds exceeding 1500 at. ppm. The association of a significant proportion of ^{13}C depleted diamonds with overall high nitrogen contents in Chidliak diamonds suggests the presence of a large to dominant eclogitic component. In agreement with this conclusion, Neilson et al. (2012), in a study of mantle xenocrysts at Chidliak found that eclogitic (G3D) and eclogitic-websteritic (G4D) facies garnets are significant for both the northern lobe of the CH-7 kimberlite (90.1% of garnets) and for the CH-6 kimberlite (71.6% of garnets).

The relationship between δ^{13}C and nitrogen for eclogitic diamonds has been well established (eg., Deines, 1980; Cartigny et al, 2001; Stachel and Harris, 2009). Diamonds with δ^{13}C values close to -5‰ show a high variability in nitrogen contents, which decreases to more ^{13}C-depleted compositions. For Chidliak diamonds, as δ^{13}C decreases, so does the maximum nitrogen content, which is consistent with the trend identified for eclogitic and websteritic diamonds by Stachel and Harris (1997). Compositional variations within individual diamonds, however, does not always follow this general trend, as in some instances as δ^{13}C values decreases total nitrogen increases.

The origin of isotopically light diamond carbon still is highly controversial. One model suggests open system isotopic fractionation at mantle

temperatures; Javoy et al. (1986), proposed that if a carbon reservoir was repeatedly distilled then "reservoir effects" could cause strongly negative $\delta^{13}C$ for eclogitic diamonds. Cartigny et al. (2001) built upon this model suggesting that open system isotopic fractionation involving CO_2 occurs in the growth medium prior to diamond precipitation, progressively depleting the residual fluid/melt in ^{13}C. This model also introduced the idea of a mantle melt evolution curve or "limit sector" in $\delta^{13}C$ -N space for eclogitic diamonds, and argued that nitrogen is incorporated into diamond not based on the concentration in the growth medium but depending on the growth rate of diamond (i.e., kinetically controlled) (Cartigny et al., 2001). The limit sector defines the maximum nitrogen content in diamond for a given $\delta^{13}C$ value; rapidly growing diamonds plot along the curve, while the diamonds plotting below represent slow growth with low uptake of nitrogen (Cartigny et al., 2001). In this model diamonds with variable $\delta^{13}C$ and N may form from a single mantle reservoir and diamond is merely a "passive recorder" of variations in $\delta^{13}C$ caused by the escape of a ^{13}C and N-enriched fluid from a carbonate bearing melt. The diamond with the highest nitrogen content would represent a best estimate for the original nitrogen-$\delta^{13}C$ relation in the growth medium (Cartigny et al., 2001). For Chidliak this would correspond to a nitrogen content of 3833 at. ppm at a $\delta^{13}C$ of -7.5‰ (diamond CH6-33).

A second model, proposed by Deines (1980), identified seven reactions for diamond formation, such as the oxidation of CH_4 or the reduction of CO_2, and suggested that high-temperature carbon isotope fractionation can take place during diamond growth but that the overall effect of these processes would be

small. Deines (1980) concluded that the observed large range in diamond $\delta^{13}C$ was likely not caused by open system isotopic fractionation, but relates to primordial heterogeneity of the mantle remaining from terrestrial accretion, with single kimberlites sampling several distinct diamond populations (Deines et al., 1993).

A third model suggests that crustal carbon is recycled into the mantle through subduction (eg., Sobolev and Sobolev, 1980; Milledge et al., 1983; McCandless and Gurney, 1997). ^{13}C-depleted carbon can then be related to the subduction of organic microbial carbon that is found near seafloor vents or in altered MORB glass, while more ^{13}C-enriched carbon could be explained by the subduction of carbonates (McCandless and Gurney, 1997). Interaction between upwelling mantle melts/fluids and eclogite will remobilize some of the subducted organic matter- or carbonate-derived carbon, explaining why some eclogitic diamonds carry an organic carbon or a carbonate isotopic signature (McCandless and Gurney, 1997).

Chidliak diamonds fit the limit sector curve of Cartigny et al. (2001) relatively well (Figure 4.14). Contrary to the original proposal of Cartigny et al. (2001), it is now assumed that nitrogen is likely incorporated into the diamond lattice due to equilibrium processes and that nitrogen is a compatible trace element in diamond (e.g., Thomassot et al., 2007; Stachel and Harris, 2009). If this is the case then the diamonds falling below the limit sector curve can be explained by closed system processes during diamond precipitation causing additional variations in both nitrogen content and $\delta^{13}C$ values (Stachel and Harris,

2009). The strength of the Cartigny et al. (2001) model is that it explains the difference between δ^{13}C-N distributions of peridotitic and eclogitic diamond: the vast majority of strongly ^{13}C-depleted samples (δ^{13}C <-10‰) are from olivine-free parageneses (eclogitic-webseritic), in which a CO_2 fluid can separate from a carbonate-bearing melt (Luth, 1993), the precondition of the proposed mechanism of isotopic fractionation (Cartigny et al. 2001). The absence of ^{13}C-depleted carbon for the vast majority of peridotitic diamonds is then related to buffering of CO_2 by olivine in harzburgite and lherzolite (Wyllie et al., 1983), effectively preventing separation of a CO_2 fluid from a melt and associated isotopic fractionation. It is, however, virtually impossible to form diamonds with δ^{13}C values below -14‰ using the CO_2 escape model of Cartigny et al. (2001) with an initial melt near the mantle value of -5‰ because unrealistically high fractionation would be required with less than 1% of the initial melt remaining (Smart et al., 2011).
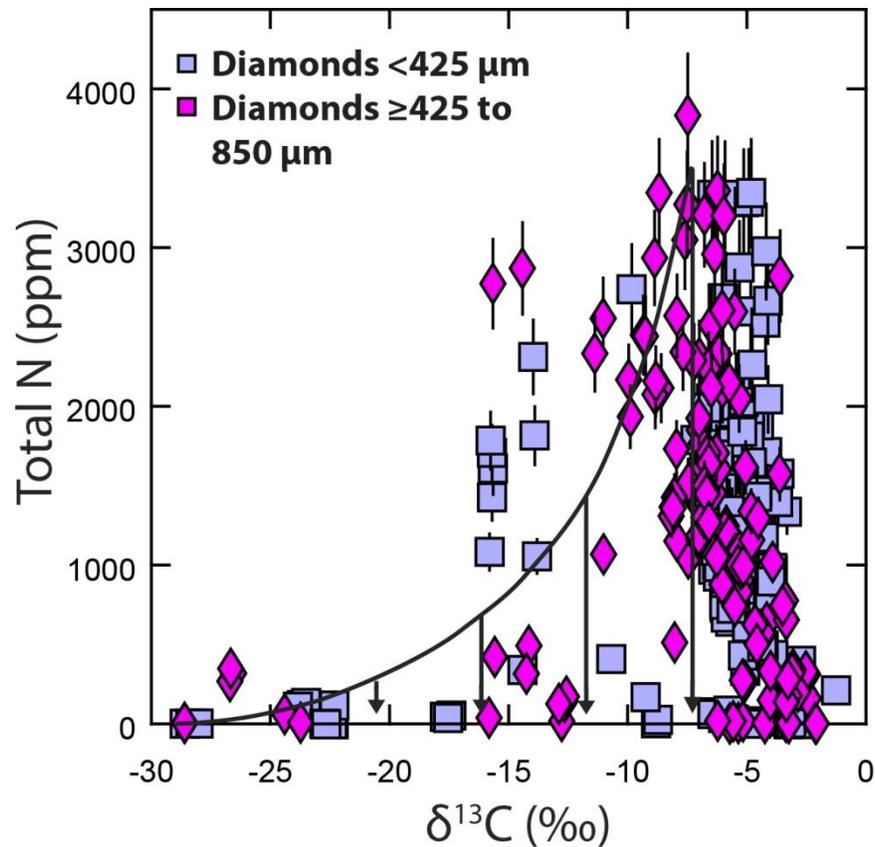
Figure 4.14. $\delta^{13}C$ and nitrogen contents in Chidliak diamonds measured via SIMS, error of $\delta^{13}C$ is smaller than the symbol size. Nitrogen content decreases as $\delta^{13}C$ decreases. The limit sector curve is after Cartigny et al. (2001) and reflects evolution of the diamond precipitating melt. Arrows represent increasingly slow diamond precipitation. Diamonds plotting above the limit sector are attributed to subducted carbon (Cartigny et al. 2001). The majority of Chidliak diamonds plot below this limit sector.

The distribution of the Chidliak diamonds also agrees with the third model (subducted carbon), with $\delta^{13}C$ values extending to -28.6‰, a main mode about -6‰, and some diamonds having $\delta^{13}C$ values up to -1.3‰. Diamonds with carbon isotopic compositions near -5‰ can be explained by precipitation from a mantle melt/fluid that infiltrated eclogitic (or peridotitic) sources, with the diamonds carrying the isotopic signature of these mantle derived fluids (Ickert et al., 2013), or they could represent the $\delta^{13}C$ values of mean altered oceanic crust (-4.7‰ Shilobreeva et al., 2011).

Given that there are abundant eclogitic mantle xenocrysts observed at Chidliak, which suggest sampling of a subducted component in the mantle beneath Chidliak, primordial isotopic heterogeneity is the least likely to explain the carbon isotopic distribution of Chidliak diamonds. It is impossible to determine if only processes associated with hypothesis 1 (isotopic fractionation) or 3 (subducted carbon) were responsible for the carbon isotopic distribution of Chidliak diamonds; however, since eclogite is the high pressure equivalent of oceanic basalts it is likely that the isotopic signatures are at least partially related to subducted oceanic material.

4.3.4 δ^{13}C, δ^{15}N and Nitrogen Content Relationships:

The diamonds from kimberlite CH-7 largely cluster around mantle-like values for both δ^{13}C and δ^{15}N (-5‰ and -5‰, respectively). Diamonds from kimberlite CH-6 are more variable in δ^{13}C and δ^{15}N (Figure 4.15) and a large number of analyses yielded positive δ^{15}N values.
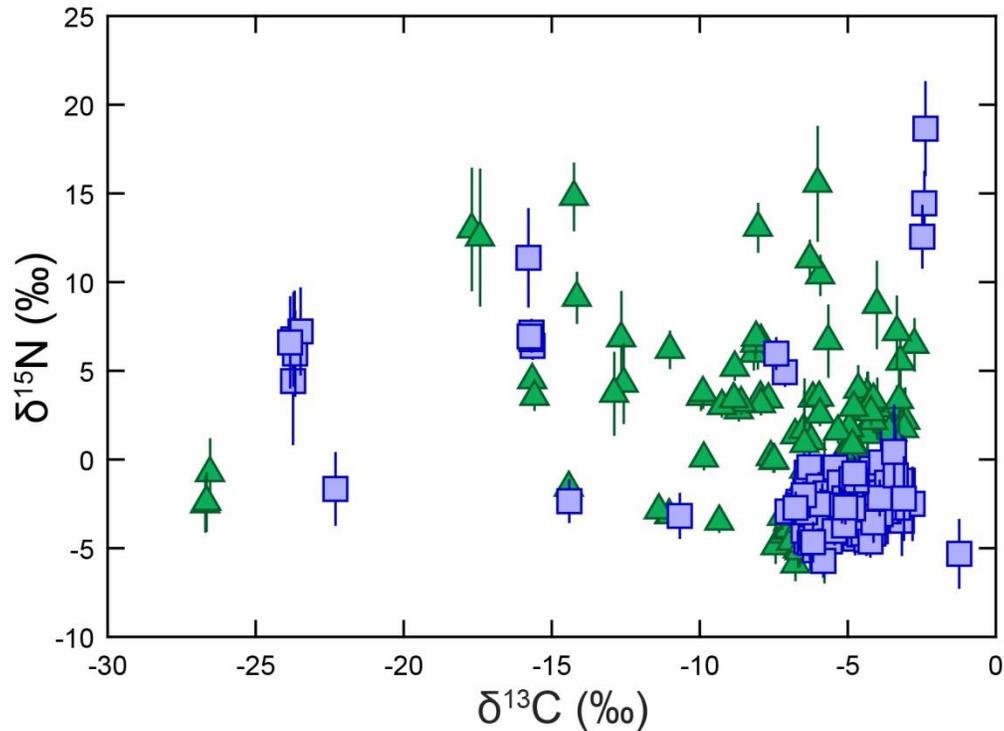
Figure 4.15. Plot of $\delta^{15}N$ vs. $\delta^{13}C$ for diamonds from kimberlite CH-7 (blue squares) and kimberlite CH-6 (green triangles); error of $\delta^{13}C$ is smaller than the symbol size. Diamonds from kimberlite CH-6 show more variability in $\delta^{15}N$ values, but no systematic trends are observed on the scale of individual diamonds. Diamonds from kimberlite CH-7 cluster closer to the expected mantle values for $\delta^{13}C$, whereas the diamonds from kimberlite CH-6 are more variable. Individual spot analyses are not averaged for each diamond.

No systematic co-variations between $\delta^{13}C$ and $\delta^{15}N$ are observed on the scale of individual diamonds. There are, however, systematic co-variations between $\delta^{15}N$ and N for diamonds from both kimberlites. Sub-parallel trends are observed between nitrogen content and $\delta^{15}N$, where nitrogen content decreases as $\delta^{15}N$ increases (Figure 4.16). These trends are also observed on the scale of individual diamonds, although not in the form of systematic core-rim variations (Figure 4.17). The absence of systematic trends away from the centre of crystals may relate to the fact that only few spots (average of 3 spots) per diamond were

analyzed, and that these spots generally were not located within individual growth

bands.
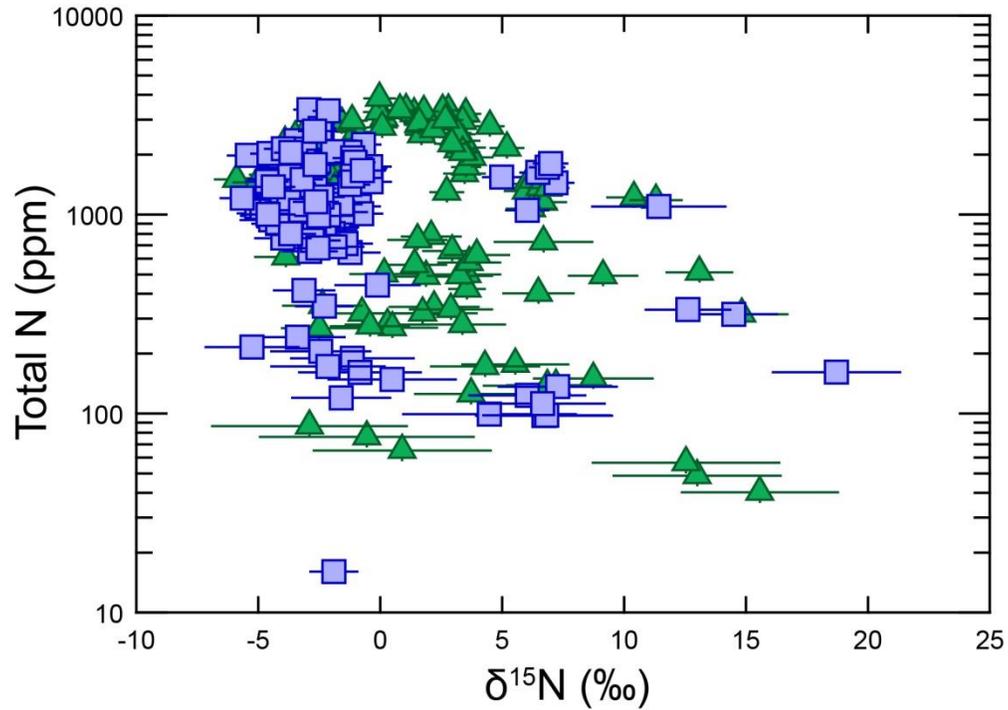
Figure 4.16. Plot of total nitrogen contents against $\delta^{15}N$. The diamonds from kimberlite CH-7 (blue squares) cluster around the mantle value for $\delta^{15}N$ (-5‰), while diamonds from kimberlite CH-6 (green triangles) show more variability. There is a blurred trend of decreasing N content with increasing $\delta^{15}N$. Values are not averaged for each diamond.
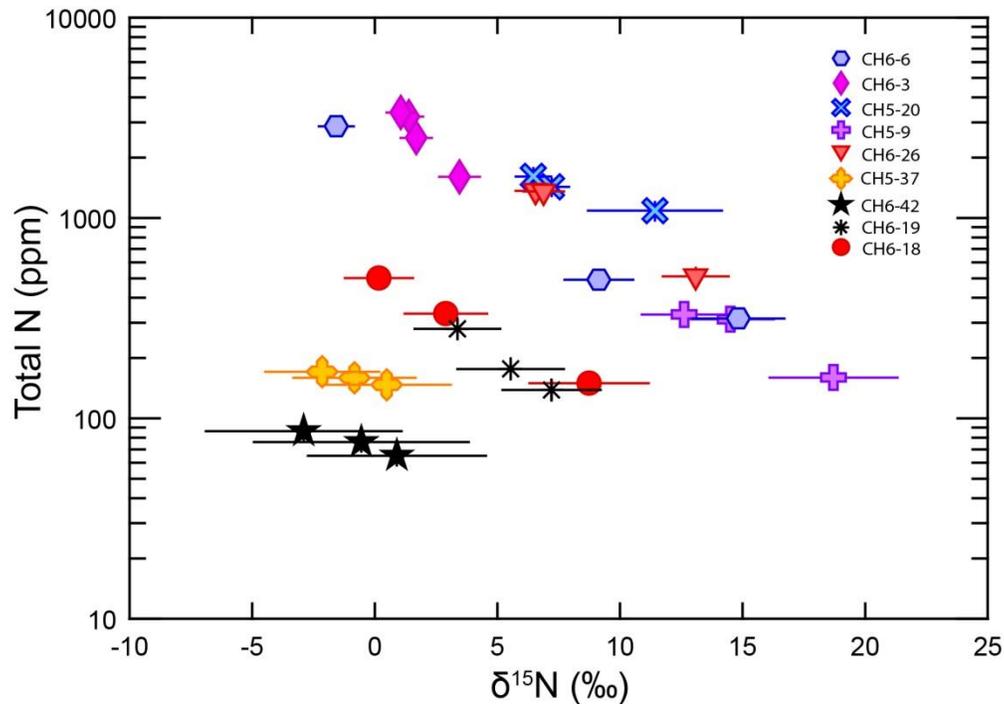
Figure 4.17. Individual diamonds displaying the sub-parallel trends between total nitrogen content and $\delta^{15}N$ values.

Possible explanations of the sub-parallel negative correlations between nitrogen content and $\delta^{15}N$ include: (1.) fractionation of isotopes during diamond precipitation; as diamond precipitates from the diamond forming fluids, fractionation of $\delta^{13}C$ and $\delta^{15}N$ can occur (eg., Boyd et al., 1987; Hauri et al., 2002; Thomassot et al., 2007). (2.) Loss of nitrogen during separation of a CO_2 and N bearing fluid from the diamond forming melt (Cartigny et al., 2001). (3.) Mixing of nitrogen derived from two components: a fluid/melt with variable nitrogen content but mantle-like $\delta^{15}N$ and a second component with variable nitrogen content and $\delta^{15}N$, covering a range to strongly positive values.

Models of $\delta^{13}C$ fractionation during diamond precipitation from carbonates and methane are well established (e.g., Deines, 1980; Stachel and Harris, 2009). Thomassot et al. (2007), modeled the expected variations of $\delta^{13}C$ and $\delta^{15}N$ of diamonds crystallizing from a methane bearing fluid, assuming

positive fractionation factors ($\Delta^{13}C$ of about +1‰ and $\Delta^{15}N$ of about +1.2‰) and

a compatible behavior of nitrogen for the diamond-fluid system (K_N of ~2.0).

These model calculations clearly show that large changes in $\delta^{15}N$ are

accompanied by large changes in $\delta^{13}C$ (Figure 4.18). For diamond precipitation

from carbonate or CO_2 bearing fluids/melts, the fractionation factor for carbon has

a negative sign but is of equal magnitude as ΔN; the rule that variations in $\delta^{15}N$

are invariably associated with changes in $\delta^{13}C$, therefore, equally applies.
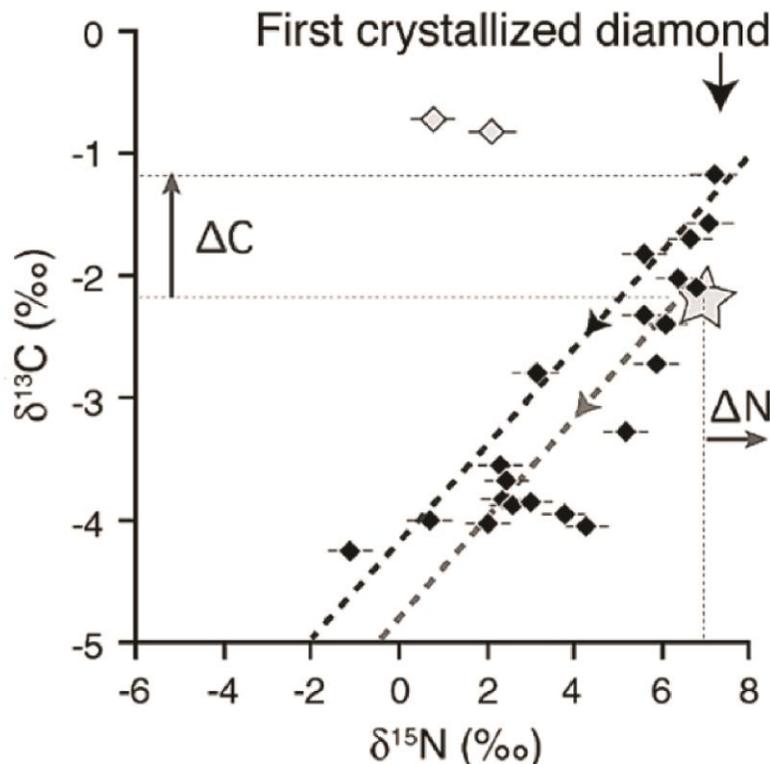
Figure 4.18. Model of diamond crystallization from a methane bearing fluid (Fig. 4 of Thomassot et al., 2007). In this case the fractionation factor $\Delta^{13}C$ is about +1‰, for $\delta^{15}N$, the fractionation factor is estimated to be about +1.2‰. For diamond precipitation from a carbonate or CO_2 bearing fluid, ΔC would be about -1.7‰ or -3.7‰, respectively (Chacko et al., 1991).

For individual Chidliak diamonds, large changes in $\delta^{15}N$ are not

accompanied by significant changes in $\delta^{13}C$ values (Figure 4.19). This decoupled

behaviour $\delta^{15}N$ and $\delta^{13}C$ is not what would be expected from Rayleigh

fractionation during diamond precipitation. This is further investigated here

through modeling of fractionation during diamond formation for two diamonds

that show systematic co-variations between $\delta^{15}N$ and N. Model parameters for

diamond precipitation from a methane bearing fluid are: $\Delta^{13}C$ is positive (+1‰),

and K_N is 2.0 (Thomassot et al., 2007); for precipitation from a carbonate bearing

fluid the parameters are $\Delta^{13}C$ is negative (-1.7‰), and K_N is 2.0 (Figure 4.20)

(Chacko et al., 1991). For both diamonds, large variations in N content are not

matched by significant variations in $\delta^{13}C$. The model calculations show, however,

that this would need to be the case if variations in nitrogen content (and $\delta^{15}N$)

were related to isotopic fractionation during diamond precipitation. This implies

that for Chidliak diamonds carbon and nitrogen isotopes are decoupled.
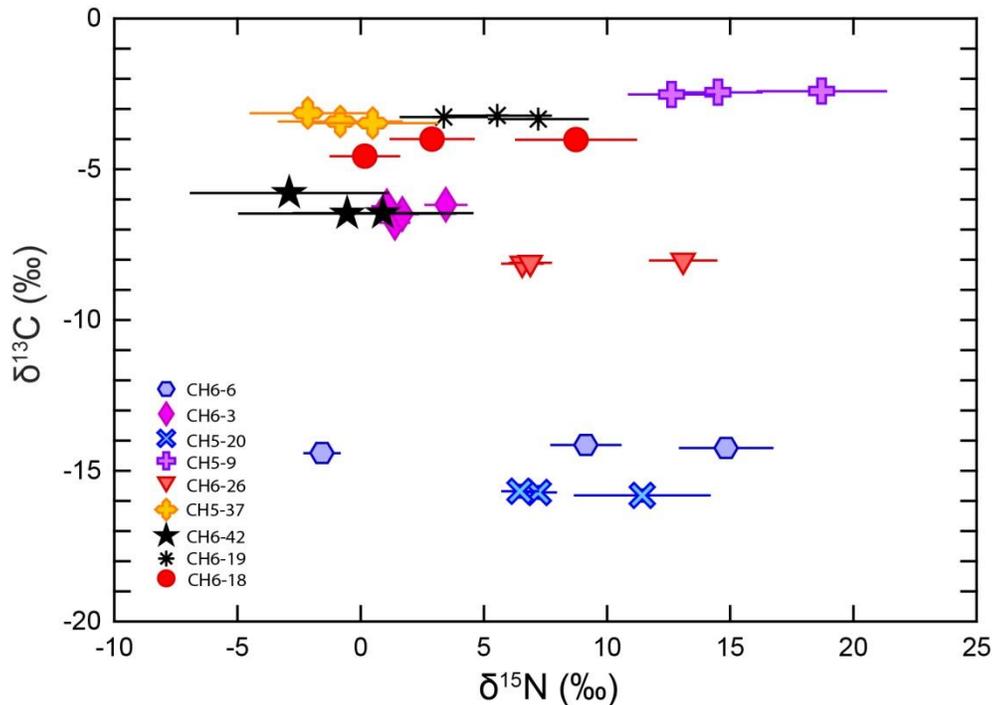
Figure 4.19. Plot of $\delta^{15}N$ and $\delta^{13}C$ values of the same diamonds showing the sub-parallel trends for $\delta^{15}N$ and nitrogen contents, errors of $\delta^{13}C$ values are smaller than the symbol size. Large changes in $\delta^{15}N$ are not associated with variation in $\delta^{13}C$ beyond analytical uncertainty, implying decoupling of carbon and nitrogen isotopes.
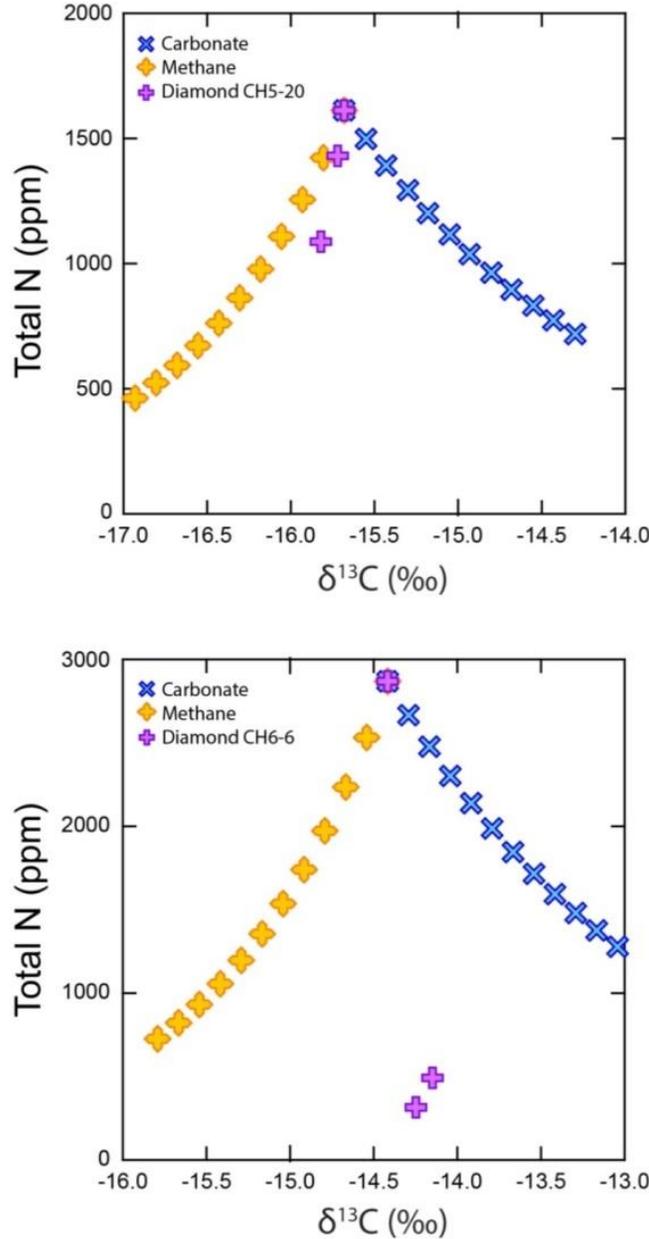
Figure 4.20. Modeled evolution of diamond composition ($\delta^{13}C$ and N content) during precipitation from carbonate and methane bearing fluids/melts in a chemically closed system. Diamonds CH5-20 and CH6-6 show systematic co-variations of $\delta^{15}N$ and N content. The absence of co-variations with $\delta^{13}C$ for CH5-20 and CH6-6 can be satisfied neither by diamond precipitation during oxidation of methane or reduction of carbonates. Therefore, co-variations between nitrogen content and $\delta^{15}N$ cannot relate to fractionation during diamond precipitation either.

The second model – N loss from the diamond precipitating fluid/melt –
would require that this N loss is accompanied by nitrogen isotope fractionation. In
the Cartigny et al. (2001) model, N is lost together with CO_2 during separation of
a fluid from a carbonate bearing melt. Experiments on degassing of MORB
conducted at 100°C suggest a fractionation factor for $\delta^{15}N$ of -1.6‰ between
volatile and residual phases (Cartigny et al., 2001b). The fractionation factor for
$\delta^{15}N$ is unknown for deep mantle conditions (>1000°C), but theoretically,
efficient fractionation of $\delta^{15}N$ during fluid loss is not expected to occur.

Consistent with this interpretation, nitrogen isotope measurements on
mineral separates from arc lavas, ocean island basalts, and mantle xenoliths
suggest that nitrogen isotope fractionation does not occur during magma
degassing (Fischer et al., 2005). Whether or not nitrogen fractionation occurs at
all at mantle conditions is currently unresolved but any possible effects are
expected to be small (Marty and Dauphas, 2003).

Consequently, the only viable model to explain the sub-parallel trends in
$\delta^{15}N$ – N for Chidliak diamonds is mixing, likely of two components, one with
high nitrogen content and negative $\delta^{15}N$, the other with low nitrogen and positive
$\delta^{15}N$. The average nitrogen content of the mantle is much lower than its carbon
content, with the nitrogen content of primitive upper mantle estimated at ~2 ppm
(Marty, 1995) to ~36 ppm (Javoy, 1997), the latter likely represents a maximum
value. Since nitrogen in the mantle is present in such low quantities, it can be used
as a sensitive recorder of mixing between reservoirs. The recycling of subducted
material adds significant amounts of nitrogen to the mantle (Busigny et al., 2003);

however, Archean marine organic matter can have low nitrogen contents ($\leq$106 ppm) (Beaumont and Robert, 1999). The mantle and the subducted component have distinct isotopic signatures: the mantle value of $\delta^{15}N$ is -5$\pm$3‰ (Nadeau et al., 1990; Cartigny, 2005), whereas subducted material, including hydrothermal deposits (Hall, 1989), organic nitrogen, and metasediments, have positive $\delta^{15}N$ values extending from 0 to +18‰ (eg., Peters et al., 1978; Bebout and Fogel., 1992; Cartigny, 2005). The range of $\delta^{15}N$ values measured for MORB is -5.9 to -2.4‰ (Javoy and Pineau, 1991); altered oceanic crust has an average $\delta^{15}N$ value that also is close to the mantle value (Li et al., 2007).

Because of the similarity in charge and ionic radius, NH_4^+ can substitute for K^+ in K-bearing sheet silicates such as clay minerals. During subduction and associated metamorphism of sediments, NH_4^+, can become incorporated into the crystal lattice of various K-bearing minerals, such as micas (e.g., phengite; Busigny et al., 2003), hollandite (Watenphul et al., 2009) and clinopyroxene (Watenphul et al., 2010); this provides a pathway for transport of nitrogen into the deep mantle through subduction of ammonium bearing metasediments and altered oceanic crust.

Based on this brief review, the two components involved in generating the $\delta^{15}N - N$ signatures of Chidliak diamonds most likely represent a subducted metasedimentary component (positive $\delta^{15}N$ values) and a mantle derived component ($\delta^{15}N$ near -5‰). In terms of nitrogen contents, this appears to contradict the expectation that a subducted component should have higher nitrogen contents than the mantle component (c.f., Cartigny et al., 1998)). In view

of the important role of nitrogen storage in minerals and consequently, nitrogen

release during mineral breakdown (e.g. during oxidation of NH^{4+} bearing

minerals, as suggested by Smith et al. (2013), or during partial melting), the total

nitrogen content in the source region(s) of fluid/melt components, or in the

diamond source rock itself, likely only plays a secondary role. An ascending

mantle fluid/melt then may contain higher (although variable) nitrogen contents

than an eclogite derived component (which may be mobilized locally in the

diamond source or mixed into the ascending mantle fluid before reaching the

locus of diamond formation). Variable nitrogen contents, either generated already

as a primary signature of the two mixing components or during nitrogen loss *en

route*, is a requirement for the mixing model to explain the observed trends. Since

the "mantle component" (exemplified by the bulk of diamonds from kimberlite

CH-7) shows strongly variable N at fairly constant $\delta^{15}N$ about -3‰, the process

causing variable nitrogen contents (partial decomposition of potassic minerals or

loss of a nitrogen bearing fluid from a melt) must not have been accompanied by

nitrogen isotope fractionation.

The sub-parallel trends observed for some Chidliak diamonds point to

compositions for the subducted component that are characterized by positive $\delta^{15}N$

and comparatively low nitrogen contents. However, the trends do not converge to

a common composition for the subducted component, implying that this

component must be variable in $\delta^{15}N$, N content or both. Intersecting trend lines

may be tentatively interpreted to suggest isotopic compositions of the subducted

component in the $\delta^{15}N$ range of ~ +17‰, ~ +30‰, with total nitrogen contents in

the 10's to 100's of ppm range (Figure 4.21). Variable nitrogen contents and

variable and strongly positive $\delta^{15}N$ values may relate to fluid loss from a

subducting slab during prograde metamorphism (eg., Haendel et al., 1986; Bebout

and Fogel, 1992; Jia, 2006).
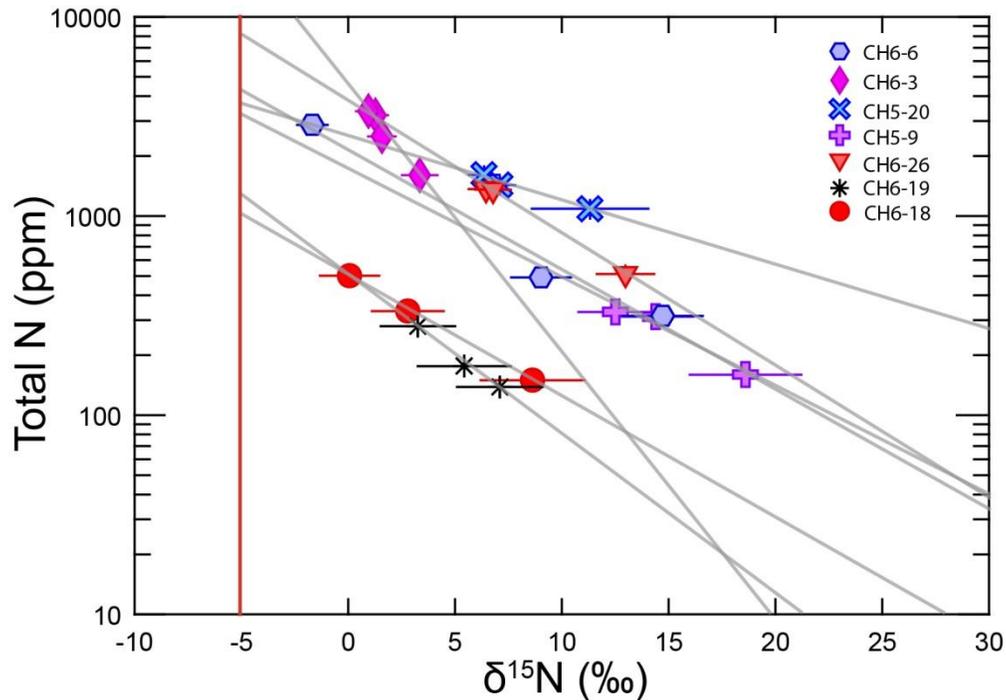
Figure 4.21. Diamonds displaying sub-parallel trends between N content and $\delta^{15}N$ values, error for total nitrogen is typically smaller than the symbol size. The vertical red line represents the mantle value of $\delta^{15}N$, and the light grey lines are linear regression lines. These trends suggest mixing between at least two reservoirs, one being a subducted component with positive but variable $\delta^{15}N$ and/or variable N content and a mantle component with $\delta^{15}N$ fixed near -5‰ and variable N content.

The observation that $\delta^{15}N$ and $\delta^{13}C$ are completely decoupled (Figure

4.19) implies that the carbon isotopic composition of Chidliak diamonds is not

determined by the mixing of the two nitrogen components. This suggests that only

one of the two components carried the bulk of diamond forming carbon; given

that the pure mantle end-member appears to be reflected in a number of

diamonds, this mantle end-member then also would need to be the carbon carrier.

To explain the overall variability in carbon isotopic composition then would require (1.) a mantle reservoir with heterogeneous $\delta^{13}C$, (2.) a process of carbon isotopic fractionation that does not affect $\delta^{15}N$ or N content, or (3.) the involvement of a third component. Given the in part strongly negative $\delta^{13}C$ values of some Chidliak diamonds, exclusive derivation of carbon from a MORB source type reservoir (option 1) appears unlikely. The processes of carbon isotopic fractionation reflected in natural diamonds (Cartigny et al. 2001; Thomassot et al. 2007) all affect nitrogen. This makes involvement of a third component (as a second carbon bearing component) likely. If mixing of the two nitrogen components occurred prior to diamond formation, then this third component could be carbon contained in an eclogitic diamond substrate.

4.3.5 Diamond Source Regions:

FTIR analyses show that the Chidliak diamonds are rich in IR-active hydrogen, only 21%, (N=35) diamonds with high quality spectra do not contain a hydrogen peak at 3107 cm^{-1} in either of the two spots analyzed per diamond. Nitrogen contents are high compared to other eclogitic (and peridotitic) diamonds from the worldwide database (Stachel and Harris, 2008), which suggests that the growth environment was both hydrogen and nitrogen rich.

From CL imaging it is clear that there were at least two distinct diamond forming episodes with distinct $\delta^{13}C$ and N signatures: $\delta^{13}C$ from -22 to -24‰ and N contents ranging from 0.2 to 119 at. ppm in the first event followed by the second growth event with $\delta^{13}C$ ranging from -5 to -7‰ and N contents ranging from 647 to 1616 at. ppm, with resorption event(s) in between. Smaller scale

fluctuations in δ^{13}C (0-3‰, only 12 diamonds without evidence of resorption between growth layers have an intra-diamond variation larger than 1‰) across growth zones visible in CL images suggest multiple pulses of fluid/melt were involved in the growth of Chidliak diamonds. However, trends indicating isotope fractionation during diamond precipitation are not observed.

4.4 Conclusions:

The Chidliak diamonds resided over a range of temperatures in the mantle (~980-1350°C), but a gap is observed between the majority of diamonds (1000-1150°C) and the three diamonds residing at residence temperatures between 1200-1350°C. This suggests that the lithosphere beneath Chidliak may either be heterogeneous in regards to diamond forming sources or that the erupting kimberlites preferentially sampled diamonds from the temperature range of 1000-1150°C. Projecting the mantle residence temperatures on the xenolith/xenocryst based geotherm of Pell et al. (2012), the Chidliak diamonds derive from depths of approximately 150-200 km. Chidliak diamonds are both hydrogen and nitrogen rich, and the IR-active hydrogen is related to the B-component aggregation of nitrogen. Platelet degradation in some of the diamonds suggests that they experienced an elevated shear stress event.

Chidliak diamonds formed from at least two growth events with resorption in between with distinct carbon isotope and nitrogen signatures. Multiple pulses of fluids likely account for the fluctuations in δ^{13}C -N across consecutive growth zones. The δ^{13}C distribution and the overall high nitrogen contents of the Chidliak diamond suite matches the distributions of eclogitic diamonds from worldwide

sources and from other Canadian deposits. Assigning a source paragenesis in the absence of mineral inclusion data has to be viewed with some caution; however, based on the strong similarity with diamonds from other deposits containing eclogitic inclusions it seems very probable that Chidliak diamonds mainly derive from eclogitic sources as well. The interrelationship of $\delta^{13}C$, nitrogen content and $\delta^{15}N$ is complex and likely requires multiple components. The presence of strongly ^{13}C-depleted diamonds ($\delta^{13}C$ -22 to -29‰) and the observation of positive $\delta^{15}N$ values (generally not in the same diamonds) reflect a contribution of subducted organic matter (low $\delta^{13}C$) and oceanic sediments (strongly positive $\delta^{15}N$) to diamond genesis beneath Chidliak. However, carbon and nitrogen are decoupled, as evidenced by systematic co-variations between $\delta^{15}N$ and N content seen in diamonds with constant carbon isotopic composition. This is interpreted to indicate involvement of (at least) three components: (1.) a carbon- and nitrogen-bearing, mantle-derived component with $\delta^{13}C$ about -5‰, $\delta^{15}N$ about -3‰ and variable but overall high nitrogen content. (2.) A fluid/melt derived from subducted and metamorphosed oceanic sediments, with positive $\delta^{15}N$, lower N content than the mantle component and negligible carbon content. (3.) A second subducted component, possibly represented by the eclogitic diamond substrate that contains negligible nitrogen and either variable amounts of ^{13}C-depleted carbon or carbon of variable isotopic composition (mantle-like to strongly ^{13}C depleted). The separation into two subducted components is required to satisfy the decoupling of carbon and nitrogen but is also consistent with the observation of a dominant eclogitic mantle xenocryst component at Chidliak with no evidence for

a meta-sedimentary xenocryst component (i.e., the diamonds did not grow in oceanic sediments).

References:

Allen, B.P. and Evans, T., 1981. Aggregation of nitrogen in diamond, including platelet formation. Proceedings of The Royal Society of London, Series A: Mathematical and Physical Sciences, 375(1760): 93-104.

Beaumont, V. and Robert, F., 1999. Nitrogen isotope ratios of kerogens in Precambrian cherts; a record of the evolution of atmosphere chemistry? Precambrian Research, 96(1-2): 63-82.

Bebout, G.E. and Fogel, M.L., 1992. Nitrogen-isotope compositions of metasedimentary rocks in the Catalina Schist, California: Implications for metamorphic devolatilization history. Geochimica et Cosmochimica Acta, 56(7): 2839-2849.

Boyd, S.R., Mattey, D.P., Pillinger, C.T., Milledge, H.J., Mendelssohn, M. and Seal, M., 1987. Multiple growth events during diamond genesis: an integrated study of carbon and nitrogen isotopes and nitrogen aggregation state in coated stones. Earth and Planetary Science Letters, 86(2-4): 341-353.

Bulanova, G.P., 1995. The formation of diamond. Journal of Geochemical Exploration, 53(1-3): 1-23.

Busigny, V., Cartigny, P., Philippot, P., Ader, M. and Javoy, M., 2003. Massive recycling of nitrogen and other fluid-mobile elements (K, Rb, Cs, H) in a cold slab environment: Evidence from HP to UHP oceanic metasediments of the Schistes Lustrés nappe (western Alps, Europe). Earth and Planetary Science Letters, 215(1-2): 27-42.

Cartigny, P., 2005. Stable isotopes and the origin of diamond. Elements, 1(2): 79-84.

Cartigny, P., Harris, J.W., Javoy, M., 1998. Eclogitic diamond formation at Jwaneng: No room for a recycled component. Science, 280(5368): 1421-1424.

Cartigny, P., Harris, J.W. and Javoy, M., 2001. Diamond genesis, mantle fractionations and mantle nitrogen content: A study of $\delta13C$-N concentrations in diamonds. Earth and Planetary Science Letters, 185(1-2): 85-98.

Cartigny, P., Jendrzejewski, N., Pineau, F., Petit, E. and Javoy, M., 2001b. Volatile (C, N, Ar) variability in MORB and the respective roles of mantle source heterogeneity and degassing: The case of the Southwest Indian Ridge. Earth and Planetary Science Letters, 194(1-2): 241-257.

Chacko, T., Mayeda, T.K., Clayton, R.N. and Goldsmith, J.R., 1991. Oxygen and carbon isotope fractionations between CO_2 and calcite. Geochimica Et Cosmochimica Acta, 55(10): 2867-2882.

Chrenko, R.M., McDonald, R.S. and Darrow, K.A., 1967. Infra-red spectra of diamond coat. Nature, 213(5075): 474-476.

Chrenko, R.M., Tuft, R.E. and Strong, H.M., 1977. Transformation of the state of nitrogen in diamond. Nature, 270(5633): 141-144.

Deines, P., 1980. The carbon isotopic composition of diamonds: relationship to diamond shape, color, occurrence and vapor composition. Geochimica et Cosmochimica Acta, 44(7): 943-961.

Deines, P., Harris, J.W. and Gurney, J.J., 1993. Depth-related carbon-isotope and nitrogen concentration variability in the mantle below the Orapa kimberlite, Botswana, Africa. Geochimica et Cosmochimica Acta, 57(12): 2781-2796.

Deines, P., Gurney, J.J. and Harris, J.W., 1984. Associated chemical and carbon isotopic composition variations in diamonds from Finsch and Premier kimberlite, South Africa. Geochimica et Cosmochimica Acta, 48(2): 325-342.

Dischler, B., Wild, C., Müller-Sebert, W. and Koidl, P., 1993. Hydrogen in polycrystalline diamond. An infrared analysis. Physica B: Physics of Condensed Matter, 185(1-4): 217-221.

Evans, T., Kiflawi, I., Luyten, W., Vantendeloo, G. and Woods, G.S., 1995. Conversion of platelets into dislocation loops and voidite formation in Type IAB diamonds. Proceedings of the Royal Society of London Series A -Mathematical and Physical Sciences, 449(1936): 295-313.

Evans, T. and Phaal, C., 1962. Imperfections in the Type I and Type II diamonds. Proceedings of the Royal Society of London Series A-Mathematical and Physical Sciences, 270(1343): 538-552.

Evans, T. and Qi, Z., 1982. The kinetics of the aggregation of nitrogen atoms in diamond. Proceedings of the Royal Society of London Series A-Mathematical and Physical Sciences, 381(1780): 159-178.

Fischer, T.P., Takahata, N., Sano, Y., Sumino, H. and Hilton, D.R., 2005. Nitrogen isotopes of the mantle: Insights from mineral separates. Geophysical Research Letters, 32(11): L11305.

Fritsch, E., Hainschwang, T., Massi, L. and Rondeau, B., 2007. Hydrogen-related optical centers in natural diamond: An update. New Diamond and Frontier Carbon Technology, 17(2): 63-89.

Goss, J.P., Jones, R., Heggie, M.I., Ewels, C.P., Briddon, P.R. and Öberg, S., 2002. Theory of hydrogen in diamond. Physical Review B - Condensed Matter and Materials Physics, 65(11): 115207-1-115207-13.

Goss, J.P., 2003. Theory of hydrogen in diamond. Journal of Physics - Condensed Matter, 15(17): R551-R580.

Gurney, J.J., Harris, J.W., Rickard, R.S., 1984. Silicate and oxide inclusions in diamonds from the Orapa Mine, Botswana. In: J. Kornprobst (Editor), Kimberlites II: the mantle and crust-mantle relationships. Elsevier, Amsterdam, pp. 3-9.

Gurney, J.J., Helmstaedt, H.H., Richardson, S.H. and Shirey, S.B., 2010. Diamonds through time. Economic Geology, 105(3): 689-712.

Haendel, D., Mühle, K., Nitzsche, H.-M., Stiehl, G. and Wand, U., 1986. Isotopic variations of the fixed nitrogen in metamorphic rocks. Geochimica et Cosmochimica Acta, 50(5): 749-758.

Hall, A., 1989. Ammonium in spilitized basalts of southwest England and its implications for the recycling of nitrogen. Geochemical Journal, 23(1): 19-23.

Harris, J.W., 1987. Recent physical, chemical, and isotopic research of diamond. In: P.H. Nixon (Editor). Mantle Xenoliths. John Wiley & Sons Ltd, Chichester, UK, pp. 477-500.

Harris, J.W., Collins, A.T., 1985. Studies of Argyle Diamonds. Industrial Diamond Review, 45(3), 128-130.

Harris, J.W., Hawthorne, J.B., Oosterveld, M.M. and Wehmeyer, E., 1975. A classification scheme for diamond and a comparative study of South African diamond characteristics. Physics and Chemistry of the Earth, 9(C): 765-783.

Hauri, E.H., Wang, J., Pearson, D.G. and Bulanova, G.P., 2002. Microanalysis of $\delta^{13}C$, $\delta^{15}N$, and N abundances in diamonds by secondary ion mass spectrometry. Chemical Geology, 185(1-2): 149-163.

Heaman, L.M., Grütter, H.S., Pell, J., Holmes, P. and Grenon, H., 2012. U-Pb geochronology, Sr- and Nd-isotope compositions of groundmass perovskite from the Chidliak and Qilaq kimberlites, Baffin Island,

Nunavut. 10th International Kimberlite Conference, Bangalore, India, conference CD (abstract 193).

Howell, D., O'Neill, C.J., Grant, K.J., Griffin, W.L., Pearson, N.J. and O'Reilly, S.Y., 2012. μ-FTIR mapping: Distribution of impurities in different types of diamond growth. Diamond and Related Materials, 29: 29-36.

Howell, D., O'Neill, C.J., Grant, K.J., Griffin, W.L., O'Reilly, S.Y., Pearson, N.J., Stern, R.A. and Stachel, T., 2012b. Platelet development in cuboid diamonds: Insights from micro-FTIR mapping. Contributions to Mineralogy and Petrology, 164(6): 1011-1025.

Iakoubovskii, K. and Adriaenssens, G.J., 2002. Optical characterization of natural Argyle diamonds. Diamond and Related Materials, 11(1): 125-131.

Ickert, R.B., Stachel, T., Stern, R.A. and Harris, J.W., 2013. Diamond from recycled crustal carbon documented by coupled $\delta^{18}O$-$\delta^{13}C$ measurements of diamonds and their inclusions. Earth and Planetary Science Letters, 364: 85-97.

Kiflawi, I., Fisher, D., Kanda, H. and Sittas, G., 1996. The creation of the 3107 cm^{-1} hydrogen absorption peak in synthetic diamond single crystals. Diamond and Related Materials, 5(12): 1516-1518.

Kirkley, M.B., Gurney, J.J., Otter, M.L., Hill, S.J. and Daniels, L.R., 1991. The application of C isotope measurements to the identification of the sources of C in diamonds: a review. Applied Geochemistry, 6(5): 477-494.

Janssen, G., Vollenberg, W., Giling, L.J., Vanenckevort, W.J.P., Schaminee, J.J.D. and Seal, M., 1991. Rapid growth of single-crystal diamond on diamonds substrates. Surface & Coatings Technology, 47(1-3): 113-126.

Javoy, M., 1997. The major volatile elements of the Earth: Their origin, behavior, and fate. Geophysical Research Letters 24(2): 177-180.

Javoy, M. and Pineau, F., 1991. The volatiles record of a "popping" rock from the Mid-Atlantic Ridge at 14°N: chemical and isotopic composition of gas trapped in the vesicles. Earth and Planetary Science Letters, 107(3-4): 598-611.

Javoy, M., Pineau, F. and Delorme, H., 1986. Carbon and nitrogen isotopes in the mantle. Chemical Geology, 57(1-2): 41-62.

Jia, Y., 2006. Nitrogen isotope fractionations during progressive metamorphism: A case study from the Paleozoic Cooma metasedimentary complex,

southeastern Australia. Geochimica et Cosmochimica Acta, 70(20): 5201-5214.

Kiflawi, I., Fisher, D., Kanda, H. and Sittas, G., 1996. The creation of the 3107 cm^{-1} hydrogen absorption peak in synthetic diamond single crystals. Diamond and Related Materials, 5(12): 1516-1518.

Lang, A.R., 1974. Glimpses into the growth history of natural diamonds. Journal of Crystal Growth, 24: 108-115.

Lang, A.R., 1979. Internal Structure. In: J.E. Field (Editor), The Properties of Diamond. Academic Press, London, pp. 425-469.

Leahy, K., and Taylor, W.R., 1997. The influence of the glennie domain deep structure on the diamonds in Saskatchewan kimberlites. Geologiya i Geofizika(2): 451-460.

Li, L., Bebout, G.E. and Idleman, B.D., 2007. Nitrogen concentration and δ15N of altered oceanic crust obtained on ODP Legs 129 and 185: Insights into alteration-related nitrogen enrichment and the nitrogen subduction budget. Geochimica et Cosmochimica Acta, 71(9): 2344-2360.

Luth, R.W., 1993. Diamonds, eclogites, and the oxidation state of the Earth's mantle. Science, 261(5117): 66-70.

Marty, B., 1995. Nitrogen content of the mantle inferred from N2-Ar correlation in oceanic basalts. Nature, 377(6547): 326-329.

Marty, B. and Dauphas, N., 2003. The nitrogen record of crust–mantle interaction and mantle convection from Archean to Present. Earth and Planetary Science Letters, 206(3–4): 397-410.

McCandless, T.E. and Gurney, J.J., 1997. Diamond eclogites: Comparison with carbonaceous chondrites, carbonaceous shales, and microbial carbon-enriched more. Geologiya i Geofizika(2): 371-381.

Melton, G., 2013. Elemental impurities, defects and carbon isotopes in mantle diamond. PhD thesis, University of Alberta.

Mendelssohn, M.J. and Milledge, H.J., 1995. Geologically significant information from routine analysis of the mid-infrared spectra of diamonds. International Geology Review, 37(2): 95-110.

Meyer, H.O.A., 1987. Inclusions in diamond. In: P.H. Nixon (Editor), Mantle xenoliths. John Wiley & Sons Ltd., Chichester, pp. 501-522.

Milledge, H.J., Mendelssohn, M.J., Seal, M., Rouse, J.E., Swart, P.K. and

Pillinger, C.T., 1983. Carbon isotopic variation in spectral Type II diamonds. Nature, 303(5920): 791-792.

Murthy, V.R., 1991. Early Differentiation of the Earth and the Problem of Mantle Siderophile Elements: A New Approach. Science, 253(5017): 303-306.

Nadeau, S., Pineau, F., Javoy, M. and Francis, D., 1990. Carbon concentrations and isotopic ratios in fluid-inclusion-bearing upper-mantle xenoliths along the northwestern margin of North America. Chemical Geology, 81(4): 271-297.

Neilson. S, G.H., Pell. J, Grenon. H, 2012. The Evolution of Kimberlite Indicator Mineral Interpretation on the Chidliak Project, Baffin Island, Nunavut. 10th International Kimberlite Conference, Bangalore, conference CD (abstract 162).

Nimis, P. and Taylor, W.R., 2000. Single clinopyroxene thermobarometry for garnet peridotites. Part I. Calibration and testing of a Cr-in-Cpx barometer and an enstatite-in-Cpx thermometer. Contributions to Mineralogy and Petrology, 139(5): 541-554.

Pell, J., 2008. Technical report on the Chidliak Property, Baffin Region, Nunavut; Peregrine Diamonds, pp. 73.

Pell, J., 2009. 2009 Technical report on the Chidliak Property, Baffin Region, Nunavut; Peregrine Diamonds, pp. 116.

Pell, J., Farrow, D., 2012. Updated 2011 Technical report on the Chidliak Property, Baffin Region, Nunavut; Peregrine Diamonds, pp. 148.

Pell, J., Grütter, H., Dempsey, S. and Neilson, S., 2012. Exploration and discovery of the Chidliak kimberlite province, Baffin Island, Nunavut: Canada's newest diamond district. 10th International Kimberlite Conference, Bangalore, conference CD (abstract 40).

Pell, J., Grütter, H., Neilson, S., Lockhart, G., Dempsey, S. and Grenon, H., 2013. Exploration and Discovery of the Chidliak Kimberlite Province, Baffin Island, Nunavut: Canada's Newest Diamond District. In: D.G. Pearson, H.S. Grütter, J.W. Harris, B.A. Kjarsgaard, H. O'Brien, N.V.C. Rao and S. Sparks (Editors), Proceedings of 10th International Kimberlite Conference. Springer India, Bangalore, India. 209-227.

Peregrine Diamonds Ltd., 2013. Peregrine Provides Chidliak Update and Announces Discovery of Three new Kimberlites.

Peters, K.E., Sweeney, R.E. and Kaplan, I.R., 1978. Correlation of Carbon and

Nitrogen Stable Isotope Ratios in Sedimentary Organic Matter. Limnology and Oceanography, 23(4): 598-604.

Richardson, S.H., 1986. Latter-day origin of diamonds of eclogitic paragenesis. Nature, 322(6080): 623-626.

Richardson, S.H., Erlank, A.J., Harris, J.W. and Hart, S.R., 1990. Eclogitic diamonds of Proterozoic age from cretaceous kimberlites. Nature, 346(6279): 54-56.

Robinson, D.N., Scott, J.A., van Niekerk, A. and Anderson, V.G., 1989. The sequence of events reflected in the diamonds of some southern African kimberlites. In: J. Ross (Editor), Proceedings of the Fourth International Kimberlite Conference, Perth, Australia. Blackwell Scientific, Carlton, Australia, Perth, Australia, pp. 990-1000.

Rondeau, B., Fritsch, E., Guiraud, M., Chalain, J.P. and Notari, F., 2004. Three historical 'asteriated' hydrogen-rich diamonds: Growth history and sector-dependent impurity incorporation. Diamond and Related Materials, 13(9): 1658-1673.

Scott, D.J., 1996. Geology of the Hall Peninsula east of Iqaluit, southern Baffin Island, Northwest Territories. Current Research 1996-C: 83-91.

Sellschop, J.P.F., Madiba, C.C.P. and Annegarn, H.J., 1980. Light volatiles in diamond: Physical interpretation and genetic significance. Nuclear Instruments and Methods, 168(1–3): 529-534.

Sharp, Z., 2007. Principles of stable isotope geochemistry. Pearson Education Upper Saddle River, NJ, USA. p. 344.

Shilobreeva, S., Martinez, I., Busigny, V., Agrinier, P. and Laverne, C., 2011. Insights into C and H storage in the altered oceanic crust: Results from ODP/IODP Hole 1256D. Geochimica et Cosmochimica Acta, 75(9): 2237-2255.

Smart, K.A., Chacko, T., Stachel, T., Muehlenbachs, K., Stern, R.A. and Heaman, L.M., 2011. Diamond growth from oxidized carbon sources beneath the Northern Slave Craton, Canada: A $\delta 13C$–N study of eclogite-hosted diamonds from the Jericho kimberlite. Geochimica et Cosmochimica Acta, 75(20): 6027-6047.

Smith, C.B., Gurney, J.J., Harris, J.W., Otter, M.L., Kirkley, M.B. and Jagoutz, E., 1991. Neodymium and strontium isotope systematics of eclogite and websterite paragenesis inclusions from single diamonds, Finsch and Kimberley Pool, RSA. Geochimica et Cosmochimica Acta, 55(9): 2579-2590.

Smith E, Kopylova M, Frezzotti ML & Afanasiev V., 2013. Mineralogical Magazine, 77(5): 2226.

Snyder, D.B., 2010. Mantle lithosphere structure beneath southeast Baffin Island, Nunavut from teleseismic studies. Geological Survey of Canada, Current Research 2010-8: 6.

St-Onge, M.R., Jackson, G.D. and Henderson, I., 2006. Geology, Baffin Island (south of 70°N and east of 80°W), Nunavut. Geological Survey of Canada, Open File 4931.

St-Onge, M.R., Wodicka, N. and Ijewliw, O., 2007. Polymetamorphic evolution of the trans-hudson orogen, Baffin Island, Canada: Integration of petrological, structural and geochronological data. Journal of Petrology, 48(2): 271-302.

St-Onge, M.R., Scott, D.J. and Wodicka, N., 2001. Terrane boundaries within the Trans-Hudson Orogen (Quebec–Baffin segment), Canada: changing structural and metamorphic character from foreland to hinterland. Precambrian Research,, 107(1-2): 75-91.

Stachel, T., 2007. Diamond. Mineralogical Association of Canada Short Course Series, 37: 1-22.

Stachel, T. and Harris, J.W., 1997. Syngenetic inclusions in diamond from the Birim field (Ghana) - A deep peridotitic profile with a history of depletion and re-enrichment. Contributions to Mineralogy and Petrology, 127(4): 336-352.

Stachel, T. and Harris, J.W., 2008. The origin of cratonic diamonds - Constraints from mineral inclusions. Ore Geology Reviews, 34(1-2): 5-32.

Stachel, T. and Harris, J.W., 2009. Formation of diamond in the Earth's mantle. Journal of Physics Condensed Matter, 21(36).

Stachel, T., Harris, J.W. and Muehlenbachs, K., 2009. Sources of carbon in inclusion bearing diamonds. Lithos, 112: 625-637.

Sobolev, E.V., Lenskaya, S.V. and Lisoivan, V.I., 1969. Lamellar formations in the structure of natural diamonds. Journal of Structural Chemistry, 9(6): 917-920.

Sobolev, V.S., Sobolev, N.V., 1980. New proof on very deep subsidence of eclogitized crustal rocks. Doklady Akademii Nauk SSSR, 250(3): 683-685.

Taylor, W.R., Jaques, A.L. and Ridd, M., 1990. Nitrogen-defect aggregation characteristics of some Australasian diamonds: time-temperature constraints on the source regions of pipe and alluvial diamonds. American Mineralogist, 75(11-12): 1290-1310.

Thomassot, E., Cartigny, P., Harris, J.W. and Viljoen, K.S., 2007. Methane-related diamond crystallization in the Earth's mantle: Stable isotope evidences from a single diamond-bearing xenolith. Earth and Planetary Science Letters, 257(3-4): 362-371.

Titus, E., Misra, D.S., Sikder, A.K., Tyagi, P.K., Singh, M.K., Misra, A., Ali, N., Cabral, G., Neto, V.F. and Gracio, J., 2005. Quantitative analysis of hydrogen in chemical vapor deposited diamond films. Diamond and Related Materials, 14(3-7): 476-481.

Walmsley, J.C., Lang, A.R., Rooney, M.L.T. and Welbourn, C.M., 1987. Newly observed microscopic planar defects on {111} in natural diamond. Philosophical Magazine Letters, 55: 209-213.

Watenphul, A., Wunder, B., Heinrich, W., 2009. High-pressure ammonium-bearing silicates: Implications for nitrogen and hydrogen storage in the Earth's mantle. American Mineralogist, 94(2-3): 283-292.

Watenphul, A., Wunder, B., Wirth, R., Heinrich, W., 2010. Ammonium-bearing clinopyroxene: A potential nitrogen reservoir in the Earth's mantle. Chemical Geology, 270(1-4): 240-248.

Weiss, Y., Kessel, R., Griffin, W.L., Kiflawi, I., Klein-BenDavid, O., Bell, D.R., Harris, J.W. and Navon, O., 2009. A new model for the evolution of diamond-forming fluids: Evidence from microinclusion-bearing diamonds from Kankan, Guinea. Lithos, 112: 660-674.

Weiss, Y., Kiflawi, I. and Navon, O., 2010. IR spectroscopy: Quantitative determination of the mineralogy and bulk composition of fluid microinclusions in diamonds. Chemical Geology, 275(1-2): 26-34.

Welbourn, C.M., Rooney, M.-L.T. and Evans, D.J.F., 1989. A study of diamonds of cube and cube-related shape from the Jwaneng mine. Journal of Crystal Growth, 94(1): 229-252.

Whalen, J.B., Wodicka, N., Taylor, B.E. and Jackson,G.D., 2010. Cumberland batholiths, Trans-Hudson Orogen, Canada: petrogenesis and implications for Paleoproterozoic crustal and orogenic processes. Lithos, 117: 99-118.

Wilks, J. and Wilks, E., 1991. Properties and applications of diamond. Butterworth-Heinemann, Oxford, UK, 525 pp.

Woods, G.S., 1986. Platelets and the infrared absorption of type Ia diamonds. Proceedings of the Royal Society of London, Series A, Mathematical and Physical Sciences 407(1832): 219-238.

Woods, G.S. and Collins, A.T., 1983. Infrared absorption spectra of hydrogen complexes in type I diamonds. Journal of Physics and Chemistry of Solids, 44(5): 471-475.

Wyllie, P.J., Huang, W.L., Otto, J. and Byrnes, A.P., 1983. Carbonation of peridotites and decarbonation of siliceous dolomites represented in the system $CaO-MgO-SiO_2-CO_2$ to 30 kbar. Tectonophysics, 100(1-3): 359-388.

Chapter 5: Conclusions

The Chidliak diamonds are hosted by kimberlites emplaced into Archean ortho- and para-gneisses on the Hall Peninsula block. To date, there are 67 kimberlite discoveries, and a 508 tonne bulk sample from kimberlite CH-6 will be processed later this year to provide a preliminary revenue model and establish an initial resource for kimberlite CH-6 (Peregrine Diamonds Ltd, 2013).

The majority of Chidliak diamonds are colorless, followed by yellow and brown diamonds, indicating the presence of nitrogen impurities (likely N2 centres formed as by-products of A to B centre aggregation) for the yellow diamonds and plastic deformation for the brown diamonds. Many of the diamonds are irregular; octahedra and octahedral fragments, and cuboids and cuboid fragments are also present in the Chidliak diamond suite but are less abundant.

Reconstructing the sequence of events from diamond genesis to emplacement is achieved by combining the observed surface features with internal growth structures imaged by CL, coupled with carbon isotopic compositions of the growth layers. Two stages of distinct growth are evident; after initial diamond growth from a distinct fluid with ^{13}C depleted carbon and low nitrogen contents, resorption occurred, followed by another distinct diamond precipitation event. δ^{13}C values and nitrogen contents vary across some growth layers, suggesting growth from multiple pulses of fluids. This second diamond growth event generated complex CL patterns, with instances of homogeneous growth, agate-like banded growth, octahedral, cuboid, and mixed habit growth. Plastic deformation postdates the growth events as the plastic deformation lines are seen cross cutting these growth structures. Evidence from platelet degradation

122

suggests that an elevated strain event affected some of the Chidliak diamonds, and possibly coincided with the plastic deformation event. Diamond breakage within the mantle may have also occurred concurrently with this elevated strain event.

Many of the Chidliak diamonds show signs of resorption. Low temperature etch features such as positive trigons and hexagons are present on some diamond surfaces, with high temperature etch features such as negative trigons postdating the formation of the low temperature etching. The majority of hillocks observed are drop shaped, while few are pyramidal, indicating progressive resorption from pyramidal to drop shaped hillocks (Tappert and Tappert, 2011). Late stage etch features are present on a few diamonds, exhibiting rough surfaces, micro-disk patterns or pits. Some diamonds broke during kimberlite ascent, and breakage surfaces were subsequently etched and/or resorbed. Since the studied diamonds are small (≤850 µm), resorption features may be more prominent than those on macro-diamonds (not studied). Due to their high surface area to mass ratio, some of these smaller diamonds may also have been completely removed from the diamond population by resorption, if they were released from xenoliths/xenocrysts early on during kimberlite eruption.

Nitrogen aggregation state and content relationships show that Chidliak diamonds resided in a relatively cool mantle between ~980-1350°C (corresponding to ~150-200 km depth), with 96% of analysed diamonds residing at apparent temperatures of 1000-1150°C. Only three diamonds reside at temperatures greater than 1200°C; this may suggest that the Chidliak kimberlites preferentially sampled diamonds from shallow diamond stable lithosphere (main

temperature range). Another possible explanation is that the subcratonic lithospheric mantle beneath Chidliak was heterogeneous and the conditions of diamond formation were not favourable at higher temperatures.

The Chidliak diamonds are both hydrogen and nitrogen rich which indicates that the growth environment was also rich in hydrogen and nitrogen. Many diamonds contain hydrogen impurity peaks at 3107 cm^{-1}, and it is shown that there is a relationship for Chidliak diamonds between IR-active hydrogen centres and the aggregation state (%B) of nitrogen. The hydrogen found in some Chidliak diamonds is considerably higher than the previously defined envelope of worldwide data from Melton (2013).

The δ^{13}C values of Chidliak diamonds range from -28.6 to -1.3‰ with a primary mode about -6‰ and a second minor mode about -15‰. A range in δ^{15}N of -5.9 to +18.7‰ is observed with a mode about -3‰ and secondary modes at +3‰ and +6‰. The δ^{13}C distribution and the overall high nitrogen contents (28 diamonds >1500 at. ppm) of the Chidliak diamond suite matches the distributions of eclogitic diamonds from worldwide sources and other Canadian deposits. The relationship between carbon isotopic composition and nitrogen content for the entire diamond suite is such that as carbon approaches ^{13}C-depleted values, total nitrogen content decreases as well. δ^{13}C values down to -28.6‰ cannot be related to fractionation of a primary mantle fluid as unrealistically high levels of fractionation would be required. Therefore, a source other than primary mantle carbon must have been introduced to the system to account for the very negative δ^{13}C values. The presence of both strongly ^{13}C depleted diamonds (δ^{13}C -22 to -

29‰) and diamonds with positive $\delta^{15}N$ values (usually not the same samples) likely reflects a contribution of subducted oceanic crust (former organic matter could deliver ^{13}C-depleted carbon whilst ammonium in clay minerals provides a subductable nitrogen component with positive $\delta^{15}N$) to diamond genesis beneath Chidliak. Diamond formation may have occurred during infiltration of mantle derived fluids/melts that mixed with carbon present in the eclogitic diamond source (recycled organic matter and primary MORB carbon). Sub-parallel trends between total nitrogen content and $\delta^{15}N$ reflect an additional mixing relationship involving the mantle fluids/melts discussed above and a subducted sedimentary component, without affecting carbon isotopic compositions. The complete decoupling of carbon and nitrogen isotopic compositions suggests that the fluid/melt carrying the sedimentary nitrogen component did not transport significant carbon.

Although assigning a source paragenesis in the absence of mineral inclusion data has to be viewed with some caution, based on the strong similarity with diamonds from other deposits containing eclogitic inclusions it seems very probable that Chidliak diamonds mainly derive from eclogitic sources.

References:

Melton, G., 2013. Elemental impurities, defects and carbon isotopes in mantle diamond. PhD thesis, University of Alberta.

Peregrine Diamonds., Sept 9, 2013. Peregrine Provides Chidliak Update and Announces Discovery of Three New Kimberlites.

Tappert, R. and Tappert, M.C., 2011. Diamonds in Nature: A Guide to Rough Diamonds. Springer Heildelberg Dordrecht, London New York.

Appendix A: Methods

A.1 Introduction:

Initially diamonds for the two sampled kimberlites pipes were separated from the kimberlite by SRC Geoanalytical Laboratories of Saskatoon, Saskatchewan, using non diamond-destructive caustic fusion. The diamonds were then sorted into sieve sizes (850-600 μm, 600-425 μm, 425-300 μm, 300-212 μm, 212-150 μm, 150-106 μm). Diamonds were placed onto sticky tape protected with a plastic slide and a second layer of sticky tape. The 210 diamonds were chosen based on size, the larger diamonds were selected first, with diamond selection progressing down to the 212 μm size fraction.

A.2 Physical Characterization of Chidliak Diamonds:

Diamond physical characterization is carried out using a binocular microscope, following the guidelines and terminology of McCandless et al. (1994) and Robinson (1979), while adhering to rules from Harris et al. (1975). Magnification used to identify surface features was typically 80x, for the larger diamonds 32x-80x magnification was used. Diamonds are characterized based on shape, surface features, color, breakage and extent of resorption. Other diamond classification schemes and observations were considered, (e.g., Orlov, 1977; Gurney, 1989; Tappert and Tappert, 2011), but not utilized for this study. Diamonds were photographed then cleaned with acetone in an ultrasonic bath for 15-20 minutes to remove any sticky tape residue and surface contamination prior to weighing and geochemical analysis.

A.3 Fourier Transform Infrared (FTIR) Spectrometry:

After cleaning, diamonds were mounted on the side of a glass slide with double sided carbon tape; up to 14 diamonds were mounted at once and analysed in sequential order. This allowed for efficient measurement and easy maneuvering under the infrared microscope to align the diamonds with the IR laser.

Determination of nitrogen concentrations and aggregation states were carried out using a Thermo Scientific Nicolet FTIR spectrometer coupled with a Nicolet Continuum infrared microscope at the University of Alberta. Background measurements were taken at the beginning of the session and at regular intervals throughout the day (no longer than 2 hours between new background measurements). The system was filled with liquid nitrogen, and then periodically topped up throughout the session to maintain a stable environment during analyses. When possible 2-3 spots were analysed for each diamond to identify intra-diamond variation in nitrogen contents and aggregation state, but in some instances only one spot was analysed.

Spectra were collected in transmittance mode for 200 scans, for a range of wave numbers from 650 to 4000 cm^{-1} with a spectral resolution of 4 cm^{-1}. Each sample spectrum was background and baseline corrected; baseline correcting is done consistently for all diamond samples with minimal manipulation of the spectra. In most cases, the spectra were zeroed at 650, 1500, and 4000 cm^{-1}. The diamond sample spectra were then normalized by subtracting an analyzed pure Type II diamond standard of 1 cm thickness from the sample spectrum. This diamond standard is baseline corrected and converted to absorption coefficients

through normalization of the absorbance at 1995 cm^{-1} to 11.94 cm^{-1}. The sample

spectra were deconvoluted into A, B and D components using software provided

by David Fisher (Research Laboratories of the Diamond Trading Company,

Maidenhead UK). This determines the nitrogen content and the aggregation state

for the unknown diamond samples. Concentrations of nitrogen, in atomic ppm (at.

ppm), are calculated using absorption coefficient values at 1282 cm^{-1} using the

factors derived by Boyd et al. (1994) for the A centres and Boyd et al. (1995) for

the B-centres. Limits of detection strongly depend on the quality of the diamond,

but are generally in the range of 5-15 at. ppm, with errors typically in the range of

5 to 10% of total nitrogen concentration.

Where present in the spectra, the intensities of the platelet peak and the

hydrogen related peak at 3107 cm^{-1} were quantified by integrating the peak area

using the OMNIC software. The peak intensity measurements were taken after the

spectra were baseline corrected and normalized to the 1 cm thickness. The peak

area measurement involved fitting of a local background to eliminate diamond

and nitrogen related absorbance. For the Chidliak diamonds the hydrogen peak at

3107 cm^{-1} is broadly linearly related to the hydrogen peak at 3236 cm^{-1} (Figure

A.3.1)
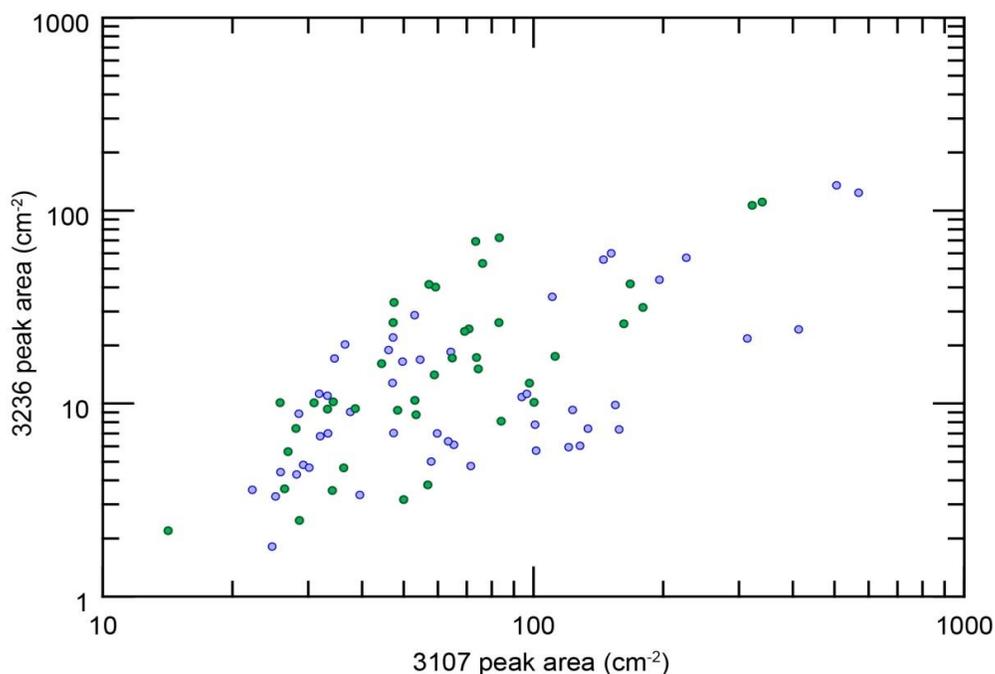
Figure A.3.1. A broadly linear relationship is observed between hydrogen peaks at 3236 cm^{-1} and 3107 cm^{-1} for Chidliak diamonds.

A.4 Scanning Electron Microscope (SEM):

Using a JEOL 6301F SEM a small subset of 12 diamonds in the size range

of 850-300 μm were imaged by secondary electron imaging with an accelerating

voltage of 5 kV and a resolution of approximately 3 nm. Cleaned diamond

samples were mounted on double sided carbon tape on brass holders and coated

with a thin layer of gold using the Xenosput XE200 prior to imaging.

A.5 Secondary Ion Mass Spectrometry (SIMS):

Ninety four diamonds were analyzed for their carbon isotopic

composition, nitrogen concentration, and nitrogen isotopic composition using

secondary ion mass spectrometry (SIMS) on a Cameca IMS1280 ion microprobe

at the Canadian Centre for Isotopic Microanalysis (CCIM) at the University of

Alberta. SIMS is a near surface, is situ analytical method, based on bombarding a

sample with a primary ion beam that causes secondary ions to sputter off the

sample surface. Sputtering is conducted at high spatial resolution, in the current study a spot size of 15μm was utilized. A mass spectrometer is then used to measure the isotopic composition of the secondary ions.

For sample preparation, the diamonds were placed on double sided thermal tape according to size and then embedded in epoxy. Three epoxy mounts were made, two of which were polished with a 30 μm diamond pad by hand to expose as much of the diamonds as possible. This was followed by two steps of polishing with 15 μm and then a 6 μm diamond pads. The third mount was polished following the same procedure as described above, but with an additional step; the mount was polished for 30 minutes on a lapping pad embedded with 3 μm diamond. Each mount was then coated with a thin layer of epoxy that was subsequently removed from the diamond surfaces using a 1 μm aluminum oxide pad. The mounts were then coated with 5 nm of gold.

The internal growth structures of the Chidliak diamonds were imaged with cathodoluminescence (CL) using a Zeiss EVO 15 scanning electron microscope equipped with both Gatan Chroma and Robinson wide spectrum CL detectors at CCIM.

Following CL imaging, the epoxy mounts were cored out and combined into two mounts with standards prior to SIMS analyses. These mounts were pressed into indium with three standards in each mount, and were subsequently coated with 30 nm of gold to ensure conductivity for analysis. Standards used include: S0233A4, S0233A8, S0011Cd, S0233A1, S0233A3, S0011Bd and S0270J. CCIM standards S0011B and S0011C derive from a single isotopically

homogeneous section through a {100} growth sector of a synthetic diamond

provided through David Fisher, The Diamond Trading Company, Maidenhead,

UK. Calibration using the synthetic diamond standard was carried out prior to

setting points on the unknown diamond samples. After $\delta^{13}C$ and nitrogen content

analyses the standards were removed from the mounts. For $\delta^{15}N$ determination the

three mounts were cored out and combined into a single mount with a single

standard (S0270J). This new mount was re-coated with 30 nm of gold to ensure

conductivity for analysis.

The points to be analysed were set and saved as a chain prior to running

the SIMS analyses. Each spot was checked against the CL images and a small

spot was burned onto the diamond surface to ensure correct spot location in

regards to internal growth structures. The primary beam spot on the diamond was

photographed and saved after each analysis.

A.5.1 Conditions for Determining $\delta^{13}C$:

The carbon isotopic composition was determined in multi-collection mode

using 2 Faraday cups for 5 s per count cycle, with 15 cycles per analytical spot

with approximately 4 minutes between spot measurements. Pre-sputtering for 30 s

per spot cleaned the area to be analysed of any possible contamination. The Cs^+

primary beam was used with an impact energy of 20 kV, a mass resolution of

~2300 and a range of primary beam current of 3.2-4.2 nA. The primary standard

used is S0011Cd, the secondary standard is S0011Bd, the tertiary standard is

S0233A8, and the quaternary standard used is S0233A1; standard S0233A8 was

used to track drift throughout the session. The synthetic diamond standard was

analyzed after every four analyses of unknowns, and the values for the diamond samples were corrected to account for instrumental drift. The standard error (2σ) for individual point analyses ranged from 0.20‰ to 0.22‰. The synthetic diamond standards used have $\delta^{13}C$ (VPDB) values of -22.78‰ which corresponds to a $^{13}C/^{12}C$ ratio of 0.010925320.

A.5.2 Conditions for Determining Nitrogen Concentration:

Nitrogen concentration was determined in multi-collection mode using 2 Faraday cups, or for samples with low count rates the electron multiplier was utilized. The cut off for low count rates of $<1\times10^5$ counts/sec was used to determine which collection mode would be used. An electron multiplier was used for nitrogen analysis of samples yielding low count rates (cts/sec). ^{12}C-^{14}N ions and ^{12}C-^{12}C ions, were simultaneously collected, from which total nitrogen concentration was calculated in at. ppm. The primary standard used was, S0233A1, the secondary standard was S0011Bd, the tertiary standard was S0233A8 and the quaternary standard used was S0011Cd. The Cs^+ primary beam was used with an impact energy of 20 kV and a mass resolution of 7000. For analyses collected using the Faraday cup the pre-sputtering time per spot prior to analysis was 60 s, followed by 10 cycles with 5 s per cycle per analytical spot; when using the electron multiplier the pre-sputtering time is 120 s followed by 15 cycles of 5 s per cycle per analytical spot. The synthetic diamond standard was measured after every 10 analyses of unknowns, the standard has a value of 270 ppm for nitrogen concentration. The time between measuring spots ranged from

4.5 min to 4.75 min depending on the detector used. The 2σ error for nitrogen concentration for the unknowns is $\pm 10\%$.

A.5.3 Conditions for Determining $\delta^{15}N$:

The nitrogen isotopic composition was determined in multi-collection mode using Faraday cups for 5 s per count cycle, with 50 cycles per analytical spot with approximately 7.25 min between spot measurements. Four unknown analytical spots were measured between measurements of the standard. The Cs^+ primary beam was used with an impact energy of 20 kV, and a primary beam current range of 2.5-4 nA. The Faraday cup was used to measure the ^{12}C-^{14}N ions with a mass resolution of 6700, while the electron multiplier was used to measure the ^{12}C-^{15}N ions with a mass resolution of 7100. These ratios were converted into $^{15}N/^{14}N$ ratios and then into $\delta^{15}N$ values. The 2σ errors for the unknown diamond samples range from 0.55 to 4.38‰. The standard material used was S0270J with a $\delta^{15}N$ value of -0.5‰.

Sample ID	SIMS ID	Sample ID	SIMS ID	Sample ID	SIMS ID
CH6-1	S1989	CH6-35	S2024	CH5-19	S2059
CH6-2	S1990	CH6-37	S2025	CH5-20	S2060
CH6-3	S1991	CH6-38	S2026	CH5-21	S2061
CH6-4	S1992	CH6-39	S2027	CH5-22	S2062
CH6-5	S1993	CH6-40	S2028	CH5-23	S2063
CH6-6	S1994	CH6-42	S2030	CH5-24	S2064
CH6-7	S1995	CH6-43	S2031	CH5-26	S2066
CH6-8	S1996	CH6-45	S2033	CH5-25	S2065
CH6-9	S1997	CH6-46	S2034	CH5-27	S2067
CH6-10	S1998	CH6-47	S2035	CH5-28	S2068
CH6-11	S1999	CH6-48	S2036	CH5-30	S2069
CH6-12	S2000	CH6-49	S2037	CH5-31	S2070
CH6-13	S2001	CH6-50	S2038	CH5-32	S2071
CH6-14	S2002	CH6-51	S2039	CH5-33	S2072
CH6-15	S2003	CH5-1	S2040	CH5-34	S2073
CH6-16	S2004	CH5-2	S2041	CH5-35	S2074
CH6-17	S2005	CH5-3	S2042	CH5-36	S2075
CH6-18	S2006	CH5-4	S2043B	CH5-37	S2076
CH6-19	S2007	CH5-5	S2045	CH5-38	S2077
CH6-20	S2008	CH5-6	S2046	CH5-39	S2078
CH6-21	S2009	CH5-7	S2047	CH5-40	S2079
CH6-22	S2010	CH5-8	S2048	CH5-42	S2081
CH6-23	S2011	CH5-9	S2049	CH5-43	S2082
CH6-24	S2012	CH5-10	S2050	CH5-44	S2083
CH6-26	S2014	CH5-11	S2051	CH5-45	S2084
CH6-27	S2015	CH5-12	S2052	CH5-46	S2085
CH6-28	S2016	CH5-13	S2053	CH5-47	S2086
CH6-29	S2017	CH5-15	S2055	CH5-48	S2087
CH6-30	S2018	CH5-16	S2056	CH5-49	S2088
CH6-32	S2020A	CH5-17	S2057	CH5-50	S2089
CH6-33	S2022	CH5-18	S2058	CH5-51	S2090
CH6-34	S2023				

Table A.1. Chidliak sample ID and SIMS ID conversion

References:

Boyd, S.R., Kiflawi, I. and Woods, G.S., 1994. The Relationship between infrared-absorption and the A defect concentration in diamond. Philosophical Magazine B-Physics of Condensed Matter Statistical Mechanics Electronic Optical and Magnetic Properties, 69(6): 1149-1153.

Boyd, S.R., Kiflawi, I. and Woods, G.S., 1995. Infrared-absorption by the B-nitrogen aggregate in diamond. Philosophical Magazine B-Physics of Condensed Matter Statistical Mechanics Electronic Optical and Magnetic Properties, 72(3): 351-361.

Appendix B: Diamond Photographs

B.1 Diamond Colors:
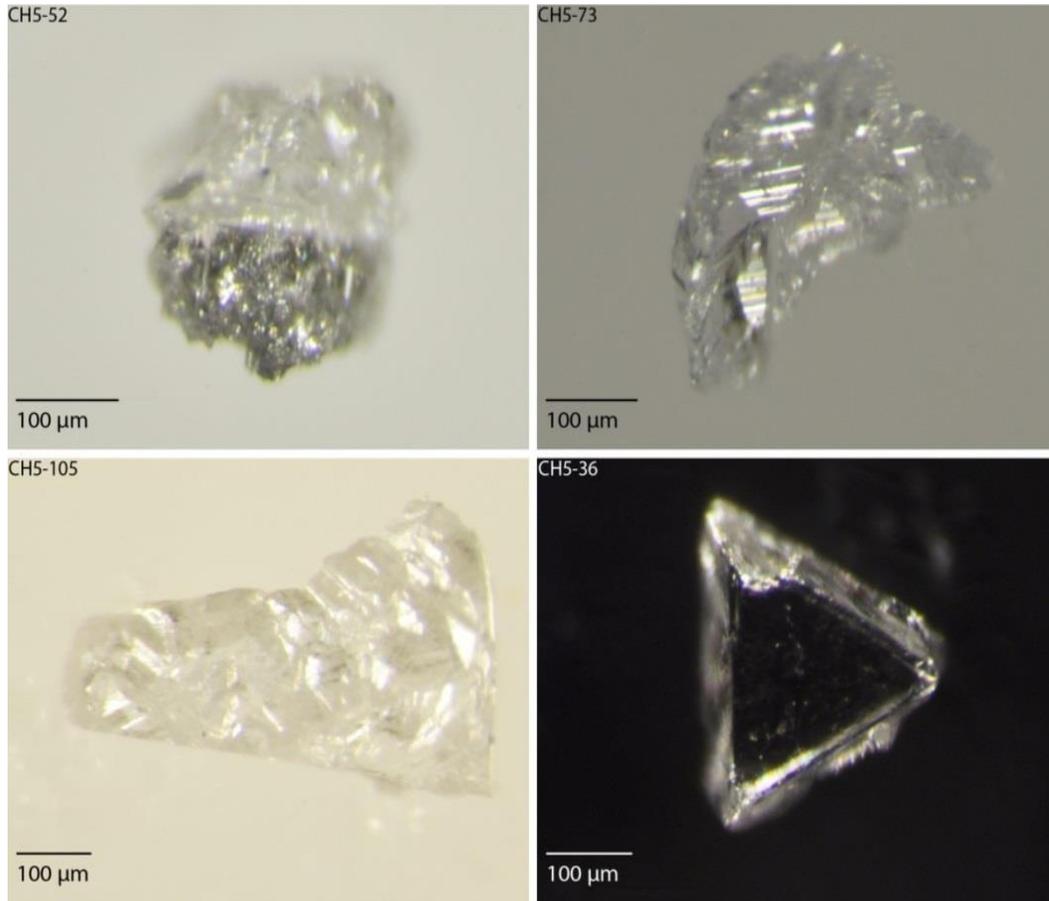
Figure B.1.1. Examples of colorless diamonds. Diamond CH5-52 is half colorless, half grey
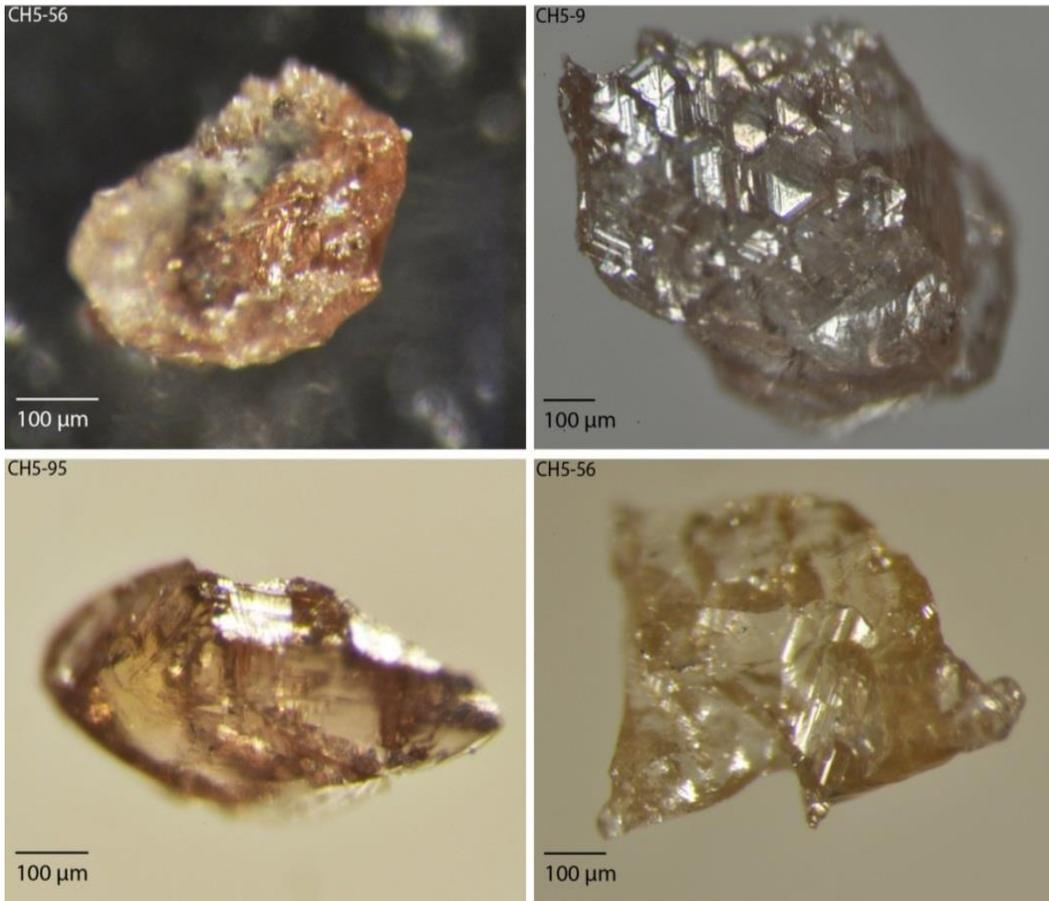
Figure B.1.2. Diamonds showing the range in brown coloration from light to dark brown. Diamond CH5-9 is partly grey (upper left portion of diamond).
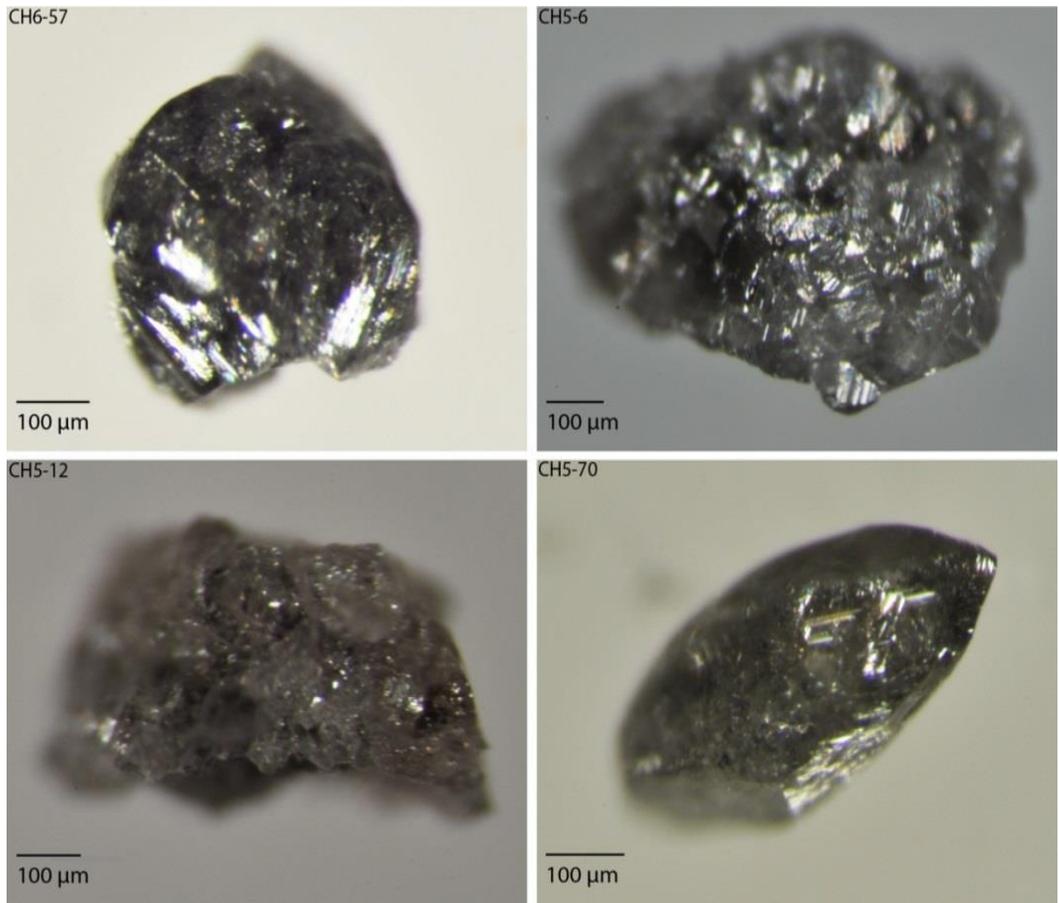
Figure B.1.3. Examples of grey diamonds.
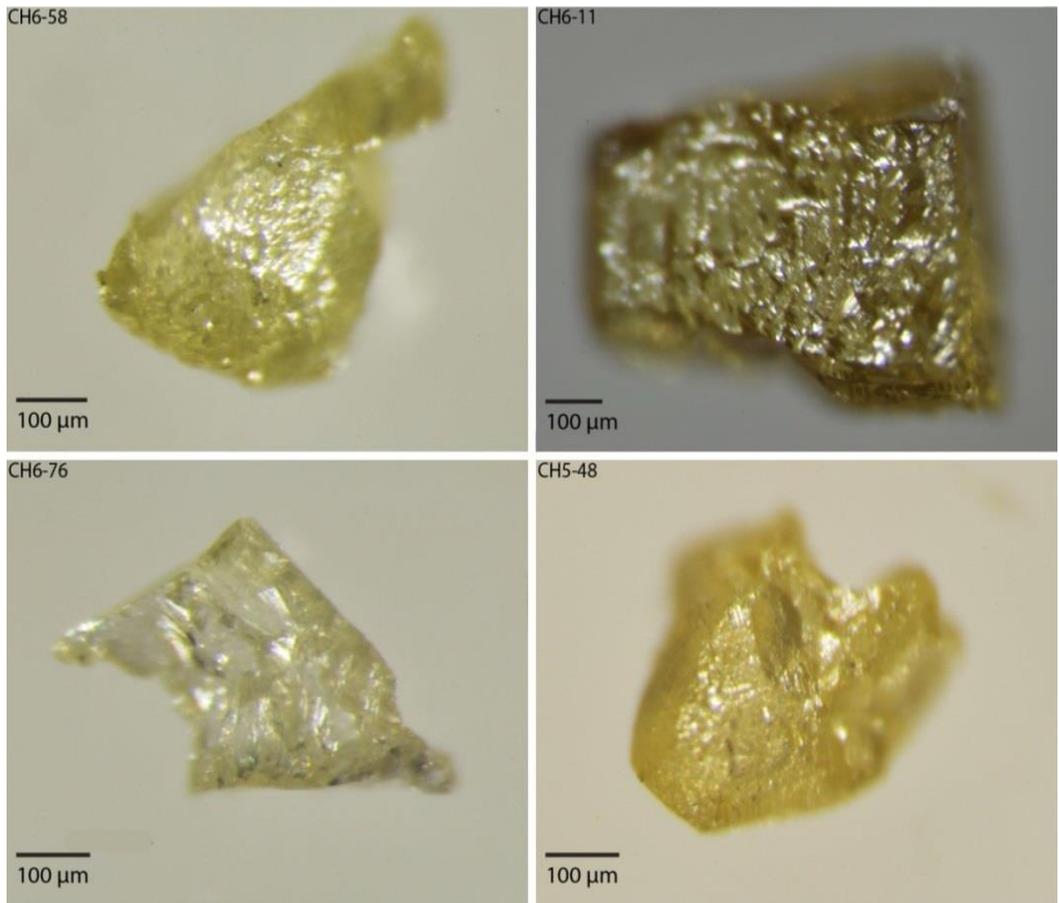
Figure B.1.4. Diamonds showing the range in yellow coloration from light yellow to dark yellow.
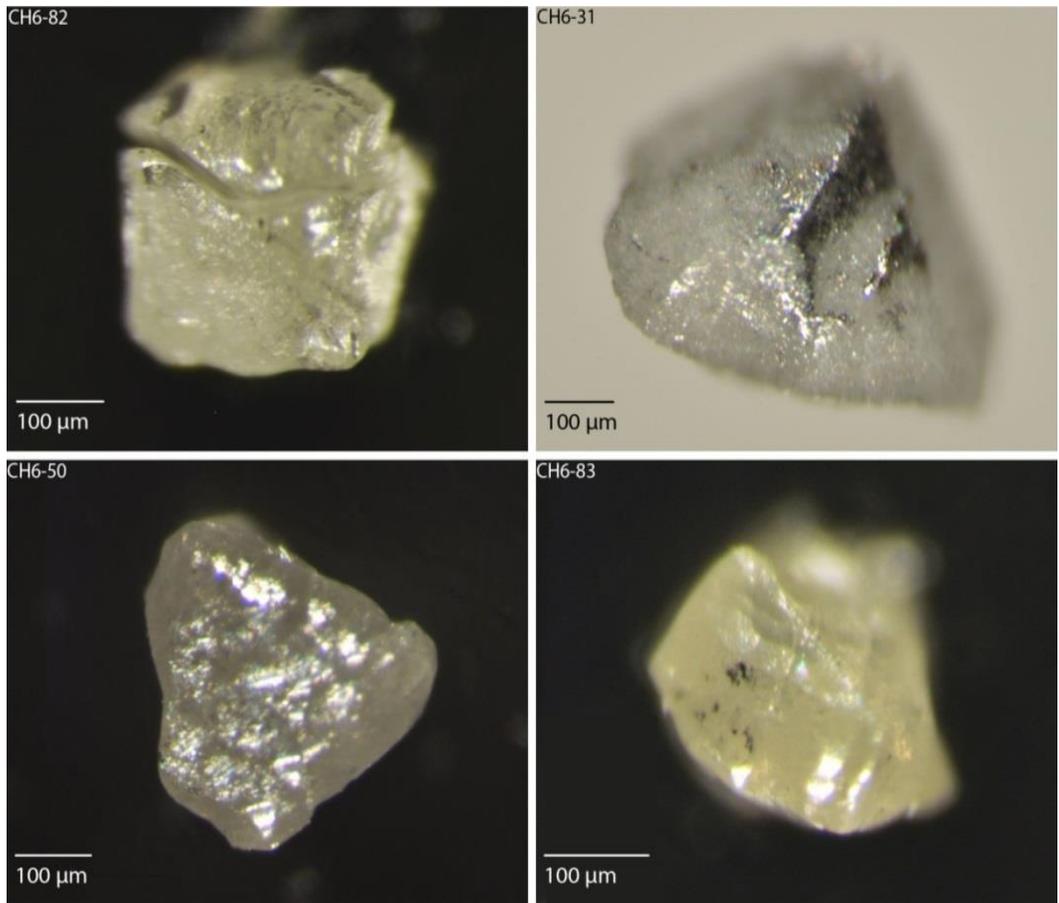
Figure B.1.5. Examples of opaque/cloudy diamonds; cloudy grey (CH6-82), cloudy grey-opaque (CH6-31) grey (CH6-50), and cloudy green-grey (CH6-83).

B.2 Diamond Shapes:
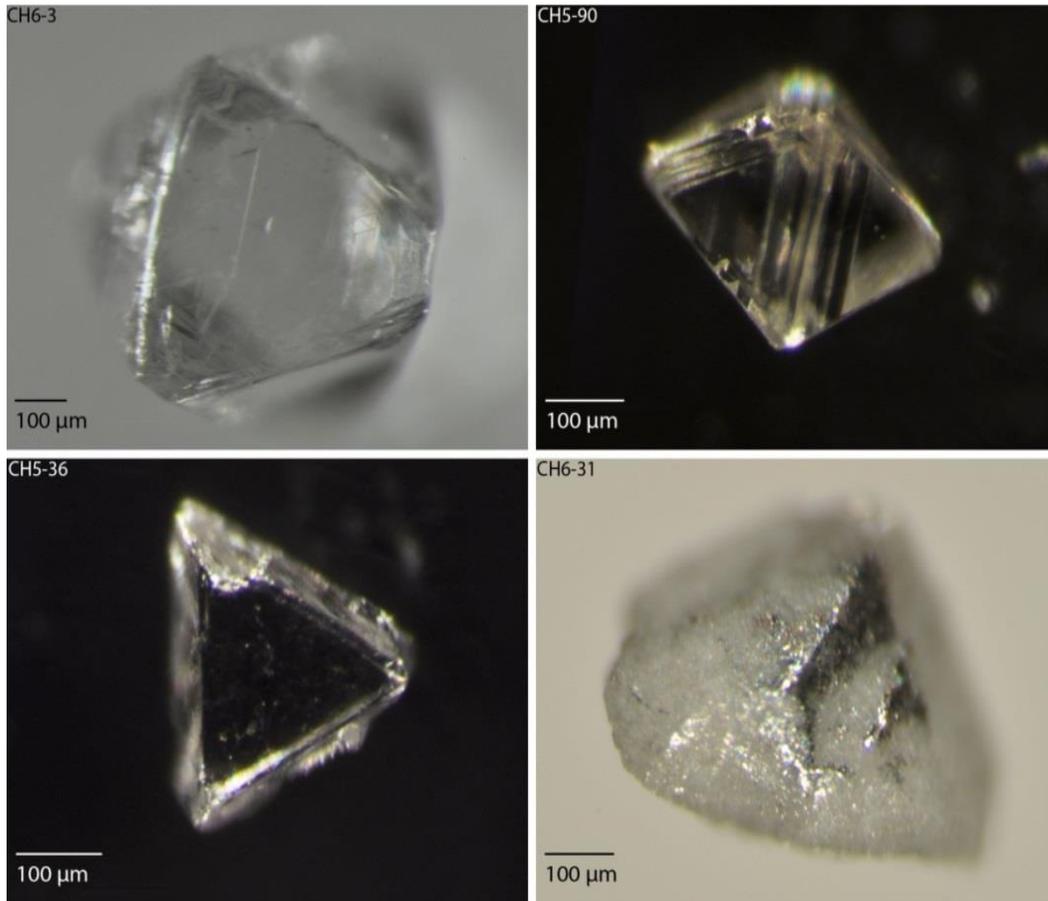
Figure B.2.1. Examples of octahedral diamonds, including two macles (CH6-36; CH6-31). Diamond CH6-31 is opaque and has a partial graphite coating, diamond CH6-3 has truncated corners.
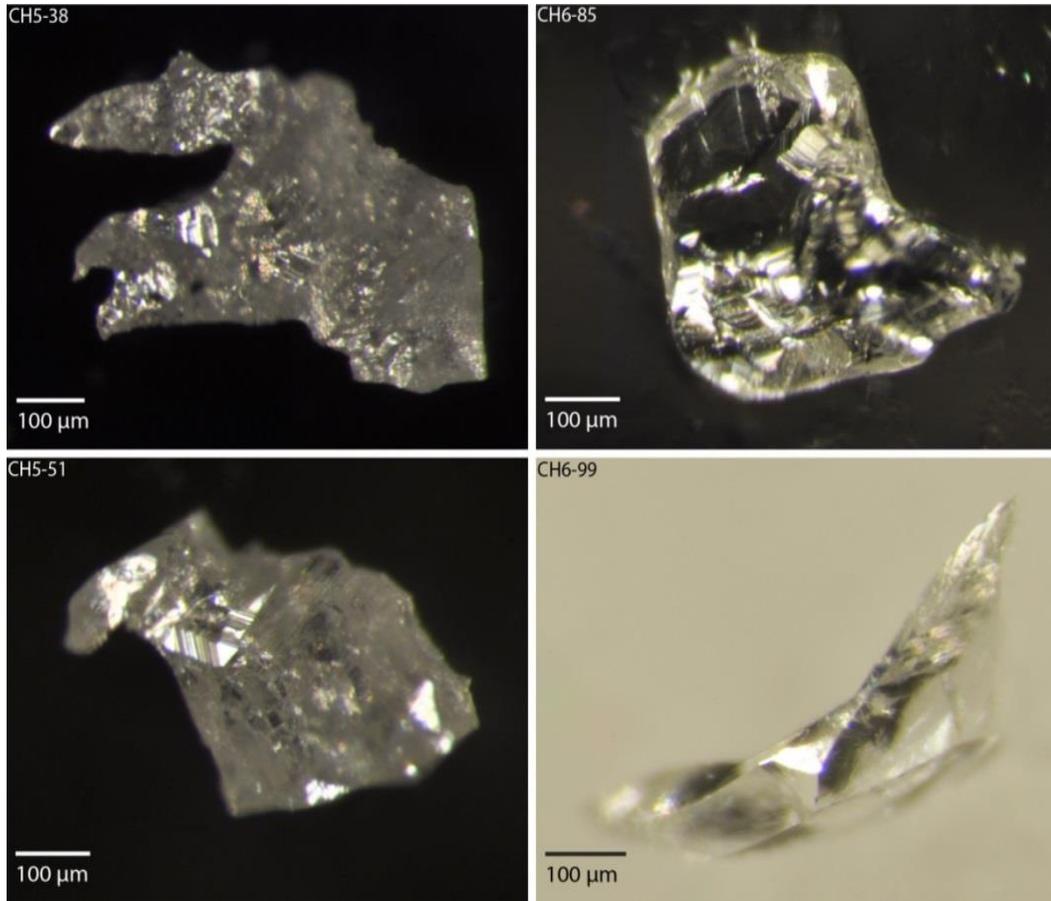
Figure B.2.2. Examples of irregular diamonds. Diamonds are characterized as irregular, when over 50% of the original stone has been removed, with no distinct primary faces but surface features may still be present (ex. trigon on CH5-51).
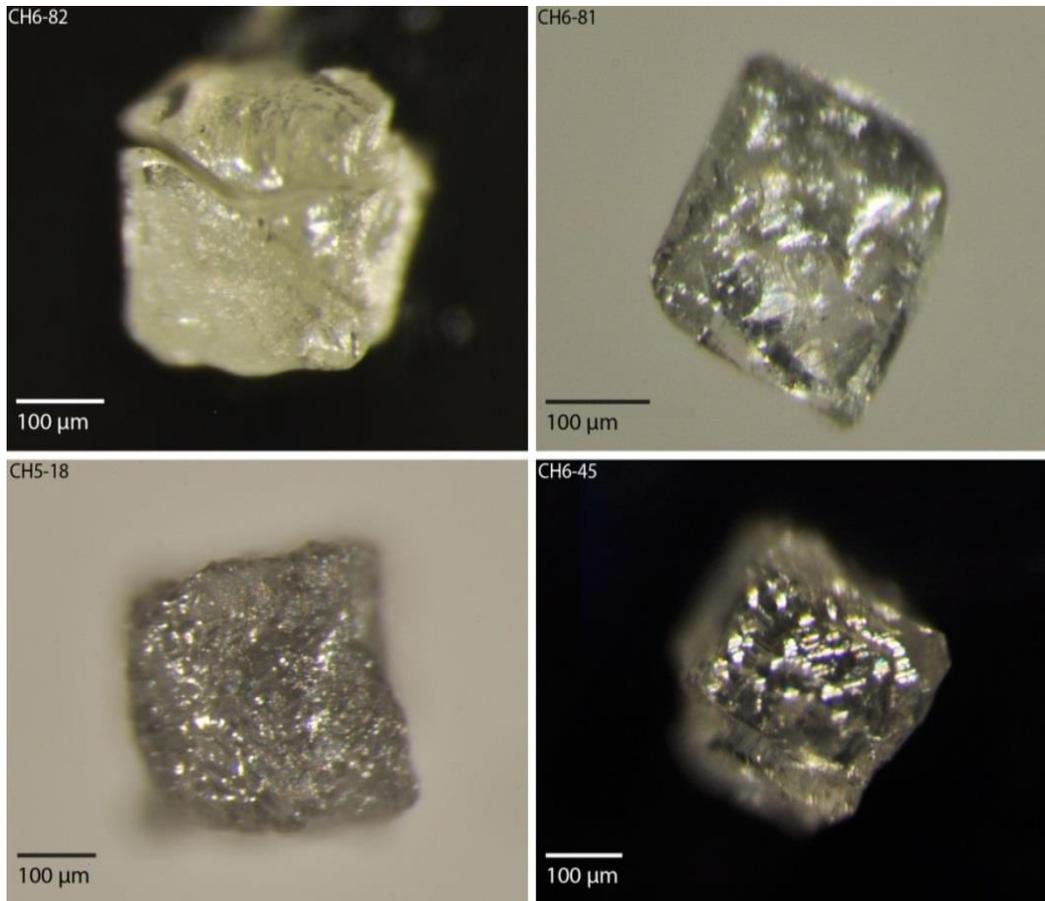
Figure B.2.3. Examples of cuboid diamonds. CH6-82 has multiple ruts and rounded edges. The surface of CH5-18 appears rough but is covered in small negative tetragons. CH6-45 shows stepped growth with the middle portion of the face raised relative to the edges.
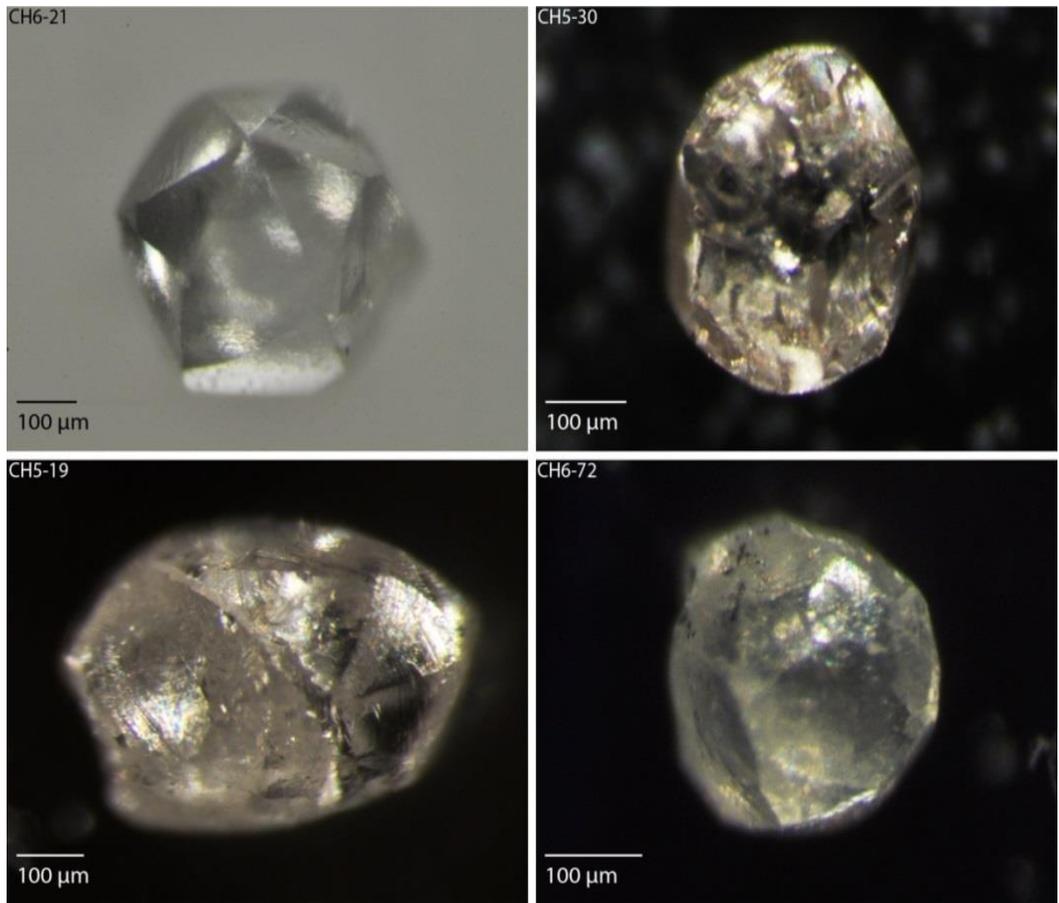
Figure B.2.4. Examples of dodecahedral diamonds.
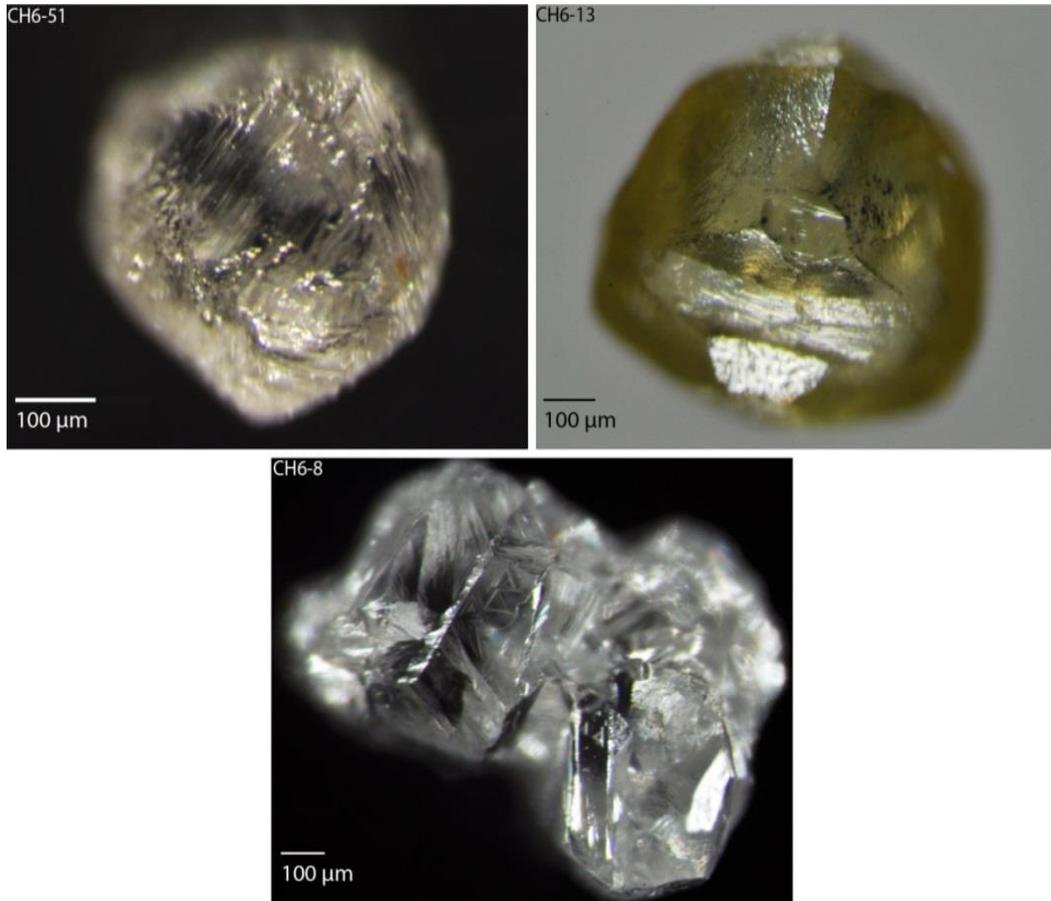
Figure B.2.5. Examples of do shape (CH6-51), od shape (CH6-13) and an aggregate showing signs of resorption (CH6-8).

B.3 Diamond Surface Features:
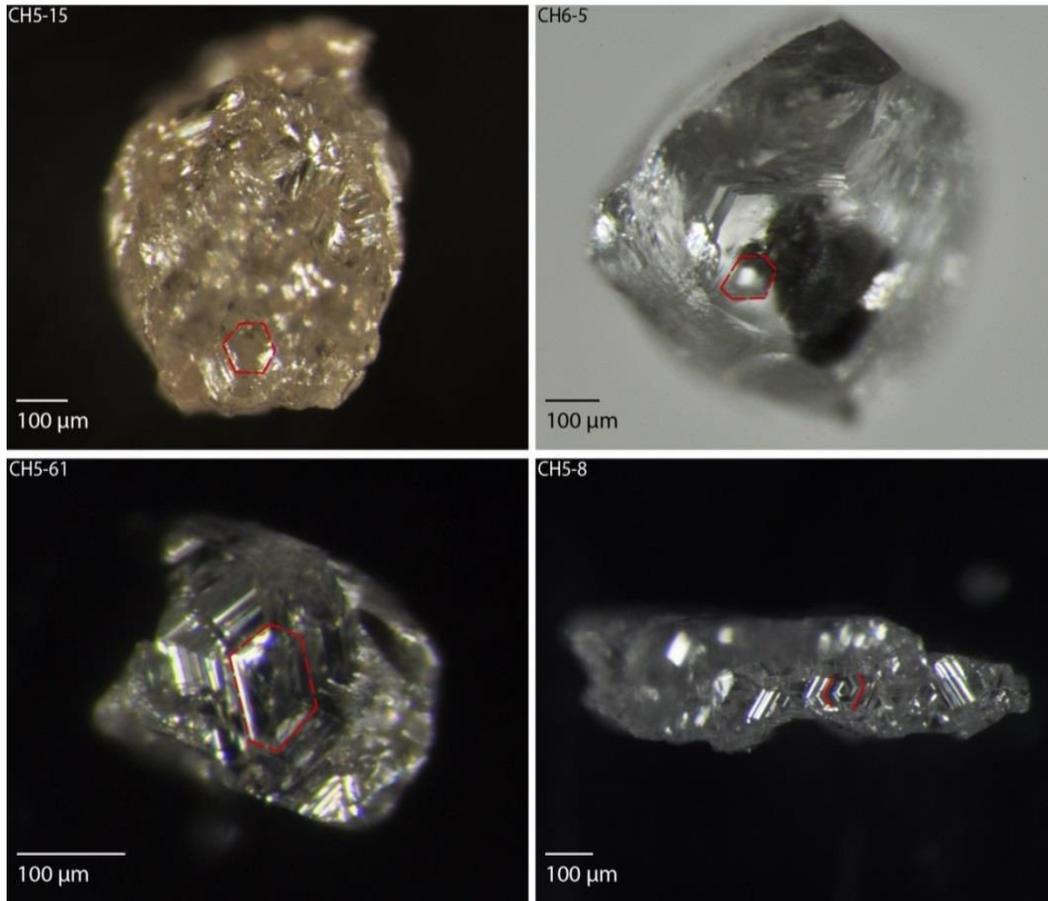
Figure B.3.1. Examples of hexagons or partial hexagons (outlined with a red dashed line).
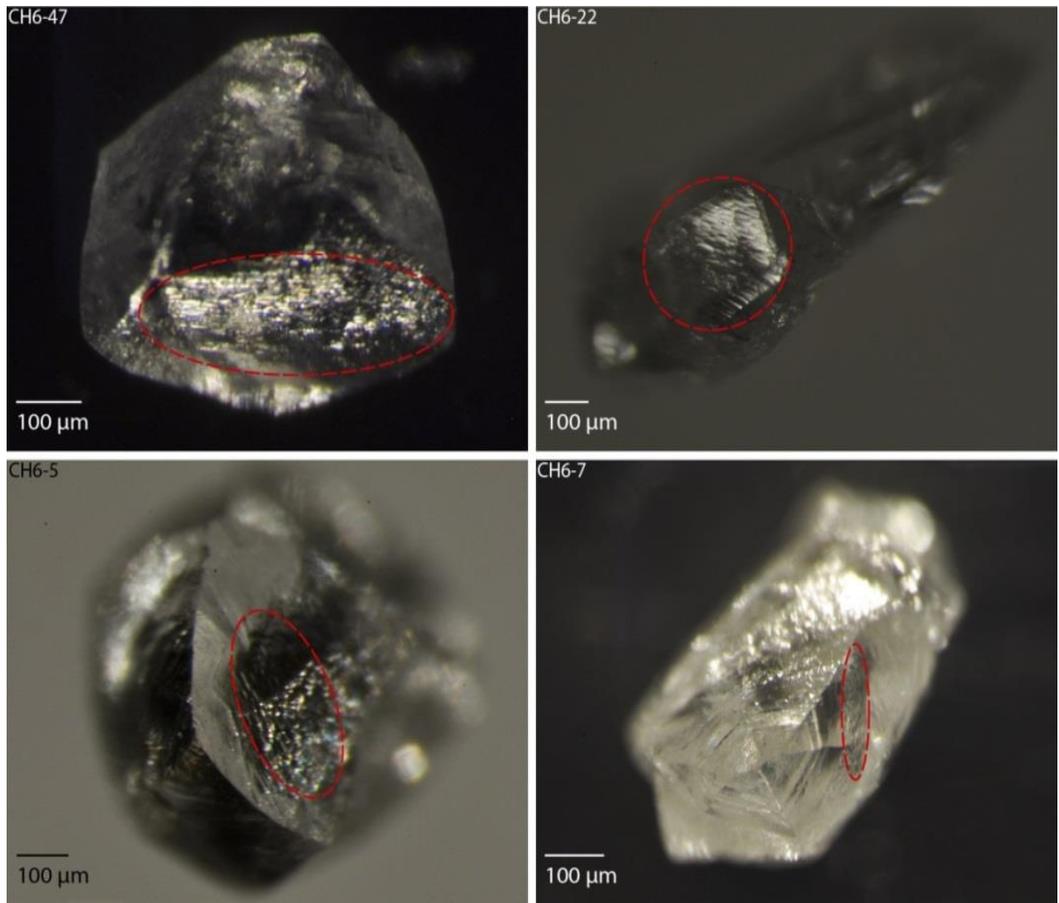
Figure B.3.2. Examples of hillocks, including boat shaped hillocks (CH6-47, CH6-7 and CH6-22) and pyramidal hillocks (CH6-5). The area showing hillocks is circled with a red dashed line.
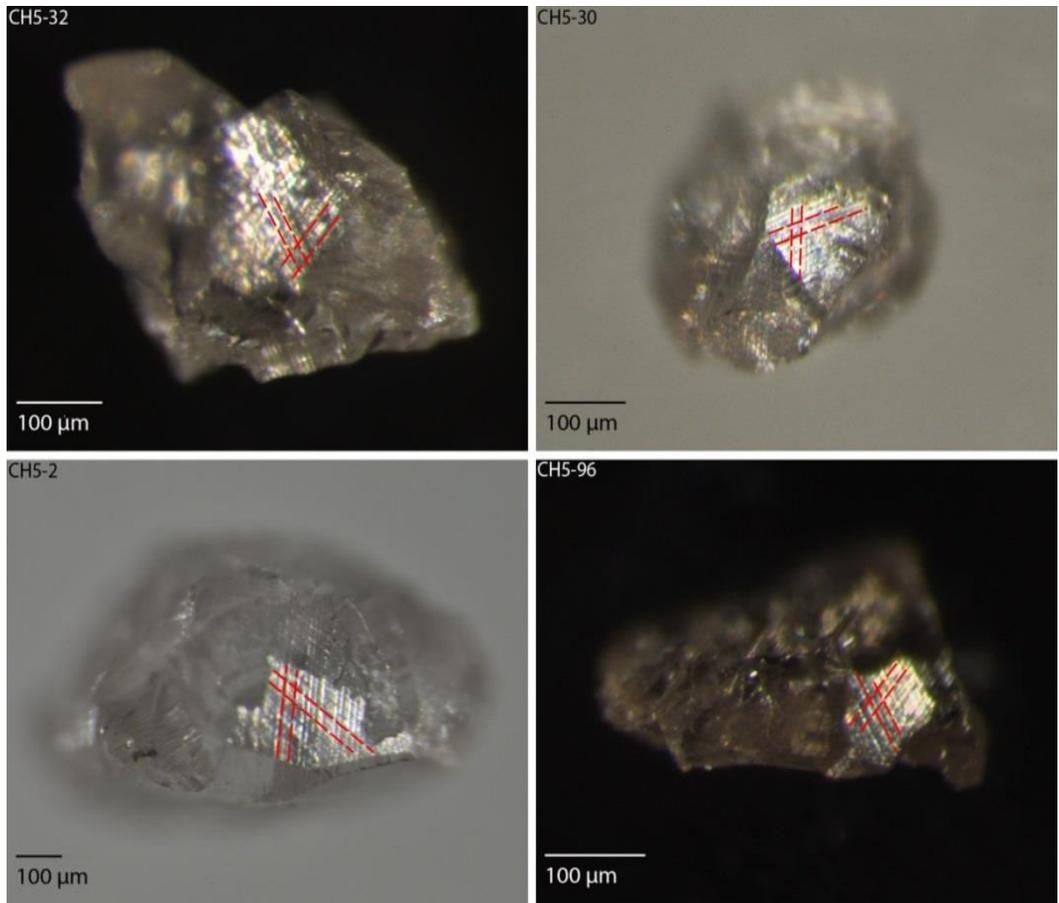
Figure B.3.3. Examples of plastic deformation lines; (highlighted with red dashed lines).
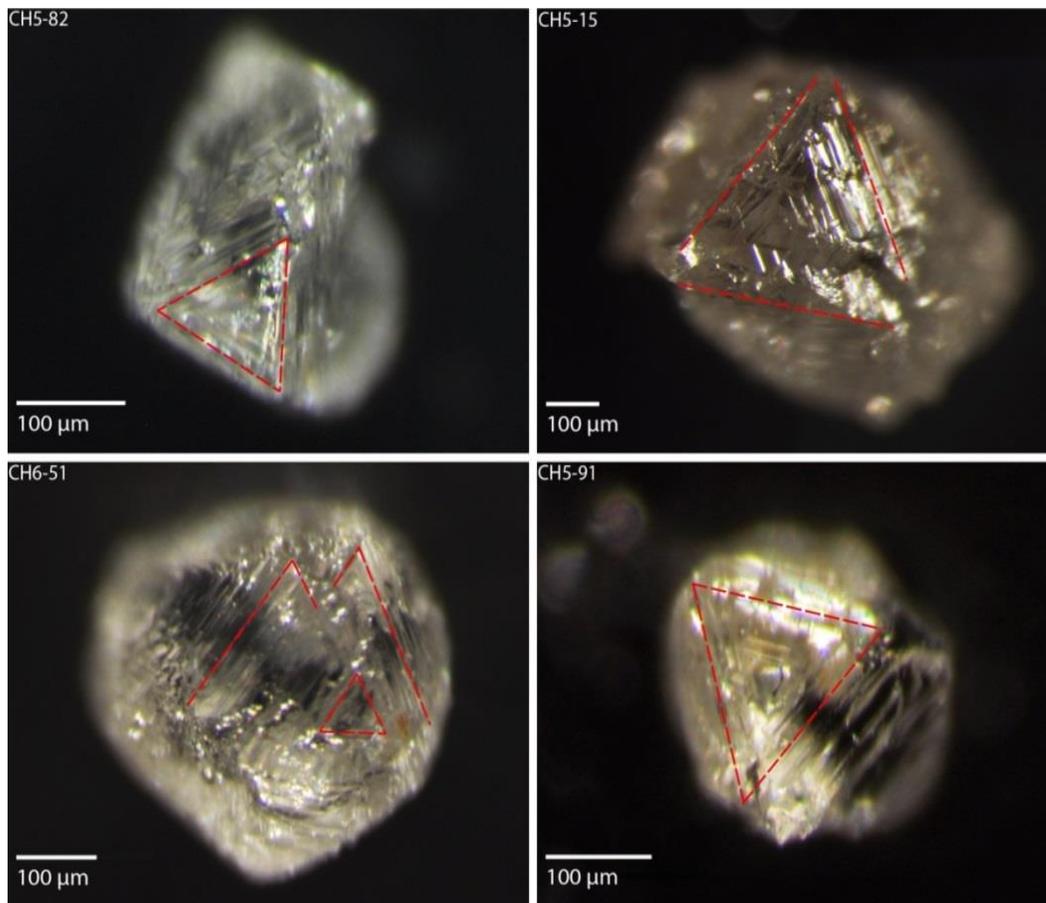
Figure B.3.4. Examples of stacked growth layers (outlined with red dashed lines).
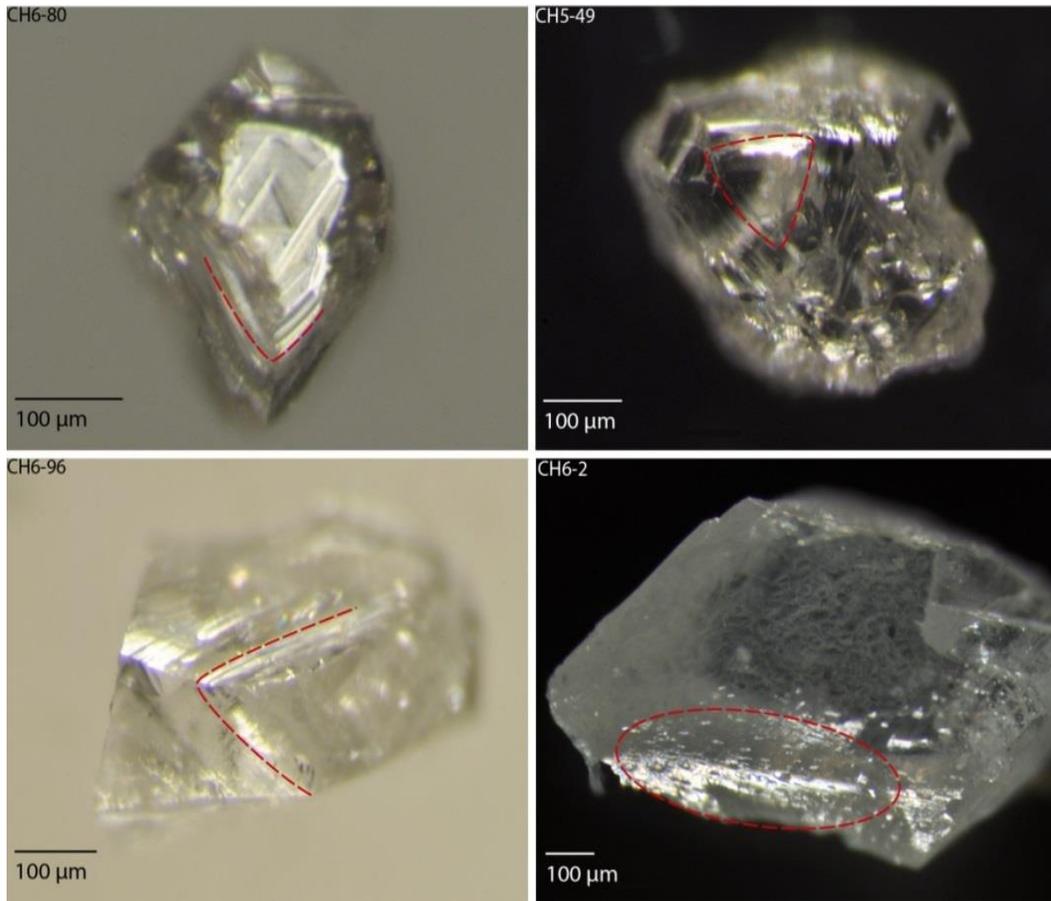
Figure B.3.5. Examples of shield shaped laminae and an example of corrosion sculpture (CH6-2) (outlined with a red dashed line).
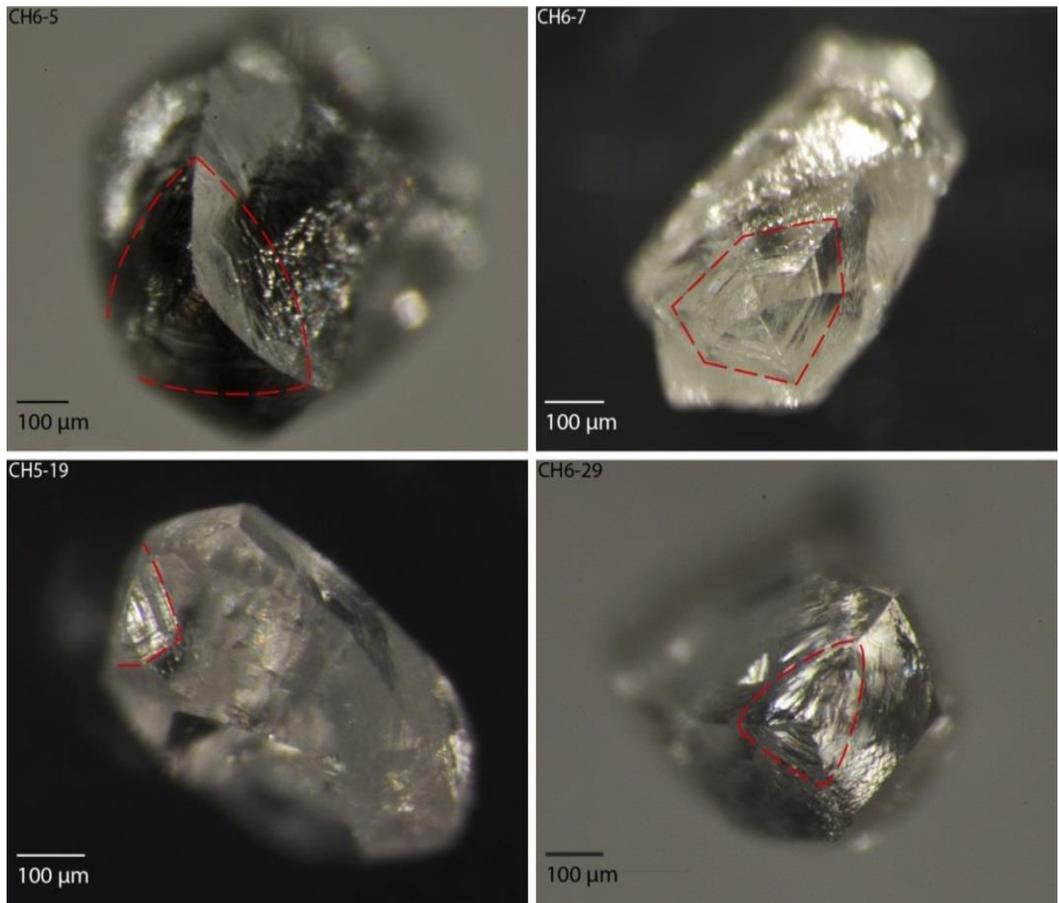
Figure B.3.6. Examples of terraces outlined with a red dashed line, two diamonds have a 3-fold axis (CH6-5 and CH6-29), and two diamonds have a pseudo 6-fold axis (CH6-7 and CH5-19).
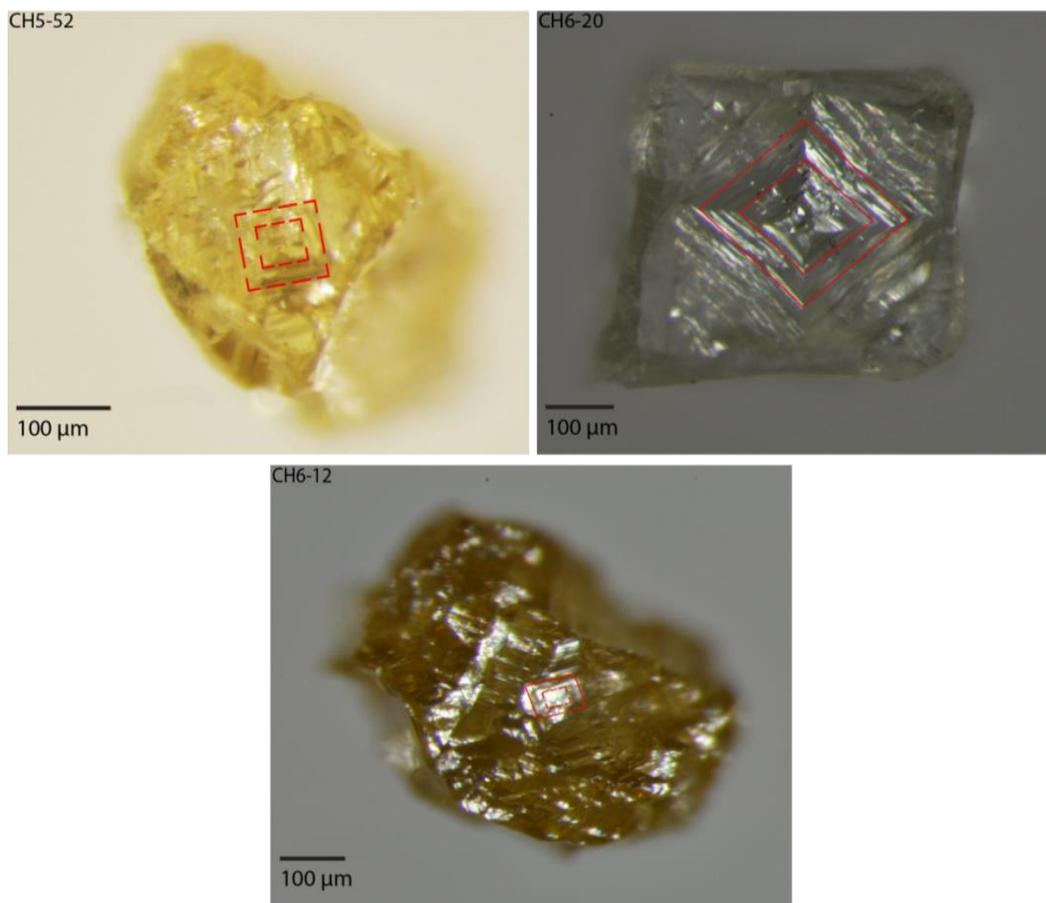
Figure B.3.7. Examples of tetragons on cubic diamonds; highlighted with dashed red lines.
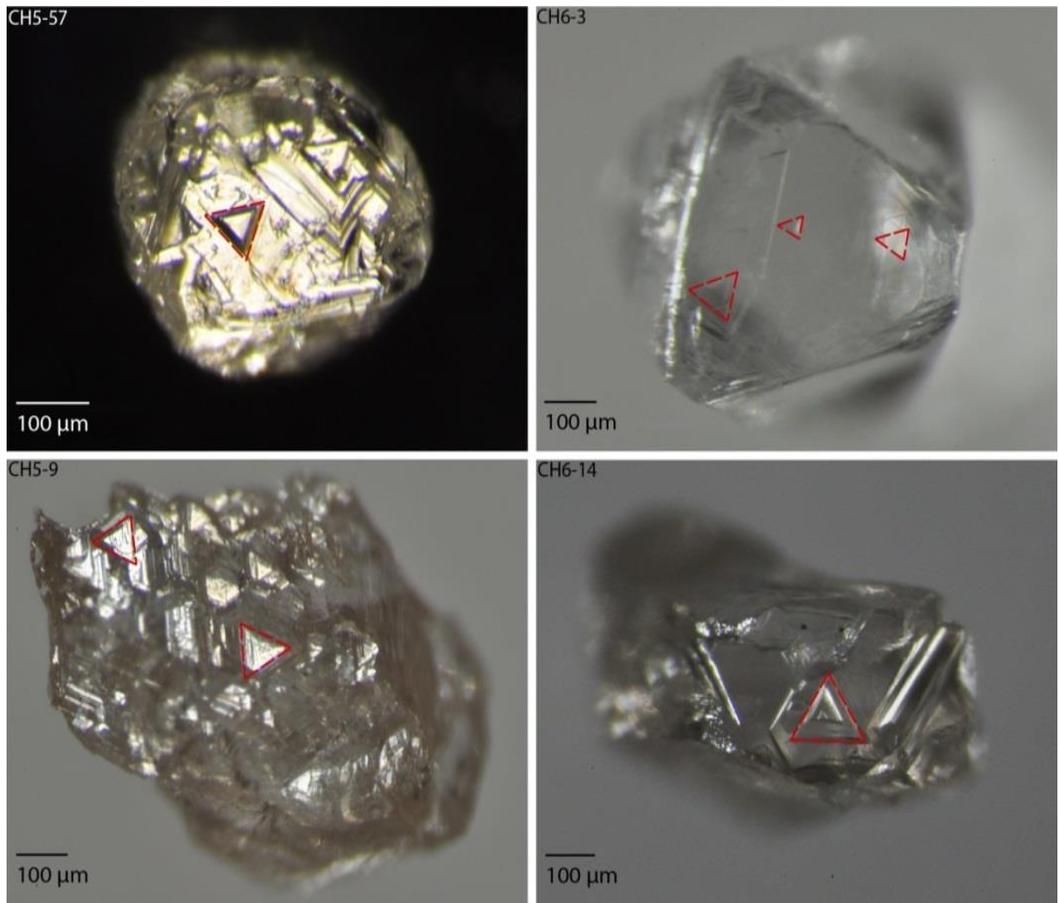
Figure B.3.8. Examples of trigons, highlighted with red dashed lines.

B.4 Diamond Breakage:
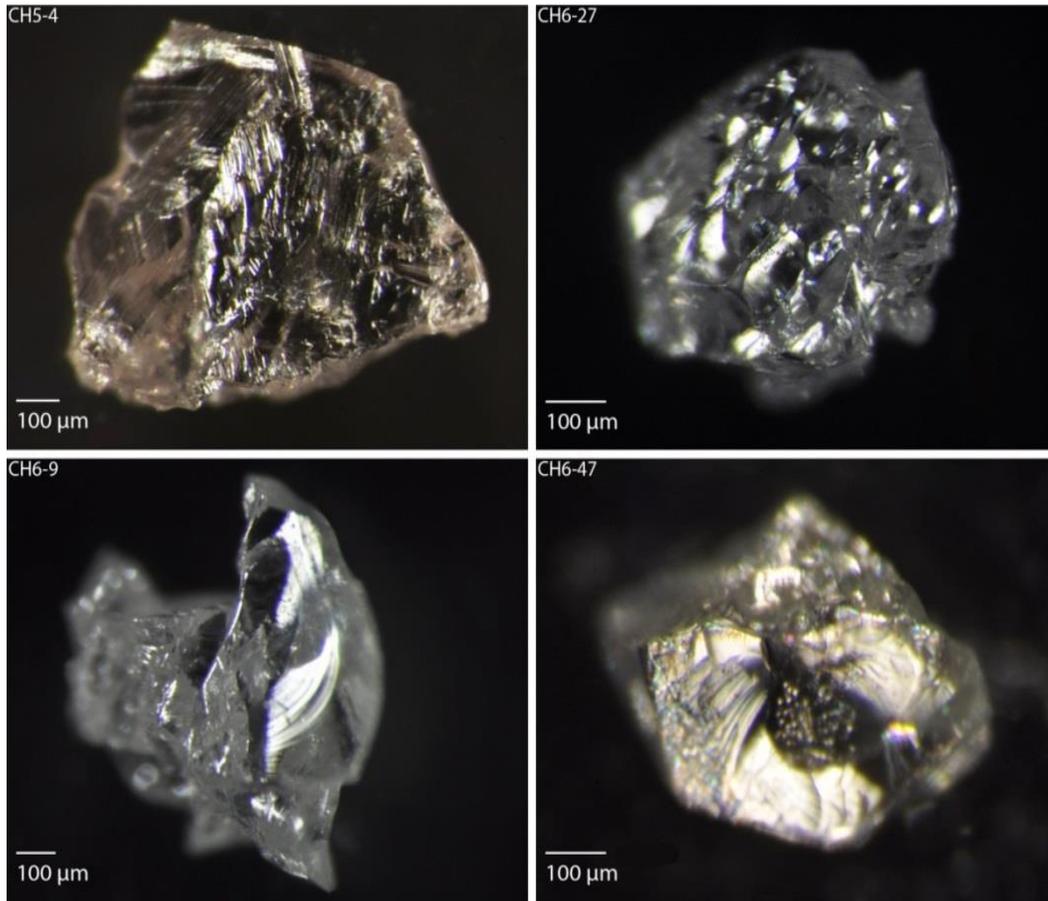
Figure B.4.1 Examples of fresh breakage surfaces on diamond. Diamond fragments are characterized as having only broken faces.
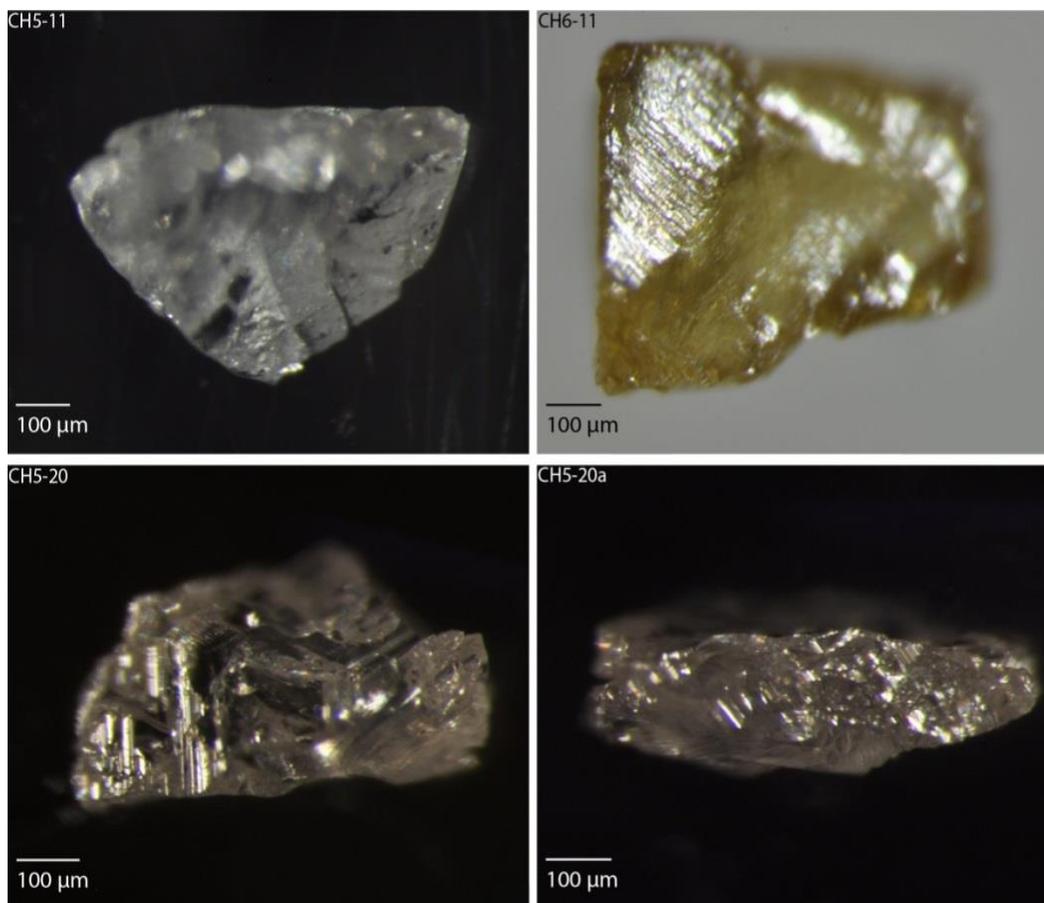
Figure B.4.2. Examples of diamond breakage surfaces showing signs of resorption or etching. Diamond CH5-20 shows a flat broken surface along the bottom of the diamond, CH5-20a shows the etch features on the broken face.

B.5 Inclusions:
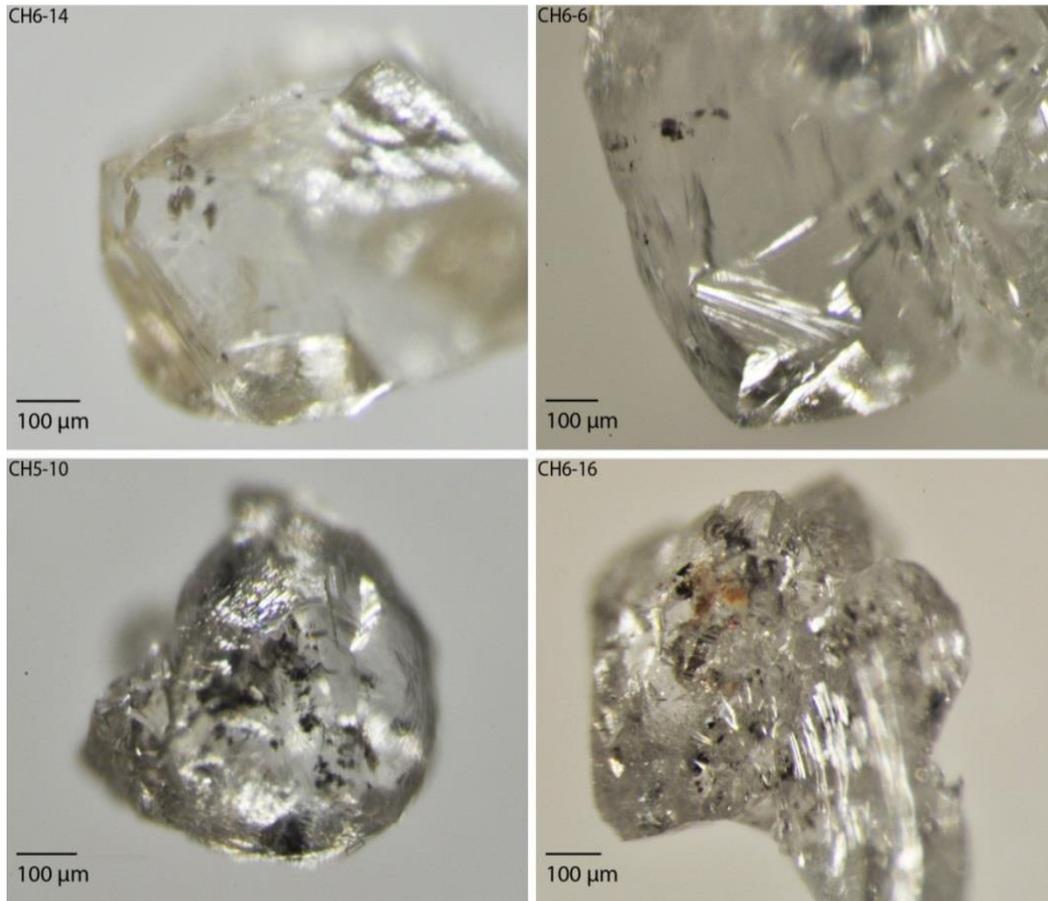
Figure B.5.1. Examples of inclusions. Most of the inclusions are likely graphite or small sulphide inclusions. There is one orange inclusion (CH6-16) which is likely an altered olivine.
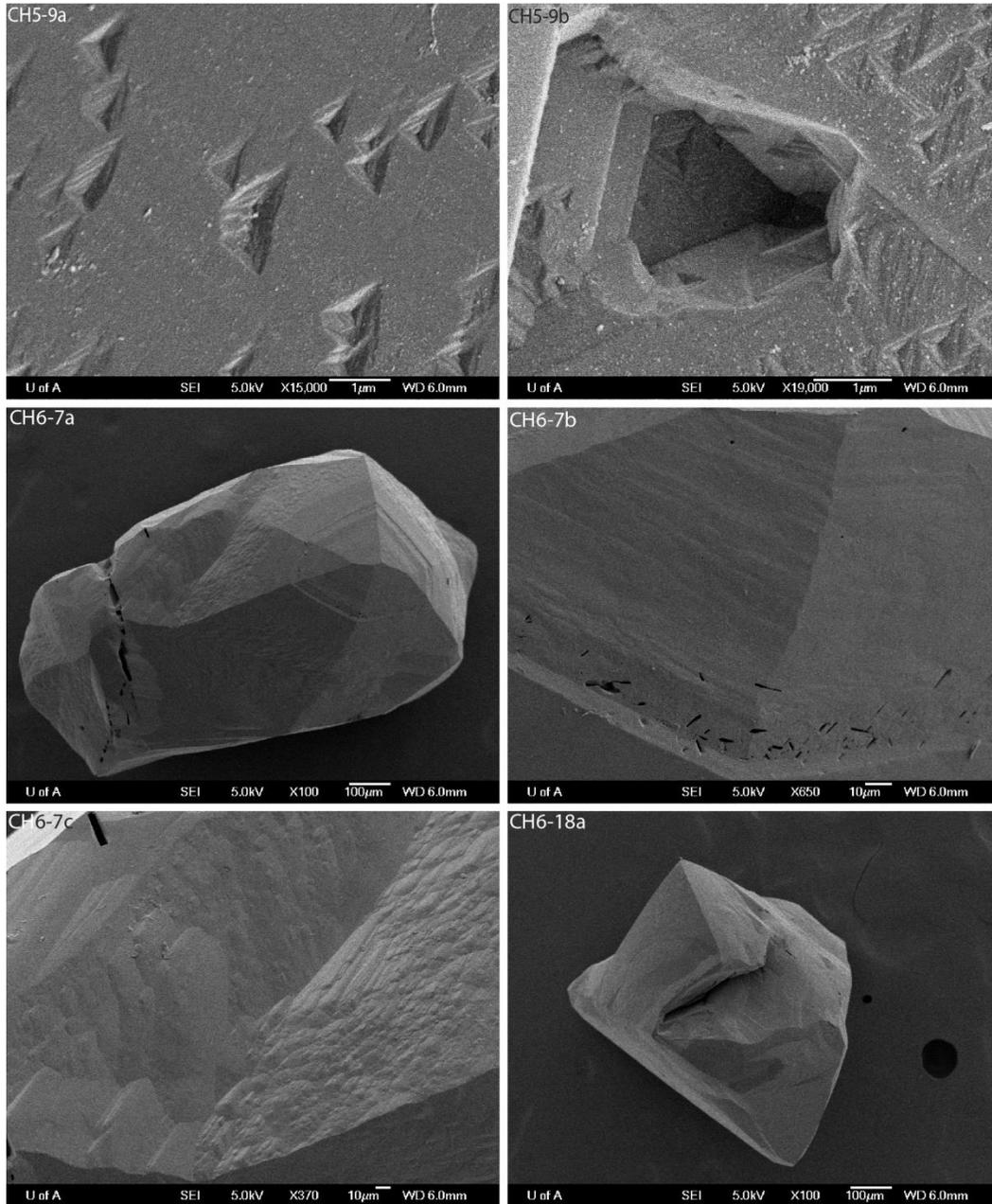
Figure C.1. SEM images of diamonds CH5-9, CH6-7, and CH6-18. CH5-9a shows pyramidal trigons, CH5-9b shows two orientations of trigons. CH6-7a is a dodecahedral macle displaying terraces around a pseudo-6-fold axis (in reality a three fold axis), CH6-7b shows boat-shaped hillocks, diamond CH6-7c shows pyramidal shaped hillocks. CH6-18a is a pseudohemimorphic diamond.
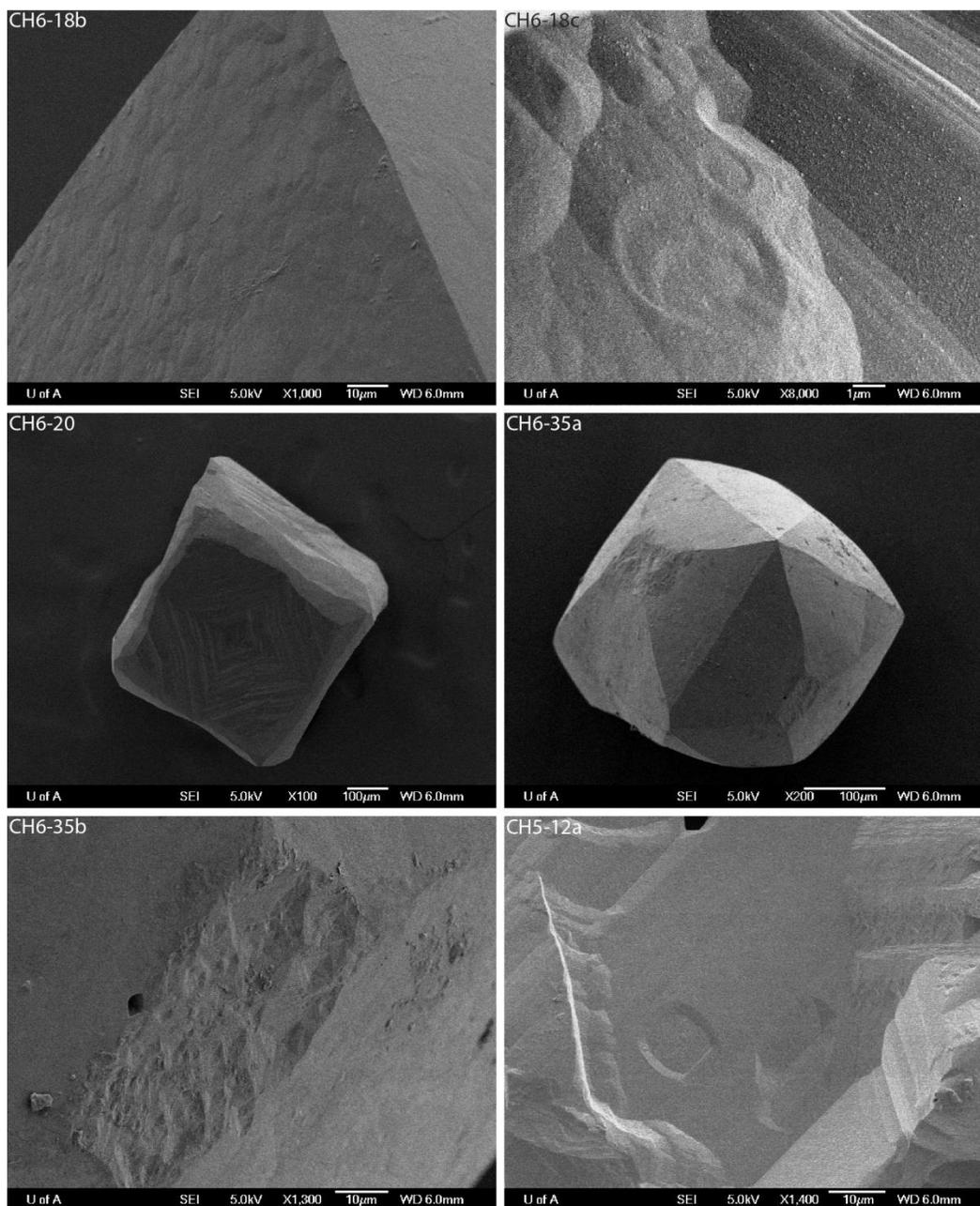
Figure C.2. SEM images of diamonds CH6-18, CH6-20, CH6-35, and CH5-12. CH6-18b shows the rough surface (possibly hillocks or shagreen texture) of the resorbed portion of the stone, CH6-18c shows circular depressions/corrosion sculpture. CH6-20 shows negative tetragons on a cuboid face. CH6-35a is a tetrahexahedroid, CH6-35b is the close up of a four-fold axis with tetragons on a tetrahexahedroid diamond. CH5-12a shows a roughly circular pit that may be associated with hexagonal pits.
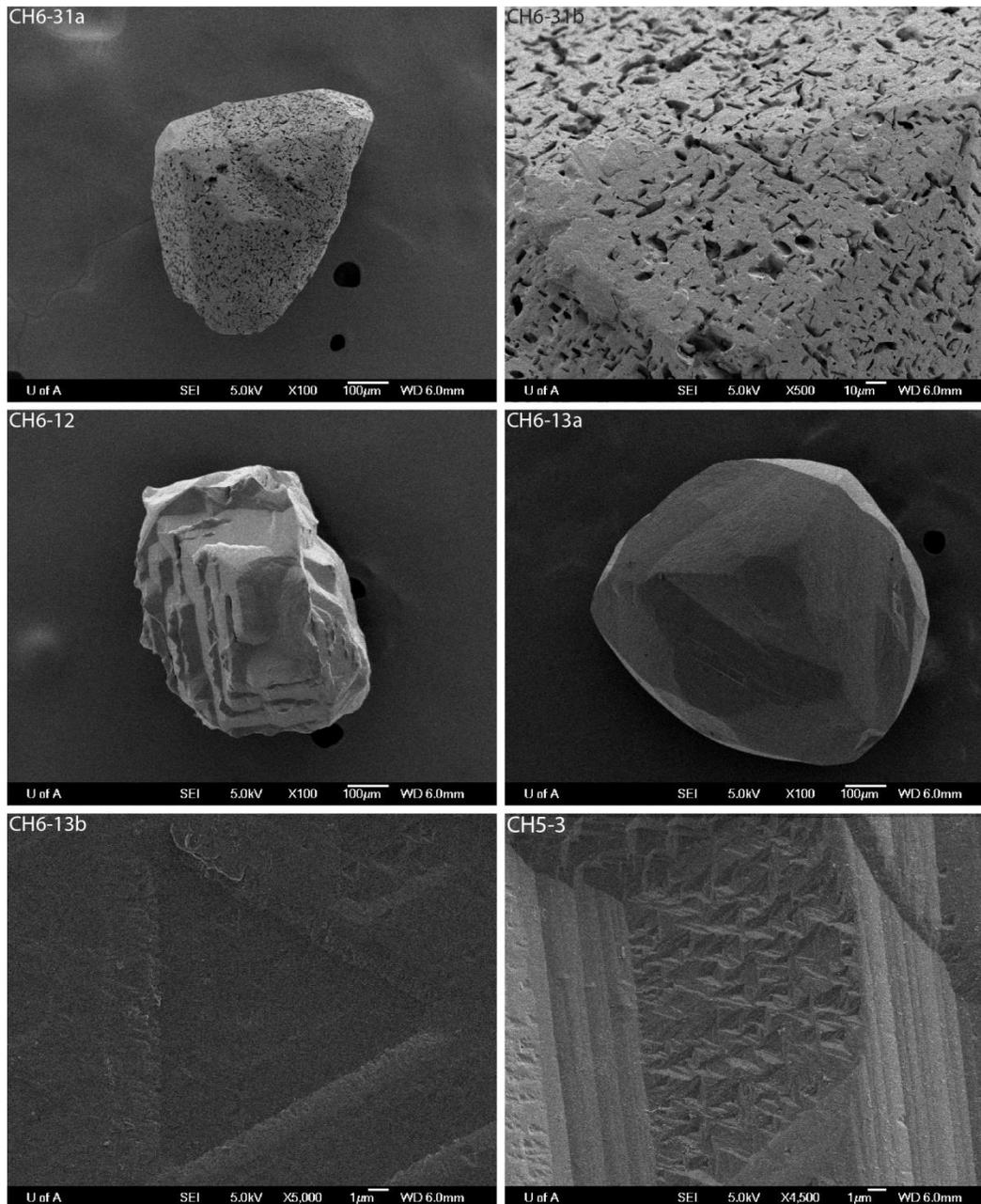
Figure C.3. SEM images of diamonds CH6-31, CH6-12, CH6-13, and CH5-3. CH6-31a is an opaque macle, CH6-31b is a close up of the surface patterns on the diamond. CH6-12 shows stepped growth on a cuboid face. CH6-13a is an example of an od (octahedral-dodecahedral) diamond, CH6-13b shows a trigon within a pit of another trigon of opposite orientation. CH5-3 is a cluster of small pyramidal bottomed trigons.

Appendix D: CL Images
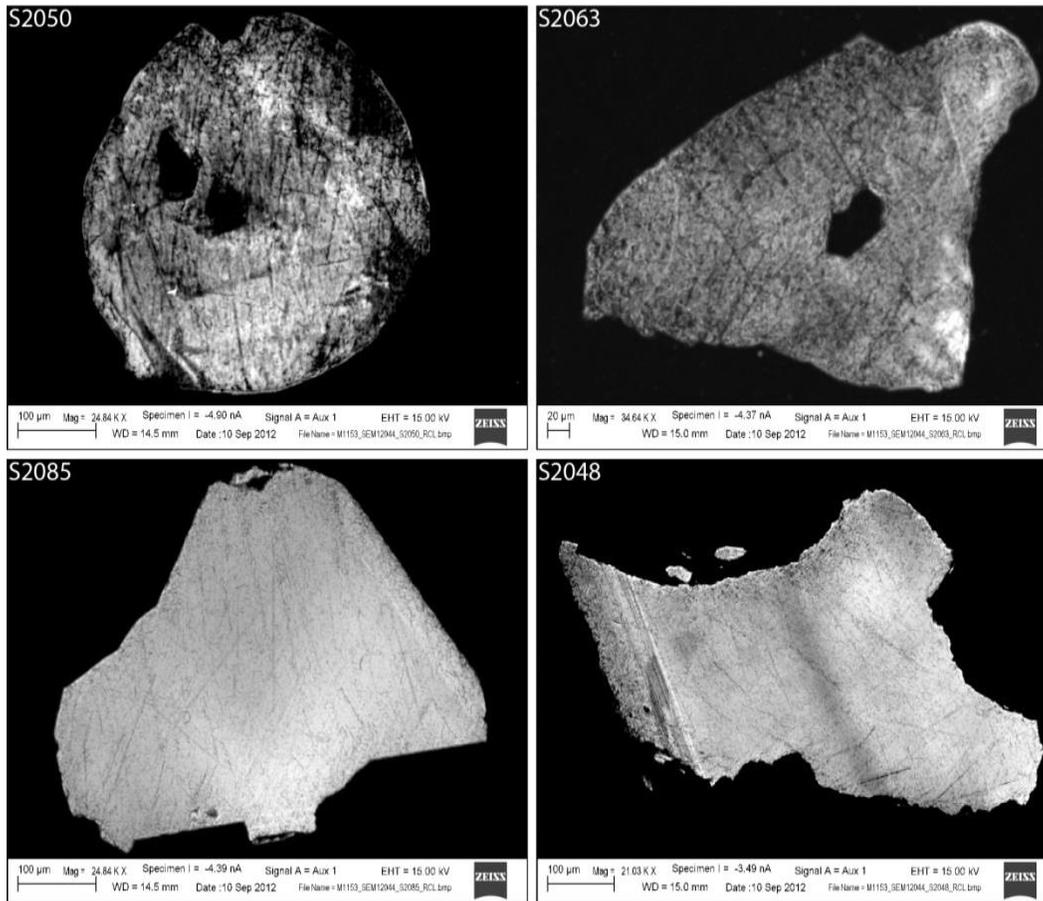
Figure D.1. Examples of homogenous CL.
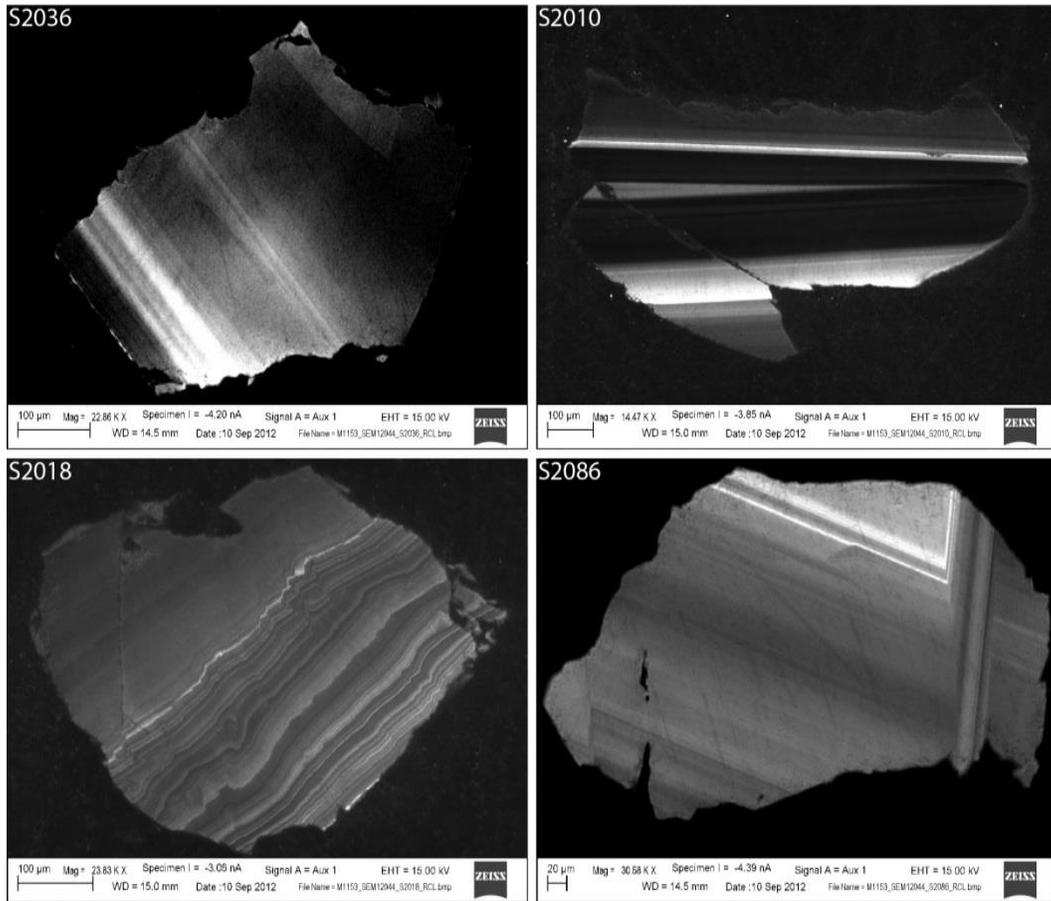
Figure D.2. Examples of agate-like banding. Diamonds S2036 and S2086 may represent octahedral growth from a fragment of a larger diamond.
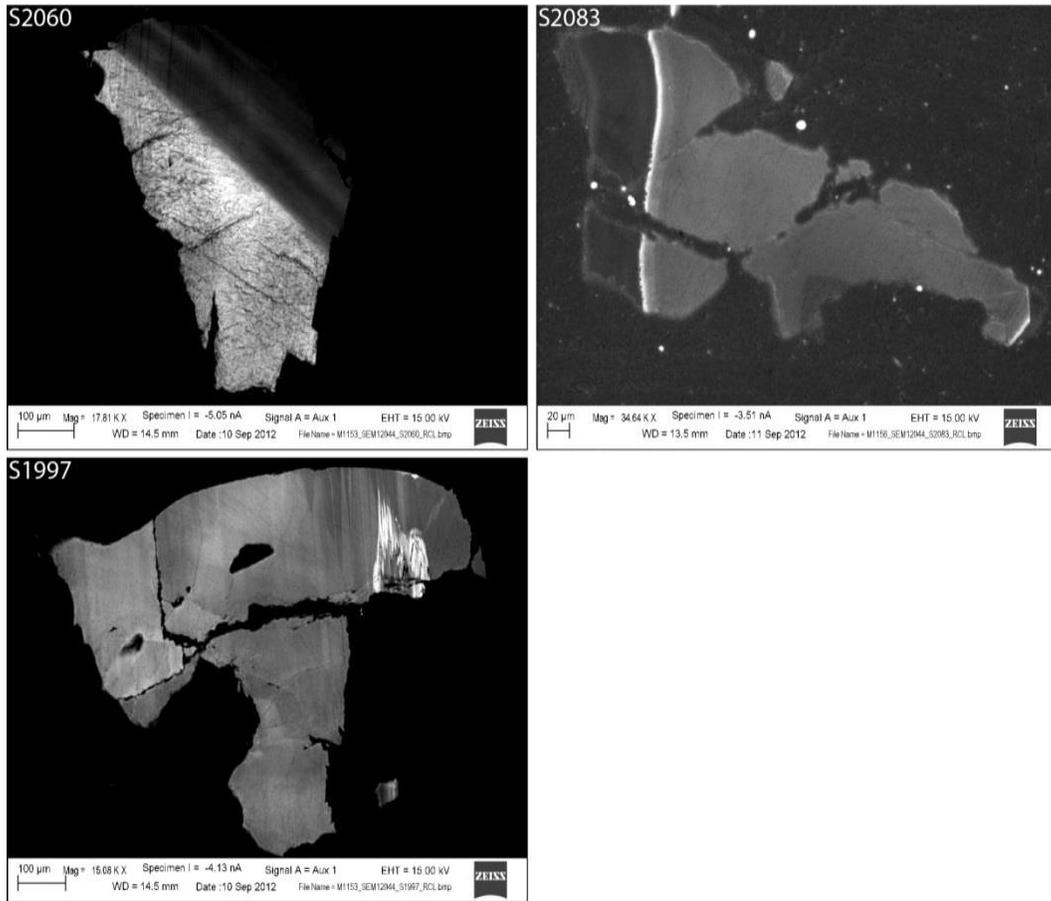
Figure D.3. Examples of mixed internal growth structures of homogenous and banded CL.
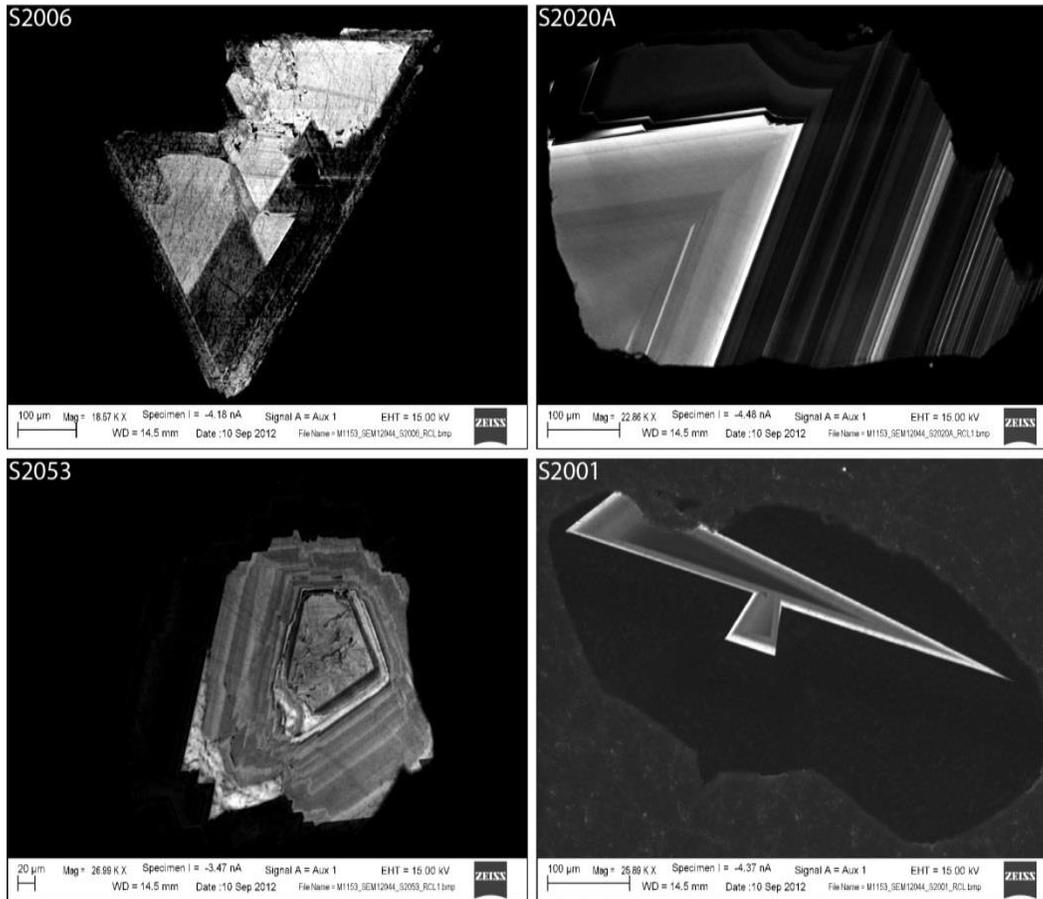
Figure D.4. Examples of octahedral internal growth structures (octahedral angles are 70°). Diamond S2053 has a distorted 4-sided central portion. Diamond S2001 has two distinct periods of growth, with the two "spear-like" portions possibly linked to the {111} octahedral directions, the dark CL has a micro-breccia appearance.
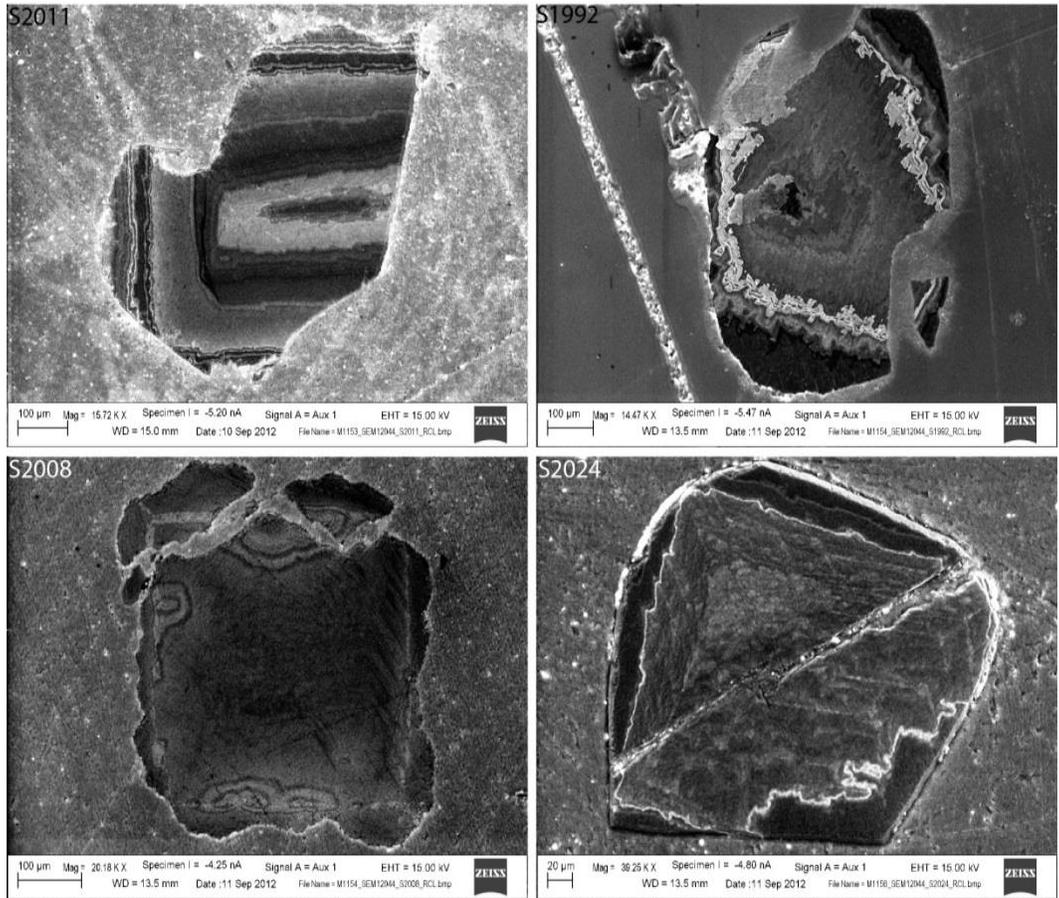
Figure D.5. Examples of cuboid internal growth structures. Cuboid internal growth can have a hummocky appearance. Diamond S1992 may represent distorted internal cuboid growth.
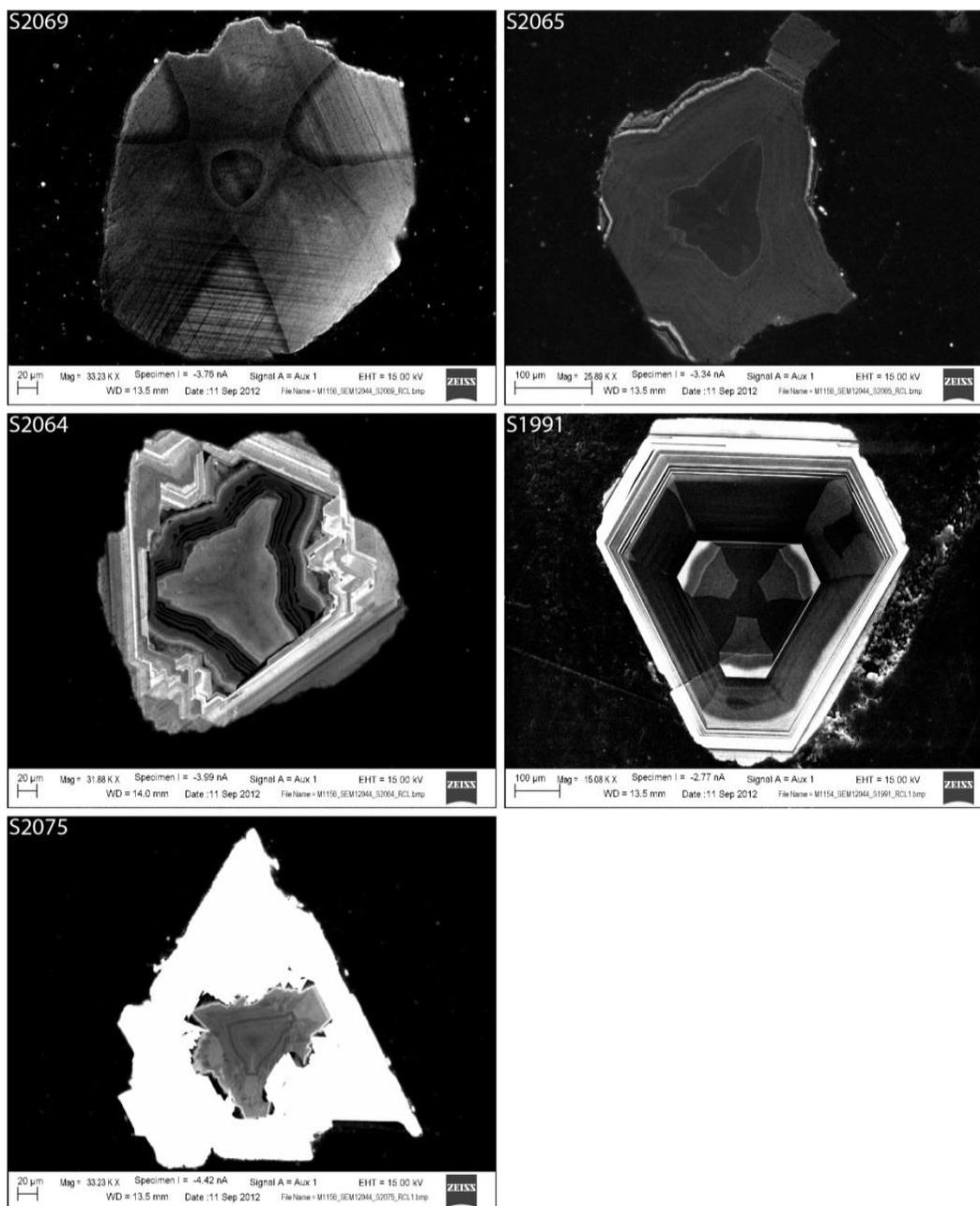
Figure D.6. Examples of mixed-habit growth diamonds with centre-cross patterns. Diamond S2069 shows 3 directions of plastic deformation lines; cuboid growth sectors are the lighter CL. The cuboid directions for diamond S2065 may be represented by the dark central CL. The three corners in central portion of diamond S2064 are likely three octahedral directions, the cuboid growth directions are the flatter growth bands; this portion of the diamond is truncated by a resorption front, followed by octahedral growth. The central portion of diamond S1991 shows equilibrium growth between the cuboid and octahedral growth sectors; either the mode of growth abruptly changes to octahedral growth or the cuboid sectors leave the plane of view. Diamond S2075 has a sharp change in CL

response, with the central portion exhibiting mixed growth. A resorption front may be present before octahedral growth takes over.
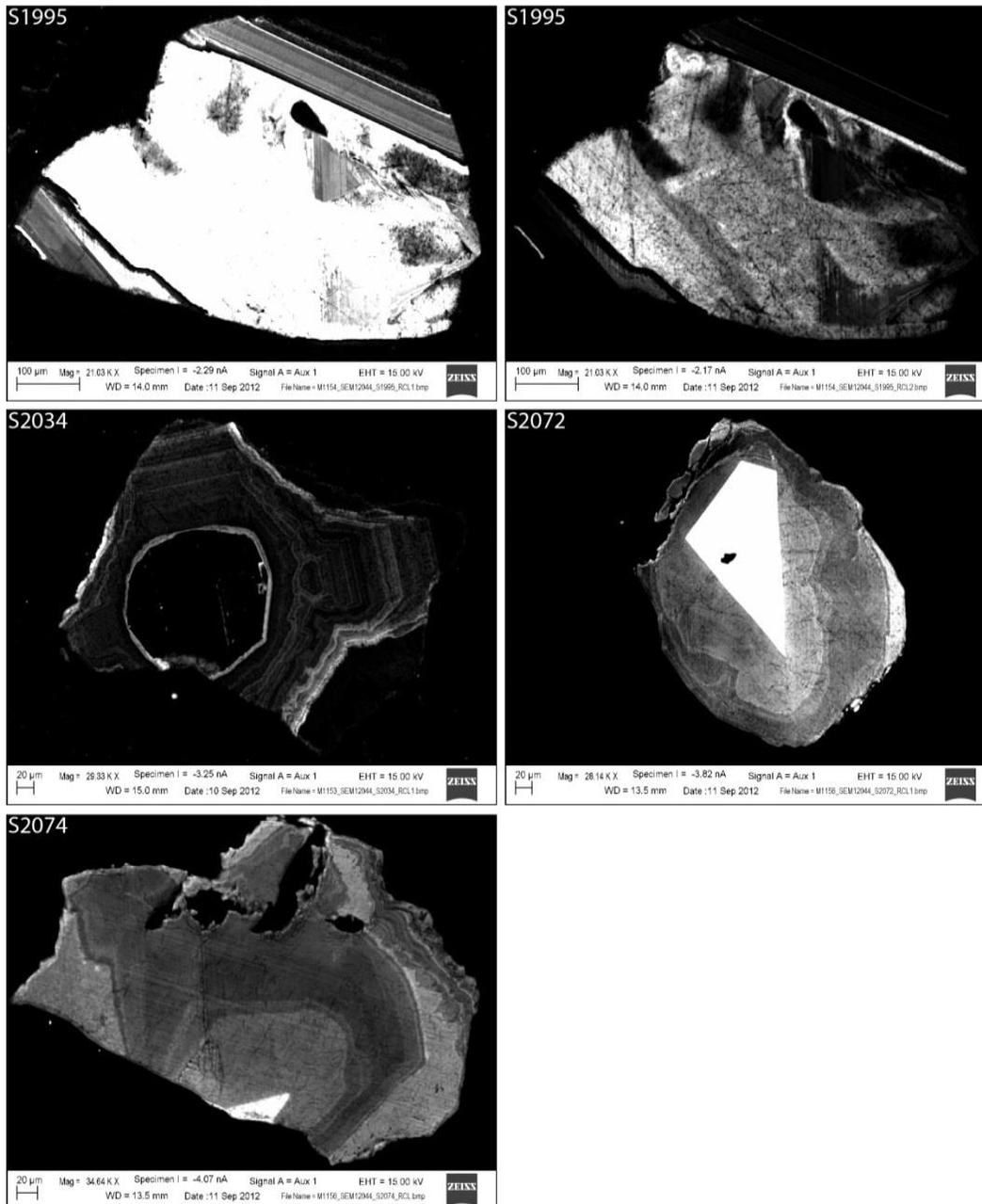

Figure D.7. Examples of hiatus CL, where there is a strong change in CL response. Resorption fronts are present between the strong changes in CL response for diamonds S1995 and S2034. Diamond S2034 is likely a partial re-entrant cube with the pointed portions representing octahedral directions and the flatter growth layers representing the relatively slow growing cuboid directions

(causing the re-entrant shape). All diamonds show a sharp change is growth between the layers and likely represent two distinct periods of growth.
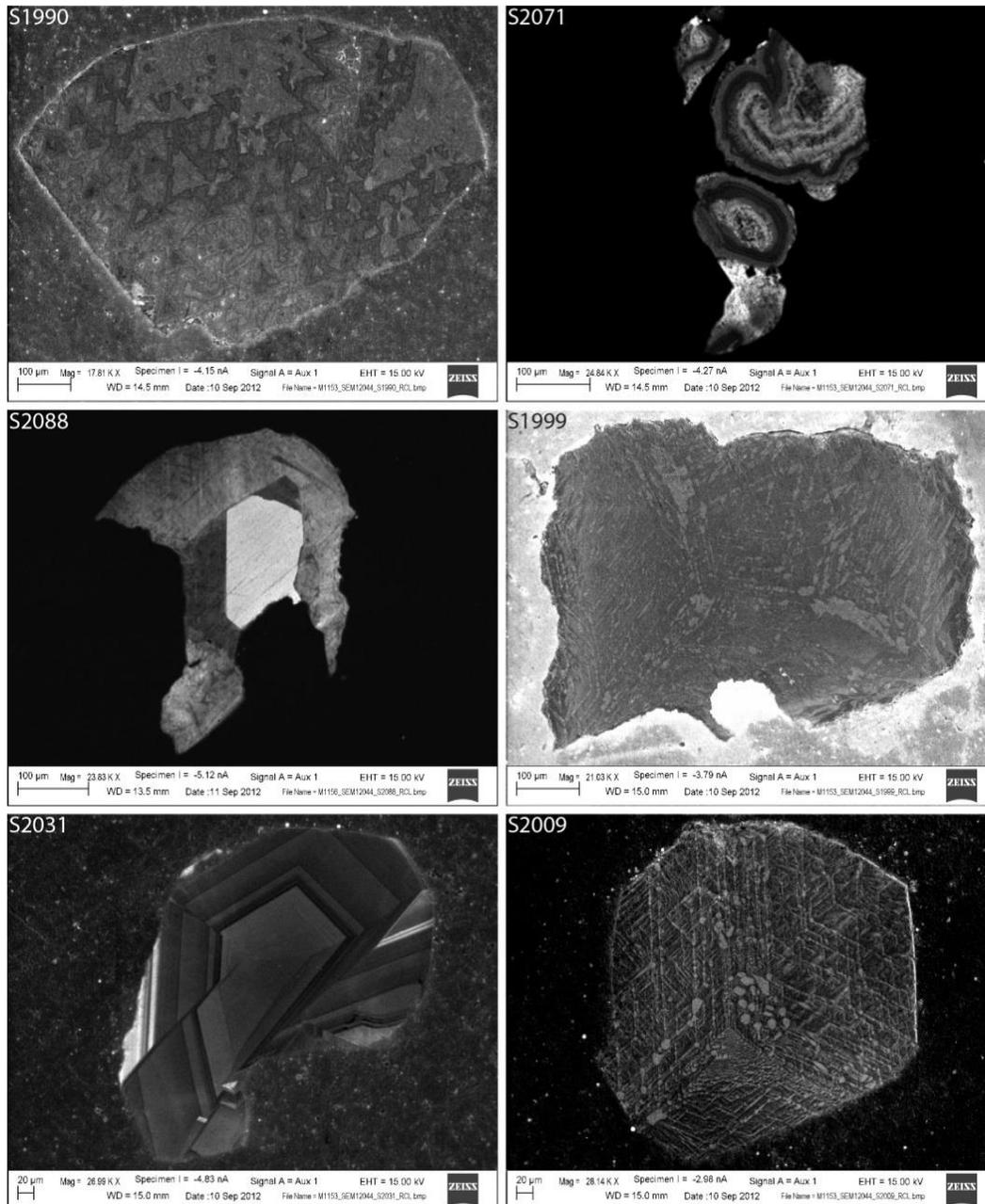

Figure D.8. Examples of complex internal growth structures. Diamond S1990 is a flat polished surface, but the CL gives the illusion of two orientations of trigons. Diamond S2088 shows a truncation of the bright and dark CL with overgrowth of the moderate CL portion of the diamond. The fault like dislocations in diamond S2031 most likely formed after initial diamond growth and offset the growth bands. The dislocation in the E section of the diamond is paired with a significant

thinning in the moderate grey second outer growth band, the growth layers on the right of this dislocation may be a continuation of the main pattern. The fault like dislocations may be due to plastic deformation. Diamond S2071 gives the impression that there are three portions of orbicular diamond with dark CL in-between. Diamonds S1999, S2009, both show bleb-like features that may be the visual representation of platelets (in diamond S2009 these are along octahedral planes; for diamond S1999 these blebs may also be oriented along octahedral planes but this cannot be clearly constrained).